Hyperspherical Approach to Quantal Three-body Theory

by

Jia Wang

B.A., Tsinghua University, 2004

M.Phil., Chinese University of Hong Kong, 2006

A thesis submitted to the

Faculty of the Graduate School of the

University of Colorado in partial fulfillment

of the requirements for the degree of

Doctor of Philosophy

Department of Physics

2012

This thesis entitled:
Hyperspherical Approach to Quantal Three-body Theory
written by Jia Wang
has been approved for the Department of Physics

Chris H. Greene

Prof. John Bohn

Prof. Eric Cornell

Date

The final copy of this thesis has been examined by the signatories, and we find that both the content and the form meet acceptable presentation standards of scholarly work in the above mentioned discipline.

Wang, Jia (Ph.D., Physics)

Hyperspherical Approach to Quantal Three-body Theory

Thesis directed by Prof. Chris H. Greene

Hyperspherical coordinates provide a systematic way of describing three-body systems. Solving three-body Schrödinger equations in an adiabatic hyperspherical representation is the focus of this thesis. An essentially exact solution can be found numerically by including nonadiabatic couplings using either a slow variable discretization or a traditional adiabatic method. Two different types of three-body systems are investigated: (1) rovibrational states of the triatomic hydrogen ion H_3^+ and (2) ultracold collisions of three identical bosons.

Dedication

To my love.

Acknowledgements

First and foremost, I'd like to thank my advisor Chris H. Greene, for his patience, motivation, enthusiasm, and immense knowledge. Working with Chris is a great experience, not only because of his unparalleled knowledge of atomic and molecular physics, but also because he has always been supportive of my career. He is also a nice and easygoing person, and will always be a role model in my life.

Besides Chris, working with other people in Greene's group is also a very nice experience. Jose D'Incao has always been a great teacher and big brother for me. Learning and discussing physics with him is always pleasant. I also owe many thanks to Yujun Wang. He has been very helpful in various projects during the last year. I also want to thank all the other group members: Michal Tarana, Chen Zhang, John Papaioannou, Nathan Morrison, Stephen Ragole, Victor Colussi, Minghui Xu and Javier von Stecher for all the discussions about physics during our fun group meetings and vast spare time. Previous group members Daniel Haxton, Zach Walters, Nirav Mehta and Seth Rittenhouse have also helped me a lot during my PhD years.

I would also like to thank the people outside the Greene group that I have gotten the pleasure of working with directly. Viatcheslav Kokoouline has given me tremendous help in the H_3^+ project. I would like to thank Richard Saykally and his group for sharing their beautiful experimental results with us. From the collaboration with Brett Esry, I learned how to think critically and how to be scientifically rigorous. Having the opportunity to collaborate with Eric Cornell is also a valuable experience. I am always amazed by his great intuition of telling the underlying physics out of complex phenomena.

I would also like to thank my Master advisor Chi Kwong Law and Ming Chung Chu in the Chinese University of Hong Kong, for bringing me into the beautiful world of atomic and molecular physics and giving me a strict training in scientific research.

I also owe many thanks to Peter Ruprecht and James McKown for all their technical support, and to Pam Leland for her administrative support.

I would like to thank all of my friends for supporting me and encouraging me with their best wishes. A special thanks goes to Yiqing Xie for her endless support during the last five years. Last but not least, I would like to thank my family for their unconditional support throughout my life.

I have received funding support from the National Science Foundation, the Department of Energy, and the Air Force Office of Scientific Research for this work.

Contents

Chapter

Tables

Table

Figures

Figure

Chapter 1

Introduction

The studies of three-body systems have a long and interesting history. In 1687, Sir Isaac Newton started studying the gravitational problem of three-body systems and presented some results in his famous "Principia" [17]. One of the most important applications at that time was for studies of the motion of the Moon under the gravitational influence of the Earth and the Sun as lunar theory [18]. During work to improve the accuracy of the lunar theory Henri Poincaré's research in the late nineteenth century led to the beginning of chaos theory. Poincaré extended the problem from the Earth-Moon-Sun system to general three-body systems with mutual gravitational interactions, as the "three-body problem". Because of this study, he won the prize competition in honor of the 60^{th} birthday of King Oscar II of Sweden in 1889. Poincaré discovered that such a system, under certain conditions, can exhibit chaotic behavior that is highly sensitive to initial conditions but impossible to predict in the long term. Chaotic behavior is described by the nonlinear differential equation governing the dynamics of a classical three-body system. However, such chaotic behavior would not exist in a classical sense for a quantal three-body system whose dynamic is governed by the linear Schrödinger equation. Nevertheless, the study of how chaotic classical dynamics can be described in terms of quantum theory became an interesting question, and leads to the beginning of quantum chaos theory in the twentieth century [19].

The studies of quantum chaos raise an interesting question: can quantum mechanics describe the exotic behaviors of three-body systems? Quantum mechanics has been proved to be very successful in describing two-body systems. One example is that for two particles interacting with

each other via a short-range interaction at ultracold temperatures, one single parameter, s-wave scattering length a, is sufficient to characterize the system. This simple description is verified by using a to determine the properties of a sufficiently dilute homogeneous Bose-Einstein condensation (BEC) [20] and compare them with experimental observations [21, 22, 23]. However, when the experimentally achieved densities become greater and greater, physicists have realized that the description of the system only in terms of two-body interactions is no longer sufficient. Quantum calculations of a three-body system are then a natural extension of two-body analogies and serve as a key meeting point for theoretical and experimental efforts to understand few-body physics. In this thesis, we use the hyperspherical coordinate approach to study three-body systems.

Hyperspherical coordinates have been applied successfully in several areas of theoretical physics ranging from nuclear physics [24, 25, 26] to atomic structure [27, 28, 29, 30] and fundamental few-body scattering [31, 32]. In a three-body system, there are nine degrees of freedom in total. After separating out the center-of-mass motion, the remaining six degrees of motion can be described by three Euler angles (α, β, γ) and three internal coordinates: the hyperradius R and two hyperangles, θ and ϕ. In particular, the hyperradius R represents the overall size of the system. Some of the deepest insights into the nature of the three-body problem have emerged from Macek's adiabatic hyperspherical methodology [27]. In this method, the Hamiltonian of the system is initially diagonalized at fixed values of the hyperradius R, and the eigenvalues yield a set of 1D-coupled adiabatic potential curves that represent the energy of the system as a function of R. The resulting eigenfunctions can be used to develop the coupling matrices between these potential curves. These potentials and couplings not only can be used for almost exact numerical calculation, but also help to build an intuitive understanding of the system. The potentials can describe available reaction pathways by indicating the threshold laws and scaling laws for the corresponding reactions. They also give information about the bound/quasi-bound states of the system and the excitation and decay mechanisms of these states. Furthermore, the coupling matrix elements allow accurate calculations of the full three-body Schrödinger equation for bound-state problems and two-body inelastic and rearrangement collisions ($A + BC \rightarrow AB + C$), three-body

collisions ($A + B + C$), and photon-assisted collision processes.

The application of the hyperspherical-coordinates approach to quantal three-body problems dates back at least as far as the pioneering work of Llwellen Hilleth Thomas in 1935 [33]. He realized a striking quantum effect in a three-body system: when the ratio between the potential range (r_0) and s-wave scattering length (a) becomes arbitrarily small, $r_0/a \to 0$, the ground state energy of the system can "collapse" to $E \to -\infty$. This effect is known as the Thomas collapse. In this case, all three particles collapse into an infinitely small size with an infinitely large binding energy. This phenomenon can be understood in the hyperspherical picture. The effective hyperspherical potential of such a system has the form of $-\left(s_0^2 + 1/4\right) / \left(2\mu_{3b}R^2\right)$ for $r_0 \ll R \ll a$, where μ_{3b} is the three-body reduced mass. The parameter s_0 is universal, i.e., it does not depend on the form of interaction as long as $r_0/a \to 0$. For three identical bosons, $s_0 = 1.00624$. It is well known that such potentials can support an infinite number of bound states and that all the nearby eigen energies are related with a geometric scaling factor $E_{n+1}/E_n = \exp\left(-2\pi/s_0\right)$. Clearly, this geometric scaling factor is also universal [$\exp\left(\pi/s_0\right) \approx 22.7$ for three identical bosons]. This universal scaling factor implies that when n approaches $-\infty$, infinitely tightly bound states (called Thomas's collapse states) exist. In real physical systems, however, the range of interparticle interactions r_0 can never be zero. Presumably, this fact prevents a Thomas collapse from being observed. On the other hand, there is no similar obstacle to observing a closely related quantum effect, namely the Efimov effect, as n approaches $+\infty$. In 1970, Efimov predicted that when a two-body bound state is exactly at the threshold, i.e., $a \to \infty$, there is an infinite number of bound states just below the three-body break-up threshold [26]. These states, called Efimov states, also obey $E_{n+1}/E_n = \exp\left(-2\pi/s_0\right)$ as a result of the $-\left(s_0^2 + 1/4\right) / \left(2\mu_{3b}R^2\right)$ potential for $R \gg r_0$, which is usually called the Efimov potential.

The fact that Efimov effect is universal implies that it can exist in any systems of three identical bosons interacting with each other via short-range interactions. Ultracold atomic gases are perfect systems for studying Efimov effects experimentally, because of the extraordinary degree of control for such systems. Using techniques such as laser cooling and subsequent evaporative

cooling of atomic gases, the experimentalists can now reach the nano Kelvin range with high densities (between about 10^{12} and 10^{15} cm^{-3}), and finally attain BEC [21, 22, 23]. In addition, applications of Feshbach resonances allow physicists to control the scattering length a between ultracold atoms and study the properties of condensates. In particular, when three free particles collide at ultracold temperatures, they can form a two-body bound state and a free particle, which is called a three-body recombination ($A + A + A \rightarrow A_2 + A$). This recombination process normally releases a large amount of kinetic energy, producing atomic losses that often limit the lifetimes of Bose-Einstein condensates [34]. Theoretical studies indicate that there is an a^4 scaling of the field-free recombination rate of three identical bosons that leads to a catastrophic loss of atoms even if a is not quite large. Three-body recombination is a process that is also closely related with the Efimov effects. When a is much larger than the range of two-body interaction r_0 but still finite, Efimov states can cause interference and resonant effects in three-body recombination processes when they cross thresholds. The hyperspherical approach gives a comprehensive description of three-body recombination and a fundamental understanding of how Efimov states affect three-body recombination [35, 36].

Hyperspherical coordinate has also been applied to study triatomic molecules. As the simplest triatomic molecule, H_3^+ is an interesting system that attracts theorists to high-accuracy quantum calculations. H_3^+ also plays an important role in astrophysics since it acts as a proton donor in chemical reactions occurring in interstellar clouds [37, 38]. Furthermore, this ion also helps to characterize Jupiter's atmosphere from afar [39, 40]. H_3^+ is the dominant positively charged ion in molecular hydrogen plasmas and was first identified in 1911 by J. J. Thomson with an early form of mass spectrometry [41]. Without a stable electronic excited state and a permanent dipole moment, H_3^+ cannot be observed by electronic spectroscopy or rotational spectroscopy. Therefore, an infrared rotation-vibration spectrum is the only mean to observe this ion. The first observation was carried out by T. Oka in 1980 [42]. By 2012, more than 600 low-lying rovibrational states of H_3^+ had been identified. The good agreement between the experimental spectrum and a first-principles calculation provided a benchmark for calculations on other polyatomic molecules such

as water. Application of the hyperspherical approach to study H_3^+ leads to a better understanding of a quantum phenomenon that once was considered mysterious and esoteric. This phenomenon is the dissociative recombination (DR) of H_3^+

$$e^- + H_3^+ \rightarrow \begin{cases} H_2 + H \\ H + H + H, \end{cases} \tag{1.1}$$

which is one of the key process to understand chemical reactions in diffuse interstellar clouds [43]. However, there once was a three-orders-of-magnitude discrepancy between the theoretical and experimental DR rate of H_3^+. This discrepancy was finally dissolved by Kokoouline and Greene in 2003 using the hyperspherical approach [31]. The use of hyperspherical coordinates has both a practical computational advantage and a qualitative conceptual advantage in this problem. For instance, the theory of DR is much better understood for a diatomic target than for a polyatomic target, so the use of an adiabatic hyperspherical representation of the nuclear positions ultimately maps polyatomic DR theory back in terms of the more familiar diatomic DR theory. In addition, applying the hyperspherical approach to describe the coupling between an incident electron and the vibrational or dissociative degrees of freedom of H_3^+ permits a natural inclusion of the Jahn-Teller coupling and dissolves this discrepancy [31].

In this dissertation, we apply the adiabatic hyperspherical approach to investigate two different types of three-body systems: (1) rovibrational states of the triatomic hydrogen ion, H_3^+ and (2) ultracold collisions of three identical bosons. Both systems provided interesting questions and rich physics to explore. The remainder of this thesis is organized as follows. Chapter two discusses the details of our numercial approach, the adiabatic hyperspherical representation. The hyperspherical coordinates used in this thesis are first introduced. Then the numerical methods for both bound states and scattering-state calculations are elaborated.

In chapter three, we calculate the rovibrational states of H_3^+ with the tools described in the last chapter. We model H_3^+ as three protons interacting with each other on a potential surface. Our calculation gives rovibrational energies that are in good agreement with experimental results. In addition, using accurate rovibrational-state wave functions, we apply multichannel quantum defect

theory to studying the Rydberg energy levels of H_3, which consists of a Rydberg electron and an H_3^+ ion core. The interaction between the Rydberg electron and the ion core is described via body-frame quantum defects. We perform the rovibrational-frame transformation with rovibrational wave functions of H_3^+ to obtain laboratory-frame quantum defects that are used to calculate both the energy levels and the mid-infrared spectrum of the H_3 Rydberg states. The mid-infrared spectrum corresponds reasonably well with the laser lines recently observed in hydrogen/rare gas discharges [44, 45], indicating that H_3 is a likely candidate for the carrier of these lasing transitions. A lasing mechanism for the population inversion is also proposed.

In chapter four, we study another type of three-body system: three-body recombination at ultracold temperature. In this chapter, we study three-body recombination processes numerically for a system of three identical bosons with a much more realistic model than used in previous studies. Our two-body model potentials support many bound states, which is a major leap in complexity. Our study indicates that recombination into deeply bound states can be described by the dominance of one decay pathway, resulting from the strong coupling between different recombination channels. Moreover, the usual Wigner threshold law must be modified for excited-incident recombination channels. Three-body recombination has also been recognized as one of the most important scattering observables in which features related to the universal Efimov physics can be manifested, which will be studied it in the next chapter.

In chapter five, problems related to Efimov physics are studied. Efimov physics predicts that there are an infinite number of three-body bound states for a three-identical-bosons system when the two-body s-wave scattering length $a \to \infty$ [26]. Tuning a from infinity to finite and negative (but still much larger than the range r_0 of the interactions), these three-body states disappear into the continuum one by one at different scattering lengths a_n^-. Whenever an Efimov trimer hits the threshold, a resonance in recombination is observed. It is remarkable that the values of a_n^- for two nearby resonances are related by a scaling factor of approximate by 22.7 that is universal, i.e., independent of the details of the short-range interaction. Hence, we only need one three-body parameter to determine the absolute positions of all the resonances. However, this

three-body parameter was once believed to depend on the details of two- and three-body short-range interactions, suggesting that this parameter would not be universal. Surprisingly, recent experiments support the idea that the three-body parameter exhibits universality. We explore the origin of this universality. Our study shows that the three-body parameter universality emerges because a universally effective barrier in the three-body potentials prevents the three particles from simultaneously getting closer to each other. Our results show limitations to this universality, as it is more likely to occur for neutral atoms and less likely to extend to light nuclei.

Chapter six focuses on three-body collisions on the positive side. When the scattering length is large and positive, minimums show up in the three-body recombination rate because of a destructive interference effect. When the Efimov states hit the atom-dimer thresholds, resonances in atom-dimer relaxation can also be observed. The universality of three-body parameter represented by the minimum position is also found to be universal for cold atoms. In addition, a universal three-body state attached to the d-wave two-body state is found in our model. The d-wave state crosses the threshold and becomes bound at a universal s-wave scattering length a_d^*. Near a_d^*, two enhancement peaks in three-body recombination can be found. The positions of the two peaks are also quite universal. The one larger than a_d^* corresponds to the three-body state attaching to the d-wave dimer, and the one smaller than a_d^* corresponds to the competition between a new d-wave threshold and the a^4 power law.

Chapter 2

Adiabatic Hyperspherical Approach

Hyperspherical coordinates have a long and distinguished history in atomic, molecular and nuclear physics. This chapter discusses the details of the adiabatic hyperspherical approach, which is a numerical method we found to be suitable for calculations of three-body systems. Section 2.1 introduces the hyperradial coordinates used in this thesis. Section 2.2 sets up the adiabatic hyperspherical approach. Some particularly important quantities, called the coupling matrices, are studied in section 2.3. Finally, section 2.4 presents applications of the adiabatic hyperspherical approach to three-body problems, including both bound-state calculations and scattering studies.

2.1 Hyperspherical coordinate

There are numerous conventions for defining hyperspherical coordinates. The modified version of Whitten-Smith's democratic coordinate described in this section is one of the most convenient conventions for our study. After separating the center-of-mass motion, the six remaining degrees of freedom are described by three Euler angles (α, β,γ), two hyperangles (θ and ϕ), and one hyperradius R. In this convention, the hyperangles and the hyperradius can be best constructed in two stages, as shown in Ref. [46]. We first introduce the mass-scaled Jacobi coordinates,

$$\begin{aligned} \vec{\rho}_1 &= \frac{1}{d_{12}}\left[\vec{r}_2 - \vec{r}_1\right], \\ \vec{\rho}_2 &= d_{12}\left[\vec{r}_3 - \frac{m_1\vec{r}_1 + m_2\vec{r}_2}{m_1+m_2}\right], \end{aligned} \tag{2.1}$$

where $\vec{r}_i$ is the position of particle i with mass m_i, and the mass-weighting factor d is given by

$$\begin{aligned} d_{ij}^2 &= \frac{m_k\left(m_i+m_j\right)}{\mu_{3b}\left(m_i+m_j+m_k\right)}, \\ \mu_{3b}^2 &= \frac{m_1 m_2 m_3}{m_1+m_2+m_3}. \end{aligned} \tag{2.2}$$

Here, μ_{3b} is the three-body reduced mass. In the case of three identical particles, $d_{12} = d_{23} = d_{31} = 2^{1/2}/3^{1/4}$ and $\mu_{3b} = m/\sqrt{3}$, where $m_1 = m_2 = m_3 = m$ is the mass of a single particle. The hyperradius R describing the overall size of the system can be defined as

$$R^2 = \rho_1^2 + \rho_2^2, \tag{2.3}$$

where $R \in [0, \infty)$. The two hyperangles (θ, φ) describing the shape of the system are defined by

$$\begin{aligned} \left(\vec{\rho}_1\right)_x &= R\cos\left(\theta/2-\pi/4\right)\sin\left(\varphi/2+\pi/6\right), \\ \left(\vec{\rho}_1\right)_y &= R\sin\left(\theta/2-\pi/4\right)\cos\left(\varphi/2+\pi/6\right), \\ \left(\vec{\rho}_1\right)_z &= 0, \\ \left(\vec{\rho}_2\right)_x &= R\cos\left(\theta/2-\pi/4\right)\sin\left(\varphi/2+\pi/6\right), \\ \left(\vec{\rho}_2\right)_y &= -R\sin\left(\theta/2-\pi/4\right)\sin\left(\varphi/2+\pi/6\right), \\ \left(\vec{\rho}_2\right)_z &= 0. \end{aligned} \tag{2.4}$$

Here, x, y, z are body frame axes that refer to the principal axes of the body frame whose orientation is specified by the Euler angles (α, β, γ): the z axis is parallel to $\vec{\rho}_1 \times \vec{\rho}_2$, and the x axis is associated with the smallest moment of inertia. The hyperangle θ spans the ranges $[0, \pi/2]$ and the hyperangle φ spans the range $[0, 2\pi)$, after requring the wave function to be single valued. The hyperangle φ can be further restricted to a smaller range if two or more particles are indistinguishable [47].

Usually, the three-body interaction $V\left(R, \theta, \varphi\right)$ can be expressed as a function of the interparticle distances $V\left(R, \theta, \varphi\right) = \widetilde{V}\left(r_{12}, r_{23}, r_{31}\right)$. For three identical particles, the interparticle distances r_{ij} can be expressed in terms of hyperspherical coordinates [47, 48, 49, 50, 51], where

$$r_{12} = 3^{-1/4} R\left[1+\sin\theta\sin\left(\varphi-\pi/6\right)\right]^{1/2},$$

$$r_{23} = 3^{-1/4} R \left[1 + \sin\theta \sin\left(\varphi - 5\pi/6\right)\right]^{1/2}, \tag{2.5}$$

$$r_{31} = 3^{-1/4} R \left[1 + \sin\theta \sin\left(\varphi + \pi/2\right)\right]^{1/2}.$$

The three-body Schrödinger equation in this hyperspherical representation can then be written as

$$\left\{-\frac{\hbar^2}{2\mu_{3b}}\left[\frac{1}{R^5}\frac{\partial}{\partial R}R^5\frac{\partial}{\partial R} - \frac{\Lambda^2\left(\theta,\varphi\right)}{R^2}\right] + V\left(R,\theta,\varphi\right)\right\}\Psi = E\Psi, \tag{2.6}$$

where Λ^2 is the "grand angular-momentum operator" [52] defined as

$$\frac{\Lambda^2}{2\mu_{3b}R^2} = T_\theta + T_{\varphi C} + T_r, \tag{2.7}$$

where

$$T_\theta = -\frac{2}{\mu_{3b}R^2\sin 2\theta}\frac{\partial}{\partial\theta}\sin 2\theta\frac{\partial}{\partial\theta}, \tag{2.8}$$

$$T_{\varphi C} = \frac{2}{\mu_{3b}R^2\sin^2\theta}\left(i\frac{\partial}{\partial\varphi} - \cos\theta\frac{J_z}{2}\right)^2, \tag{2.9}$$

and

$$T_r = \frac{J_x^2}{\mu_{3b}R^2\left(1-\sin\theta\right)} + \frac{J_y^2}{\mu_{3b}R^2\left(1+\sin\theta\right)} + \frac{J_z^2}{2\mu_{3b}R^2}. \tag{2.10}$$

The operators (J_x, J_y, J_z) are the body-frame components of the total angular momentum of the system. One convenient transformation is to introduce a rescaled wave function $\psi_E = R^{5/2}\Psi$. The Schrödinger equation for ψ_E then becomes,

$$\left\{-\frac{\hbar^2}{2\mu_{3b}}\left[\frac{\partial^2}{\partial R^2} - \frac{\Lambda^2\left(\theta,\varphi\right)+15/4}{R^2}\right] + V\left(R,\theta,\varphi\right)\right\}\psi_E = E\psi_E. \tag{2.11}$$

The volume element relevant to integrals over $|\psi_E|^2$ is $2dR\sin 2\theta d\theta d\varphi d\alpha \sin\beta d\beta d\gamma$.

2.2 Adiabatic hyperspherical representation

Solving the Schödinger equation [Eq.(2.11)] directly should in principle provide accurate results for three-body problems, but it would require extensive computational time and memory to diagonalize the full Hamiltonian matrix. Instead, we break the problem into two steps: first solve the hyperangular Schödinger equation in the adiabatic representation, and then later include the

nonadiabatic coupling. The adiabatic hyperspherical representation is a numerically efficient and stable way to solve the three-body Schrödinger equation [Eq. (2.11)]. It is currently a standard method. The first step in solving the three-body Schrödinger equation is to find the adiabatic potentials and channel functions, which are defined as solutions of the adiabatic eigenvalue equations

$$H_{\mathrm{ad}}\left(R,\Omega\right)\Phi_{\nu}\left(R;\Omega\right)=U_{\nu}\left(R\right)\Phi_{\nu}\left(R;\Omega\right), \tag{2.12}$$

whose solutions depend parametrically on R. Here, Ω denotes the Euler angles and the two hyperspherical angles. The adiabatic Hamiltonian, containing **all** angular dependence and interactions, is defined as

$$H_{\mathrm{ad}}\left(R,\Omega\right)=\left[\frac{\hbar^{2}\Lambda^{2}}{2\mu_{3b}R^{2}}+\frac{15\hbar^{2}}{8\mu_{3b}R^{2}}+V\left(R,\theta,\varphi\right)\right]. \tag{2.13}$$

Therefore, the adiabatic potentials and nonadiabatic couplings obtained by solving Eq. (2.12) for fixed values of R contain all the correlations relevant to this problem. For each R, the set of $\Phi_{\nu}\left(\Omega;R\right)$ is orthogonal,

$$\int d\Omega\Phi_{\mu}\left(R;\Omega\right)^{*}\Phi_{\nu}\left(R;\Omega\right)=\delta_{\mu\nu}, \tag{2.14}$$

and complete

$$\sum_{\tau}\Phi_{\tau}\left(R;\Omega\right)\Phi_{\tau}\left(R;\Omega'\right)^{*}=\delta\left(\Omega-\Omega'\right). \tag{2.15}$$

In practice, calculating all the channel functions is time consuming and impractical. However, numerical studies show that only a small number of channels are needed as a truncated set of the basis to expand the whole wave function, e.g.,

$$\psi_{E}\left(R,\Omega\right)=\sum_{\nu=1}^{N_{c}}F_{\nu}^{E}\left(R\right)\Phi_{\nu}\left(\Omega;R\right), \tag{2.16}$$

where $\Omega=\{\alpha,\beta,\gamma,\theta,\varphi\}$ denotes the Euler angles and the two hyperspherical angles, N_c is the number of channels adopted. Insertion of Eq. (2.16) into Eq. (2.11) leads to a set of coupled one-dimensional equations:

$$\left[-\frac{\hbar^{2}}{2\mu_{3b}}\frac{d^{2}}{dR^{2}}+U_{\nu}\left(R\right)-E\right]F_{\nu\nu'}^{E}\left(R\right)-\frac{\hbar^{2}}{2\mu_{3b}}\sum_{\mu}\left[2P_{\nu\mu}\left(R\right)\frac{d}{dR}+Q_{\nu\mu}\left(R\right)\right]F_{\mu\nu'}^{E}\left(R\right)=0, \tag{2.17}$$

where $\underline{P}$ and $\underline{Q}$ are the coupling matrices defined below, and ν' denotes the $\nu'-$th independent solution. (Hereafter, unless otherwise specified, we use an underline to denote the matrix form, e.g., $\underline{P}$ denotes a matrix with matrix element $P_{\nu\mu}$.) Numerically, if there are N_c coupled equations, then there are N_c independent solutions in general, before imposing any boundary condition at $R \to \infty$. For a scattering calculation, these solutions can be used to compute the R-matrix ($\underline{\mathcal{R}}$); this $\underline{\mathcal{R}}$ is a fundamental quantity that can be subsequently used to determine the scattering matrix $\underline{S}$, which is the main goal of the scattering study [see Eqs. (2.21) and (2.22) below]. As usual, the R-matrix $\underline{\mathcal{R}}$ is defined for some large, fixed radius R as

$$\underline{\mathcal{R}}(R) = \underline{F}(R)\left[\underline{\widetilde{F}}(R)\right]^{-1}, \tag{2.18}$$

where matrices $\underline{F}$ and $\underline{\widetilde{F}}$ are given in terms of the solutions of Eqs. (2.11) and (2.12) by:

$$F_{\nu\nu'}(R) = \int d\Omega \Phi_\nu(\Omega;R)^* \psi_{\nu'}(\Omega,R), \tag{2.19}$$

$$\widetilde{F}_{\nu\nu'}(R) = \int d\Omega \Phi_\nu(\Omega;R)^* \frac{\partial}{\partial R}\psi_{\nu'}(\Omega,R). \tag{2.20}$$

Once we have the R-matrix at large distances, the physical scattering matrix $\underline{\mathcal{S}}$ (and its close relative, the reaction matrix $\underline{\mathcal{K}}$) can be simply determined by applying asymptotic boundary conditions [53], i.e.,

$$\underline{\mathcal{K}} = \left(\underline{f} - \underline{f}'\underline{\mathcal{R}}\right)\left(\underline{g} - \underline{g}'\underline{\mathcal{R}}\right)^{-1}, \tag{2.21}$$

$$\underline{\mathcal{S}} = \left(\underline{1} + i\underline{\mathcal{K}}\right)\left(\underline{1} - i\underline{\mathcal{K}}\right)^{-1}, \tag{2.22}$$

where $\underline{f}$, $\underline{f}'$, $\underline{g}$ and $\underline{g}'$ are diagonal matrixes whose matrix elements are the energy-normalized asymptotic solutions f_ν, g_ν and their derivatives f'_ν, g'_ν, respectively. f_ν and g_ν are given in terms of spherical Bessel functions: $f_\nu(R) = (2\mu_{3b}k_\nu/\pi)^{1/2} R j_{l_\nu}(k_\nu R)$, $g_\nu(R) = (2\mu_{3b}k_\nu/\pi)^{1/2} R n_{l_\nu}(k_\nu R)$, where k_ν and l_ν are determined by the asymptotic behavior of the potential in Eqs. (2.28-2.29).[1] In general, $\underline{\mathcal{R}}$ is symmetric, which guarantees that $\underline{\mathcal{K}}$ is symmetric and $\underline{\mathcal{S}}$ is unitary (see Appendix A).

[1] For the f'th recombination channel, l_f is given by Eq. (4.5), and $k_f = \sqrt{2\mu_{3b}\left(E - E_{2b}^{(f)}\right)}$. For the i'th three-body break-up channel, $l_i = \lambda_i + 3/2$, and $k_i = \sqrt{2\mu_{3b}E}$.

For a bound state calculation, we need to apply the boundary condition that the wave function vanishes at $R \to \infty$. The eigen-energy will be quantized, and only one solution (denoted as $F_\nu^{E_i}$) survives for a given eigen energy E_i.

2.3 Coupling matrices

In Eq. (2.17), the coupling matrices describing nonadiabatic coupling are critical for a quantitative calculation. They are defined as

$$P_{\nu\mu}(R) = \int d\Omega \Phi_\nu(R;\Omega)^* \frac{\partial}{\partial R} \Phi_\mu(R;\Omega), \tag{2.23}$$

$$Q_{\nu\mu}(R) = \int d\Omega \Phi_\nu(R;\Omega)^* \frac{\partial^2}{\partial R^2} \Phi_\mu(R;\Omega). \tag{2.24}$$

In practice, only the

$$P_{\nu\mu}^2(R) = -\int d\Omega \frac{\partial}{\partial R} \Phi_\nu(R;\Omega)^* \frac{\partial}{\partial R} \Phi_\mu(R;\Omega), \tag{2.25}$$

component of $Q_{\nu\mu}$ (see the Appendix B) is needed to solve the coupled equations. The relation between $\underline{Q}$ and $\underline{P}$ is given by $\frac{d}{dR}\underline{P} = -\underline{P^2} + \underline{Q}$. From the definition of the $\underline{P}$ and $\underline{Q}$ matrices, it is easy to see that the coupling matrices have the following properties: $P_{\nu\mu} = -P_{\mu\nu}$ and $P_{\nu\mu}^2 = P_{\mu\nu}^2$, which leads to $P_{\nu\nu} = 0$, and $Q_{\nu\nu} = -P_{\nu\nu}^2$. We usually define a matrix as the addition of the coupling to the potential, with the matrix elements being

$$W_{\nu\mu}(R) = U_\nu(R)\,\delta_{\nu\mu} - \frac{\hbar^2}{2\mu_{3b}} \left[2P_{\nu\mu}(R) \frac{d}{dR} + Q_{\nu\mu}(R) \right]. \tag{2.26}$$

The diagonal terms of this matrix

$$\widetilde{U}_\nu(R) \equiv W_{\nu\nu}(R) = U_\nu(R) - \frac{\hbar^2}{2\mu_{3b}} P_{\nu\nu}^2(R), \tag{2.27}$$

are called "adiabatic potentials with diagonal correction" or "effective potentials". The effective potentials are usually more physical than the adiabatic potentials. They describe the system better. For example, the effective potential gives physical asymptotic behaviors of the system at large R. In the case of three particles with only short-range interactions, the zero energy of the system can be

defined as the energy of three stationary particles that are infinitely far away from each other (the three-body break up threshold). The effective potentials can then be classified into two categories.

The potential curves converging to asymptotic limiting values below the three-body threshold at very large R are called recombination channels. These recombination channels have asymptotic behavior at large R as,

$$\widetilde{U}_{\nu}(R) \overset{R\to\infty}{\approx} \frac{l_{\nu}(l_{\nu}+1)}{2\mu_{3b}R^{2}} + E_{2b}^{(\nu)}, \tag{2.28}$$

where $E_{2b}^{(\nu)}$ is the two-body bound-state (dimer) energies, and l_{ν} is the corresponding angular momentum of the third particle relative to the dimer. One can easily see that these recombination channels have a strong "dimer plus atom" character; they are sometimes called $2+1$ channels.

The potential curves above the three-body threshold at very large R are called the three-body break-up channels. Their asymptotic behavior is described by

$$\widetilde{U}_{\nu}(R) \overset{R\to\infty}{\approx} \frac{\lambda_{\nu}(\lambda_{\nu}+4)+15/4}{2\mu_{3b}R^{2}}, \tag{2.29}$$

where $\lambda_{\nu}(\lambda_{\nu}+4)$ is the eigenvalue of the grand angular momentum operator Λ^{2}. In the large R limit, the corresponding eigenstates will be hyperspherical harmonics. Therefore, these channels have a strong "atom plus atom plus atom" character, and are sometimes called $1+1+1$ channels.

In addition, the asymptotic values of the coupling matrix elements in the large R limit also obey some simple power laws of R [54, 55]. Therefore, we usually calculate the values of these matrix elements at large R then fit them with power law expansions, and extrapolate them to a even larger distance, if desired.

A traditional method for calculating the coupling matrices is to apply a simple differencing scheme for the derivative of $\Phi_{\mu}(R;\Omega)$, i.e.,

$$\frac{\partial}{\partial R}\Phi_{\mu}(R;\Omega) \approx \frac{\Phi_{\mu}(R+\Delta R;\Omega)-\Phi_{\mu}(R-\Delta R;\Omega)}{2\Delta R}. \tag{2.30}$$

However, this scheme is only accurate up to the first order of ΔR. In addition, the value chosen for ΔR in a realistic numerical calculation can sometimes be tricky. When $\Phi_{\mu}(R;\Omega)$ changes very rapidly, e.g., near a sharp avoided crossing, we need to choose a very small step size ΔR. In

contrast, when $\Phi_\mu(R;\Omega)$ changes very slowly, e.g., at very large distances R, we need to choose a relatively larger step size ΔR, or else $\Phi_\mu(R+\Delta R;\Omega)-\Phi_\mu(R-\Delta R;\Omega)$ would be too small, and the accuracy would be limited by the machine precision.

One way to improve the accuracy is to apply the Hellmann–Feynman theorem. The Hellmann–Feynman theorem can give us analytical formulas for the coupling matrices if we know the derivative of the adiabatic Hamiltonian $\frac{\partial}{\partial R}H_{\rm ad}$ from the following derivation. First, taking the derivative of both sides of Eq. (2.12) leads to

$$\left[H_{\rm ad}(R,\Omega)-U_\nu(R)\right]\frac{\partial}{\partial R}\Phi_\nu(R;\Omega)=-\left[\frac{\partial}{\partial R}H_{\rm ad}(R,\Omega)-\frac{\partial}{\partial R}U_\nu(R)\right]\Phi_\nu(R;\Omega). \tag{2.31}$$

Next, multiplying $\Phi_\mu(R;\Omega)^*$ on both sides of Eq. (2.31) and integrating over Ω gives

$$P_{\mu\nu}=\int d\Omega\Phi_\mu(R;\Omega)^*\frac{\partial}{\partial R}\Phi_\nu(R;\Omega)=-\frac{\int d\Omega\Phi_\mu(R;\Omega)^*\left[\frac{\partial}{\partial R}H_{\rm ad}(R,\Omega)\right]\Phi_\nu(R;\Omega)}{\left[U_\mu(R)-U_\nu(R)\right]}, \tag{2.32}$$

where $\mu\neq\nu$, and

$$\frac{\partial}{\partial R}U_\nu(R)=\int d\Omega\Phi_\nu(R;\Omega)^*\left[\frac{\partial}{\partial R}H_{\rm ad}(R,\Omega)\right]\Phi_\nu(R;\Omega) \tag{2.33}$$

after some manipulation of algebra. The Hellmann–Feynman theorem is believed to be numerically exact (assuming that the numerical basis expansion for Ω is complete enough). The matrix elements for P^2 can be obtained by

$$P^2_{\mu\nu}=\sum_{\tau=1}^{N_c}P_{\mu\tau}P_{\tau\nu}, \tag{2.34}$$

where N_c is the number of channels. However, numerical studies show that the convergence of $P^2_{\mu\nu}$ with respect to number of channels is very slow, making this method impractical.

We now introduce a new method to calculate $\frac{\partial}{\partial R}\Phi_\mu(R;\Omega)$. It is numerically exact (again, assuming that the numerical basis expansion for Ω are complete enough). The first hint of the derivations of this method is that Eq. (2.31) seems plausible to be directly solved for $\frac{\partial}{\partial R}\Phi_\mu(R;\Omega)$ by

$$\frac{\partial}{\partial R}\Phi_\nu(R;\Omega)=-\left[H_{\rm ad}(R,\Omega)-U_\nu(R)\right]^{-1}\left[\frac{\partial}{\partial R}H_{\rm ad}(R,\Omega)-\frac{\partial}{\partial R}U_\nu(R)\right]\Phi_\nu(R;\Omega). \tag{2.35}$$

However, this solution is forbidden since $H_{\mathrm{ad}}(R,\Omega)-U_{\nu}(R)$ is singular:

$$|H_{\mathrm{ad}}(R,\Omega)-U_{\nu}(R)|=0 \tag{2.36}$$

meaning that $H_{\mathrm{ad}}(R,\Omega)-U_{\nu}(R)$ is not invertible. The singularity can also be understood from the fact that the equation

$$\left[H_{ad}(R,\Omega)-U_{\nu}(R)\right]\chi_{\nu}(R;\Omega)=-\left[\frac{\partial}{\partial R}H_{ad}(R,\Omega)-\frac{\partial}{\partial R}U_{\nu}(R)\right]\Phi_{\nu}(R;\Omega) \tag{2.37}$$

does not have a unique solution, $\chi_{\nu}(R;\Omega)$. In fact, any functions with the form of

$$\chi_{\nu}(R;\Omega)=\frac{\partial}{\partial R}\Phi_{\nu}(R;\Omega)+c\Phi_{\nu}(R;\Omega), \tag{2.38}$$

(where c is an arbitrary number) can be a solution of Eq. (2.37). The singularity of matrix $H_{\mathrm{ad}}(R,\Omega)-U_{\nu}(R)$ can be removed by considering the additional condition that

$$\int d\Omega\Phi_{\nu}(R,\Omega)^{*}\frac{\partial}{\partial R}\Phi_{\nu}(R,\Omega)=0, \tag{2.39}$$

which can be derived from the normalization condition of $\Phi_{\nu}(R,\Omega)$, as shown in Ref. [56]. Nevertheless, our numerical studies show that even without removing the singularity, applying numerical solver packages such as "Linear Algebra PACKage" (LAPACK) [57] or PARDISO [58] to solve Eq. (2.37) directly can still give an accurate solution $\chi_{\nu}(R;\Omega)$ in the form of Eq. (2.38) with an unknown c. And once we have the numerical solution $\chi_{\nu}(R;\Omega)$, c can be calculated by

$$c=\int d\Omega\Phi_{\nu}(R;\Omega)^{*}\chi_{\nu}(R;\Omega). \tag{2.40}$$

Finally, the derivative of $\Phi_{\nu}(R;\Omega)$ can be written as

$$\frac{\partial}{\partial R}\Phi_{\nu}(R;\Omega)=\chi_{\nu}(R;\Omega)-c\Phi_{\nu}(R;\Omega), \tag{2.41}$$

which can be inserted into Eq. (2.23) and Eq. (2.25) for the coupling matrices. The P matrices obtained in this way are found to be numerically the same as the one calculated from the Hellmann–Feynman theorem up to machine precision, proving that our $\frac{\partial}{\partial R}\Phi_{\nu}(R;\Omega)$ are numerically accurate. Therefore, this method can give numerically very accurate coupling matrices.

2.4 Slow variable discretization (SVD) method

The traditional method using Eq. (2.17) works well, however, only when $P_{\nu\mu}(R)$ and $Q_{\nu\mu}(R)$ are smooth functions of R. In this case, the $\underline{P}$ and $\underline{Q}$ (actually $\underline{P^2}$) matrices can be calculated on a sparse grid and then interpolated and/or extrapolated on a much denser grid and even larger distances. Clearly, this scheme suffers from tremendous numerical difficulties arising from sharp nonadiabatic avoided crossings. In that case, the SVD approach offers a much more stable and accurate approach for solving Eq. (2.11). One key ingredient for implementing the SVD approach is the use of the discrete variable representation (DVR) [59, 60]. Our DVR basis functions $\pi_i(R)$ are defined by the Gauss-Lobatto quadrature points x_i and weights w_i [61]. This quadrature approximates integrals of a function $g(x)$ as

$$\int_{-1}^{1} g(x)dx \cong \sum_{i=1}^{N} g(x_i)w_i. \tag{2.42}$$

After scaling the quadrature points and weights, the above equation is generalized to treat definite integrals over an arbitrary interval $R \in [a_1, a_2]$:

$$\int_{a_1}^{a_2} g(R)\, dR \cong \sum_{i=1}^{N} g(R_i)\widetilde{w}_i, \tag{2.43}$$

where

$$\widetilde{w}_i = \frac{a_2 - a_1}{2} w_i, R_i = \frac{a_2 + a_1}{2} x_i + \frac{a_2 - a_1}{2}. \tag{2.44}$$

Equation (2.43) is exact for polynomials whose degree is less than or equal to $2N-1$. We construct the DVR basis functions as

$$\pi_i(R) = \sqrt{\frac{1}{\widetilde{w}_i}} \prod_{j \neq i}^{N} \frac{R - R_j}{R_i - R_j}, \tag{2.45}$$

which have the important property that

$$\pi_i(R_j) = \sqrt{\frac{1}{\widetilde{w}_i}} \delta_{ij}. \tag{2.46}$$

Hence, over an interval $R \in [a_1, a_2]$, the DVR approximation based on quadrature gives

$$\int_{a_1}^{a_2} \pi_i(R)\, H(R)\, \pi_j(R)\, dR \cong H(R_i)\, \delta_{ij} \tag{2.47}$$

for matrix elements of any function $H(R)$, which is usually called the DVR approximation.

2.4.1 Bound-state calculations

This subsection discusses the implementation of SVD in bound-state calculations. The solution $\psi_{\nu'}$ is expanded in the radial DVR basis $\pi_n(R)$ and in hyperangles in terms of the adiabatic hyperspherical channel functions as

$$\psi_{E_i}(R,\Omega) = \sum_{\nu,n} c^i_{n\nu} \pi_n(R)\, \Phi_\nu(\Omega; R_n). \tag{2.48}$$

It is now possible to rewrite Eq.(2.11) under the DVR approximation Eq. (2.47) as

$$\sum_{n,\mu} T_{nn'} O_{n\nu,n'\mu} c^i_{n'\mu} + [U_\nu(R_n) - E_i]\, c^i_{n\nu} = 0, \tag{2.49}$$

where

$$T_{nn'} = \int dR \pi_n(R) \left[-\frac{1}{2\mu}\frac{\partial^2}{\partial R^2}\right] \pi_{n'}(R)\, dR, \tag{2.50}$$

and $O_{n\nu,n'\mu}$ is the overlap matrix given by

$$O_{n\nu,n'\mu} = \int d\Omega \Phi_\nu(\Omega; R_n)^* \Phi_\mu(\Omega; R_{n'}). \tag{2.51}$$

Finally, Eq.(2.49) is solved for the expansion coefficients $c^i_{n\nu}$ and E_i.

2.4.2 Scattering calculations

In our scattering calculations, the R-matrix propagation method is combined with the SVD approach (following the logic of Ref. [62]) and uses the DVR basis given by Eq. (2.45). For a given R-matrix [Eq. (2.18)] at $R = a_1$, one uses the R-matrix propagation method to calculate the corresponding R-matrix at another point $R = a_2$, as follows. The solution $\psi_{\nu'}$ is expanded in the radial DVR basis $\pi_j(R)$ and in hyperangles in terms of the adiabatic hyperspherical channel functions as

$$\psi_{\nu'}(R,\Omega) = \sum_{j\mu} c_{j\mu,\nu'} \pi_j(R)\, \Phi_\mu(\Omega; R_j), \tag{2.52}$$

where $\Phi_\nu(\Omega; R_j)$ is the $\nu-$th hyperspherical adiabatic channel function calculated at $R = R_j$.

Substituting Eq. (2.52) into Eq. (2.19) yields the values of the matrix elements of $F_{\nu\nu'}$ and $\widetilde{F}_{\nu\nu'}$ at the $R = a_1$ and $R = a_2$ boundaries in terms of the coefficients of Eq. (2.52):

$$F_{\nu\nu'}(a_1) = \sum_j c_{j\nu,\nu'}\pi_j(a_1), \tag{2.53}$$

$$F_{\nu\nu'}(a_2) = \sum_j c_{j\nu,\nu'}\pi_j(a_2), \tag{2.54}$$

$$\widetilde{F}_{\nu\nu'}(a_1) = \sum_{j\mu} c_{j\mu,\nu'} O^{1j}_{\nu\mu}\pi'_j(a_1), \tag{2.55}$$

$$\widetilde{F}_{\nu\nu'}(a_2) = \sum_{j\mu} c_{j\mu,\nu'} O^{Nj}_{\nu\mu}\pi'_j(a_2), \tag{2.56}$$

where $O^{ij}_{\nu\mu}$ are the overlap matrix elements, and

$$O^{ji}_{\nu\mu} = \int d\Omega \Phi_\nu(\Omega; R_j)^* \Phi_\mu(\Omega; R_i). \tag{2.57}$$

Note that the determination of $\underline{F}$ and $\underline{\tilde{F}}$ according to the above expressions only depends on derivatives of the well-behaved DVR basis $[\pi'_j(R)]$. Therefore, this approach is much better suited for handling the complex structure of avoided crossings present in systems.

Over an interval $R \in [a_1, a_2]$, the DVR approximation gives

$$\int_{a_1}^{a_2} \pi_i(R) H_{\rm ad}(R,\Omega) \pi_j(R) dR \approx H_{\rm ad}(R_i,\Omega)\delta_{ij}. \tag{2.58}$$

Expansion of the Schrödinger equation in the same numerical basis functions as in Eq. (2.52) and integration by parts yields the equation for the expansion coefficients $c_{j\mu,\nu'}$ (in vector notation, $\vec{c}_{\nu'}$) as

$$\left[\widetilde{H} - E\right]\vec{c}_{\nu'} = L\vec{c}_{\nu'}, \tag{2.59}$$

or, equivalently,

$$\vec{c}_{\nu'} = \left[\widetilde{H} - E\right]^{-1} L\vec{c}_{\nu'}. \tag{2.60}$$

Here, the matrix elements of $\widetilde{H}$ and L are given by

$$\widetilde{H}_{i\nu,j\mu} = \frac{1}{2\mu_{3b}}\left[\int_{a_1}^{a_2} \frac{d\pi_i(R)}{dR}\frac{d\pi_j(R)}{dR}dR\right] O^{ij}_{\nu\mu} + U_\nu(R_i)\delta_{\nu\mu}\delta_{ij}, \tag{2.61}$$

$$L_{i\nu,j\mu} = \frac{1}{2\mu_{3b}}\left[\pi_i(R)\frac{d\pi_j(R)}{dR}O^{ij}_{\nu\mu}\right]\Bigg|_{a_1}^{a_2}. \tag{2.62}$$

Diagonalizing $\widetilde{H}$ over the range $[a_1, a_2]$ gives,

$$\vec{x_n}^T \widetilde{H} \vec{x_n'} = \varepsilon_n \delta_{n,n'}, \tag{2.63}$$

and the completeness relation of $\vec{x}_n$,

$$\sum_n \vec{x}_n \vec{x}_n^T = \underline{1}, \tag{2.64}$$

where $\underline{1}$ is an identity matrix. Equation (2.60) is then rewritten as

$$\vec{c}_{\nu'} = \left[\widetilde{H} - E\right]^{-1} \sum_n \vec{x}_n \vec{x}_n^T L \vec{c}_{\nu'} = \sum_n \frac{\vec{x}_n \vec{x}_n^T}{\varepsilon_n - E} L \vec{c}_{\nu'}. \tag{2.65}$$

Substitution of the matrix elements of L from Eq. (2.62) and insertion of the definition of $F_{\nu\nu'}$ and $\widetilde{F}_{\nu\nu'}$ at a_1 and a_2 into Eq. (2.53) finally gives

$$F_{\nu\nu'}(a_1) = \sum_{n\mu} \frac{u_\nu^{(n)}(a_1)\, u_\mu^{(n)}(a_2)}{2\mu_{3b}(\varepsilon_n - E)} \widetilde{F}_{\mu\nu'}(a_2) - \sum_{n\mu} \frac{u_\nu^{(n)}(a_1)\, u_\mu^{(n)}(a_1)}{2\mu_{3b}(\varepsilon_n - E)} \widetilde{F}_{\mu\nu'}(a_1), \tag{2.66}$$

$$F_{\nu\nu'}(a_2) = \sum_{n\mu} \frac{u_\nu^{(n)}(a_2)\, u_\mu^{(n)}(a_2)}{2\mu_{3b}(\varepsilon_n - E)} \widetilde{F}_{\mu\nu'}(a_2) - \sum_{n\mu} \frac{u_\nu^{(n)}(a_2)\, u_\mu^{(n)}(a_1)}{2\mu_{3b}(\varepsilon_n - E)} \widetilde{F}_{\mu\nu'}(a_1), \tag{2.67}$$

where,

$$u_\nu^{(n)}(R) = \sum_j x_{j\nu,n} \pi_j(R), \tag{2.68}$$

and $x_{j\nu,n}$ are elements of the vector $\vec{x}_n$.

Our next step introduces the following matrices

$$(\underline{\mathcal{R}}_{11})_{\nu\mu} = \sum_{n\mu} \frac{u_\nu^{(n)}(a_1)\, u_\mu^{(n)}(a_1)}{2\mu_{3b}(\varepsilon_n - E)}, \tag{2.69}$$

$$(\underline{\mathcal{R}}_{12})_{\nu\mu} = \sum_{n\mu} \frac{u_\nu^{(n)}(a_1)\, u_\mu^{(n)}(a_2)}{2\mu_{3b}(\varepsilon_n - E)}, \tag{2.70}$$

$$(\underline{\mathcal{R}}_{21})_{\nu\mu} = \sum_{n\mu} \frac{u_\nu^{(n)}(a_2)\, u_\mu^{(n)}(a_1)}{2\mu_{3b}(\varepsilon_n - E)}, \tag{2.71}$$

$$(\underline{\mathcal{R}}_{22})_{\nu\mu} = \sum_{n\mu} \frac{u_\nu^{(n)}(a_2)\, u_\mu^{(n)}(a_2)}{2\mu_{3b}(\varepsilon_n - E)}. \tag{2.72}$$

After some manipulation, the matrix equation is finally obtained that determines the R-matrix propagation from a_1 to a_2:

$$\underline{\mathcal{R}}(a_2) = \underline{\mathcal{R}}_{22} - \underline{\mathcal{R}}_{21} \left[\underline{\mathcal{R}}_{11} + \underline{\mathcal{R}}(a_1)\right]^{-1} \underline{\mathcal{R}}_{12}. \tag{2.73}$$

In the SVD method, the overlap matrix $O^{ji}_{\nu\mu}$ requires us to calculate the channel functions $\Phi_\nu(\Omega; R_j)$ at every grid point R_j, which can be very memory demanding if one needs to perform calculations over a broad range of R. At large distances, therefore, we apply the traditional adiabatic approach combined with the R-matrix propagation method. In the traditional adiabatic method, the P and Q matrixes can be calculated on a sparse grid, and then interpolated and/or extrapolated on a much denser grid and larger distances. This strategy makes the calculation faster and it also requires less memory. The main difference between the traditional adiabatic approach and the SVD method is the use of a different three-body numerical basis. The details of this traditional approach and its connection with the SVD method are discussed in Appendix B.

Chapter 3

Rovibrational states of $H_3{}^+$ and quantum-defect analysis of H_3 Rydberg states

In this chapter, the hyperspherical approach is used to study rovibrational states of triatomic hydrogen ion (H_3^+). These rovibrational states have important applications in a multichannel quantum defect theory (MQDT) analysis of Rydberg energy levels of the triatomic hydrogen molecule (H_3). In MQDT, interactions between the Rydberg electron and the ion core H_3^+ are described by quantum defects. We extract the body-frame p-wave quantum defects from highly accurate **ab initio** electronic potential surfaces and calculate the quantum defects of higher angular momentum states in a long-range multipole potential model. Laboratory-frame quantum defect matrices emerge from a rovibrational-frame transformation carried out with accurate rovibrational states of H_3^+. Finally, the laboratory-frame quantum defects are used to calculate $3p$ and $3d$ Rydberg energy levels for the fundamental neutral triatomic molecule H_3. In addition, calculations of radiative transitions for higher Rydberg states give explanations for a recent experiment. In this experiment, mid-infrared laser lines observed in hydrogen/rare gas discharges are assigned to three-body recombination processes involving an electron, a rare gas (He or Ne) atom, and the H_3^+ [44, 45]. A mechanism for the population inversion is proposed.

Note that the material in this chapter has been published in Ref. [63] and Ref. [45].

3.1 Introduction

The triatomic hydrogen molecule (H_3) plays an important role in astrophysics because its cation H_3^+ acts as a proton donor in chemical reactions occurring in interstellar clouds. As the

simplest triatomic neutral molecule, H_3 also attracts fundamental interest. Ever since its emission spectra were first observed by G. Herzberg in the 1980s [2, 3, 4, 5], H_3 has been studied extensively. Herzberg and co-workers measured infrared and visible emission spectra of H_3 in discharges through hydrogen and assigned them to Rydberg-Rydberg transitions between $n = 2$ and $n = 3$ electronic states using empirical fits [2, 3, 4, 5]. Helm and co-workers investigated the higher Rydberg states and ionization potentials of H_3 by analyzing the photoabsorption spectrum [64, 65]. In 2003, building on previous work of Schneider, Orel and Suzor-Weiner [66], it was shown [31, 67] that intermediate Rydberg states of H_3 play an important role in the dissociative recombination (DR) process, $H_3^+ + e^- \rightarrow H_3 \rightarrow H_2 + H$ or $H + H + H$. Prior to the study of Ref. [31, 67], the large discrepancy between the DR rate determined by experiment and previous theory had not been resolved. Refs. [31, 67] found that Jahn-Teller effects in H_3 neglected in previous theoretical studies couple the electronic and nuclear degrees of freedom and generate a relatively high DR rate via intermediate p-wave Rydberg-state pathways. A recent alternative formulation developed by Jungen and Pratt provides supporting evidence for this interpretation [68]. Vervloet and Watson improved both the experimental techniques and empirical fits and reinvestigated the low Rydberg states that G. Herzberg had observed [69]. Here we undertake an analysis of the Rydberg states with **ab initio** theory. One of the most successful techniques in treating Rydberg states by **ab initio** theory is MQDT [70, 71]. Earlier studies [31, 72, 73, 74] have utilized MQDT to successfully describe the DR process.

The application of MQDT to study molecular Rydberg energy levels treats the H_3 molecule as a Rydberg electron attached to a H_3^+ ion. The interaction between the Rydberg electron and the ion core is described through a smooth reaction matrix K or quantum defect matrix μ. K and μ are simply related, e.g., for a single-channel, $K = \tan(\pi\mu)$. We extract a body-frame reaction matrix from **ab initio** electronic potential surfaces for p-wave Rydberg states and calculate the body-frame reaction matrix for higher angular momentum states ($l > 1$) by using the long-range multipole potential model. For the higher angular-momentum states, we neglect short-range interactions due to the nonpenetrating nature of the high l states. Here l denotes the quantum number of

the Rydberg electron orbital angular momentum. We then construct the total laboratory-frame reaction matrix K through a rovibrational frame transformation, obtaining

$$K_{ii'} = \sum_{\alpha,\alpha'} \langle i|\ \alpha\rangle \tilde{K}_{\alpha\alpha'} \left\langle \alpha' \right|\ i' \rangle\,. \tag{3.1}$$

Here, $K_{ii'}$ is the laboratory-frame reaction matrix element between the laboratory-frame eigenchannels $|i\rangle$ and $|i'\rangle$, and $\tilde{K}_{\alpha\alpha'}$ is the body-frame reaction matrix element between body-frame eigenchannels $|\alpha\rangle$ and $|\alpha'\rangle$. The rovibrational frame transformation is specified by the unitary transformation $U_{i\alpha} = \langle i\ |\alpha\rangle$.

The process of constructing the rovibrational transformation is similar to that described in Ref. [31] and is based on the rovibrational wave functions of H_3^+. To calculate them, there are two important approximations adopted in Ref. [31], the rigid rotator approximation and the adiabatic hyperspherical approximation. The nonadiabatic coupling between different adiabatic hyperspherical channels was included in later studies by using the slow variable discretization (SVD) approach in Ref. [75, 76]. In the present study, we abandon the rigid rotator approximation and consider the Coriolis interaction. In this way, we obtain very accurate rovibrational energy levels and wave functions of H_3^+ that allow us to construct the rovibrational transformation.

After the rovibrational transformation described by Eq. (3.1) is carried out, we obtain the laboratory-frame K matrix and calculate the eigenenergies E of the H_3 molecule by solving the secular equation [53]

$$\det\left|\tan\left(\pi\nu\right) + K\right| = 0, \tag{3.2}$$

where ν is a diagonal matrix with elements $\nu_{ii} = 1/\sqrt{2\left(E_i - E\right)}$. Here E_i denotes the ith rovibrational energy level.

The remainder of the chapter is organized as follows. Section 3.2 describes the detailed calculation of rovibrational states of H_3^+ and shows how to use them to construct the rovibrational transformation. Section 3.3 describes the calculation of the p-wave energy levels of H_3 using **ab initio** quantum defects. Section 3.4 discusses the long-range multipole potential model for higher angular momentum Rydberg states, and Section 3.5 gives our conclusions.

3.2 Rovibrational states of H_3^+

In the cation H_3^+, three protons interact with each other under a potential surface $\widetilde{V}(r_{12}, r_{23}, r_{31})$. The potential surface was created by Refs. [77, 78, 79] and is sub-micro-hartree accurate. With this potential surface, the three-body Schrödinger equation is solved in the adiabatic hyperspherical representation.

In a previous study [31], two approximations are adopted: adiabatic hyperspherical approximation and rigid rotator approximation. The adiabatic hyperspherical approximation refers to neglecting coupling matrices in Eq. (2.11). Under this approximation, all the channels are decoupled with each other, and can be treated as a 1-D single channel problem. Rigid rotator approximation refers to neglecting the Coriolis interaction that couples rotational and vibrational dynamics. The vibrational energy are first calculated for $J = 0$, where the grand angular momentum operator can be simplified as,

$$\Lambda^2 = \frac{-4}{\sin 2\theta}\frac{\partial}{\partial\theta}\sin 2\theta\frac{\partial}{\partial\theta} - \frac{4}{\sin^2\theta}\frac{\partial^2}{\partial\varphi^2}. \tag{3.3}$$

The rotational energy are latter included approximately as the rotational energy of a rigid rotator, which only depends on the rotational quantum numbers and the moment of inertia.

Here, we improve both of these approximations: (1) using the SVD method to include the nonadiabatic couplings between different adiabatic channels, and (2) including the Coriolis interaction that couples rotational angular momentum with vibrational angular momentum by implementing the full "grand angular momentum operator".

3.2.1 Adiabatic representation

The first step is to solve Eq. (2.12) numerically for the adiabatic potentials and couplings. In order to do so, we expand $\Phi_\nu(\Omega; R)$ in a set of basis $\Phi_{jm_2K^+}^{N^+m^+g_I}$, such that

$$\Phi_\nu(\Omega; R) = \sum_{jm_2K^+} a_{jm_2K^+}^{(\nu)}(R)\,\Phi_{jm_2K^+}^{N^+m^+g_I}, \tag{3.4}$$

where j, m_2, N^+, K^+ and g_I are quantum numbers labeling basis functions in different degrees of freedom. $\Phi_{jm_2K^+}^{N^+m^+g_I}$ satisfies the permutation symmetry of a three-fermion system, e.g.,

$$P_{12}\Phi_{jm_2K^+}^{N^+m^+g_I} = -\Phi_{jm_2K^+}^{N^+m^+g_I}, \tag{3.5}$$

and

$$\mathcal{A}\Phi_{jm_2K^+}^{N^+m^+g_I} = \Phi_{jm_2K^+}^{N^+m^+g_I}, \tag{3.6}$$

where

$$\mathcal{A} = 1 - P_{12} - P_{23} - P_{31} + P_{12}P_{31} + P_{12}P_{23}. \tag{3.7}$$

The explicit form of the basis functions $\Phi_{jm_2K^+}^{N^+m^+g_I}$ is given in Appendix C. Expanding in these basis functions, Eq. (2.12) can be solved for the adiabatic potentials $U_\nu(R)$ and the channel functions $\Phi_\nu(\Omega; R)$.

For the purpose of illustration, Fig. 3.1 presents the lowest 60 hyperspherical adiabatic potentials of H_3^+. The total angular momentum of the system here is $N^+ = 1$, with odd parity and $g_I = 1$ (spin para state). Near $3 \leq R \leq 5$, these hyperspherical potentials show a series of avoid crossing, implying the existence of important nonadiabatic couplings between different channels. These couplings are included through the SVD method. The dashed line shows the position of the ground rovibrational level of the ion. This is in fact the lowest possible rovibrational state of H_3^+ shown in table 3.1 below.

Once $U_\nu(R)$ and $\Phi_\nu(\Omega; R)$ are obtained, the expansion coefficients $c_{n\nu}^i$ and E_i can be solved from Eq.(2.49). The total rovibrational wave function is therefore given by

$$\psi_{E_i}(R,\Omega) \equiv \Psi_{N^+m^+}^{v^+g_I\Pi^+}(R,\Omega) = \sum_{n\nu} c_{n\nu}^i \pi_n(R) \sum_{jm_2K^+} a_{jm_2K^+}^{(\nu)}(R_n)\, \Phi_{jm_2K^+}^{N^+m^+g_I}, \tag{3.8}$$

corresponding to the eigenenergy E_i. Here i is the set of good quantum numbers $N^+m^+v^+g_I\Pi^+$, where v^+ denotes the vibrational quantum numbers.

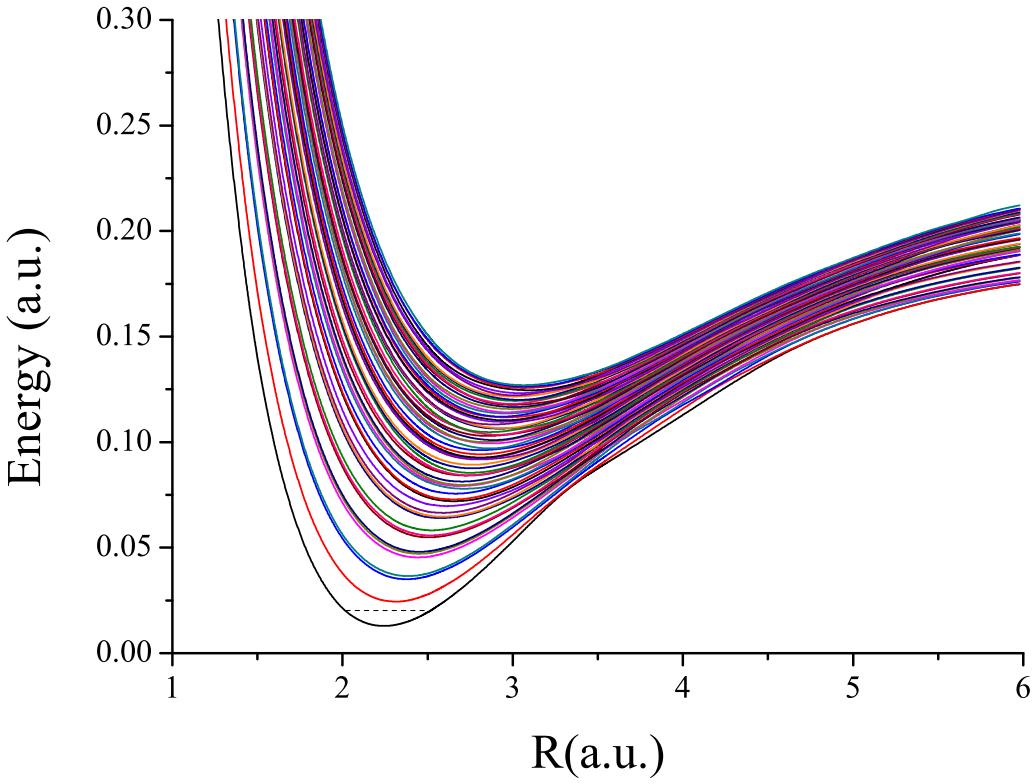

Figure 3.1: (Color online) Lowest 60 adiabatic potential curves $U(R)$ of H_3^+ with total angular momentum $N^+ = 1$, odd parity and $g_I = 1$. The dashed horizontal line shows the lowest rovibrational ground state of this system.

3.2.2 Accuracy of the rovibrational energies of H_3^+

Next we compare our theoretical rovibrational energy levels E_i of H_3^+ with experimental energy levels [1]. Adopting the notation used in Ref. [1], we label the rovibrational states i by quantum numbers $(N^+, G)\{v_1, v_2^{l_2}\}(l|u)$. v_1 is the symmetric-stretch vibrational quantum number, v_2 denotes the quantum number of the asymmetric-stretch mode, l_2 describes the quantum number of the vibrational angular momentum, and $G \equiv |K^+ - l_2|$. The fact that G instead of K^+ is a good quantum number implies that the Coriolis interaction couples rotational and vibrational angular momenta and makes levels with the same G nearly degenerate. However, for levels with $l_2 \neq 0$ and $(N^+ - |l_2|) \geq G \geq 1$, the degeneracy breaks, and we utilize u (or l) to denote the upper (or lower) energy level; these levels with a u or an l cannot be described by rigid rotator approximations.

Table 3.1 compares the rovibrational energy levels, calculated for $N^+ \leq 3$ states of $\{0, 0^0\}$ and $\{0, 1^1\}$ bands, with the experimental results of Lindsay and McCall [1]. The agreement is good, with a rms difference of 0.281 cm^{-1} for the levels shown in the table. Higher-rovibrational energy-level calculations also exhibit good agreement. For our calculated energy levels up to around 9000 cm^{-1} with $N^+ \leq 4$, the rms difference between our calculation and the experimental results of Ref. [1] is 0.657 cm^{-1}.

3.2.3 Rovibrational-frame transformation

Next we describe in detail how to construct the rovibrational-frame transformation using the ionic rovibrational eigenstates. In the laboratory frame, the $H_3^+ + e^-$ system is described by the electron orbital angular momentum l and its projection λ onto the laboratory z-axis, and by N^+, m^+, g_I, and parity of the ion core. Hence, we construct the wave function of the $H_3^+ + e^-$ system as a sum of products of the ionic rovibrational wave function and electronic wave function, of the form

$$\Psi_{N^+m^+}^{v^+ g_I \Pi^+}(R, \Omega)\, Y_{l\lambda}(\theta_e, \varphi_e)\,, \tag{3.9}$$

Table 3.1: Comparison of several calculated rovibrational energy levels of H_3^+ with experimental results [1]. Only states with $N^+ \leq 3$ for the $\{0, 0^0\}$ and $\{0, 1^1\}$ bands are shown here.

Q.N.[1]	E_{cal}[2] (cm^{-1})	E_{exp}[3] (cm^{-1})	Q.N.[1]	E_{cal}[2] (cm^{-1})	E_{exp}[3] (cm^{-1})
$(1,1)\{0,0^0\}$	64.128	64.121(00)	$(2,3)\{0,1^1\}$	2614.034	2614.279(11)
$(1,0)\{0,0^0\}$	86.960	86.960(00)	$(2,2)\{0,1^1\}$	2723.708	2723.962(06)
$(2,2)\{0,0^0\}$	169.288	169.295(04)	$(2,1)\{0,1^1\}l$	2755.313	2755.565(04)
$(2,1)\{0,0^0\}$	237.335	237.356(05)	$(2,1)\{0,1^1\}u$	2790.086	2790.344(04)
$(3,3)\{0,0^0\}$	315.317	315.349(04)	$(2,0)\{0,1^1\}$	2812.504	2812.857(05)
$(3,2)\{0,0^0\}$	427.974	428.018(07)	$(3,3)\{0,1^1\}$	2876.566	2876.847(06)
$(3,1)\{0,0^0\}$	494.712	494.775(07)	$(3,2)\{0,1^1\}l$	2931.091	2931.366(05)
$(3,0)\{0,0^0\}$	516.823	516.873(07)	$(3,2)\{0,1^1\}u$	2992.151	2992.436(05)
$(0,1)\{0,1^1\}$	2521.183	2521.411(05)	$(3,1)\{0,1^1\}l$	3002.348	3002.905(05)
$(1,2)\{0,1^1\}$	2547.996	2548.164(11)	$(3,0)\{0,1^1\}$	3025.663	3025.951(08)
$(1,1)\{0,1^1\}$	2609.302	2609.541(05)	$(3,1)\{0,1^1\}u$	3063.181	3063.478(05)

[a]The quantum numbers labeling the energy levels, in the notation $(N^+, G)\{v_1, v_2^{l_2}\}(l|u)$ described in the text.
[b]Theoretically calculated results from this work.
[c]Experimentally determined energies from Ref. [1].

where θ_e and φ_e are spherical angles of the electron in the laboratory frame. The radial part of electronic wave function is not shown here since we apply the MQDT method for that degrees of freedom. Specifically, we want to construct the laboratory eigenchannel function $|i\rangle$ with a definite laboratory-frame total angular momentum N: $|i\rangle = |N^+, \nu^+\rangle^{(N,l,m,\Pi^+,g_I)}$. In the position representation, it takes the form as,

$$\sum_{\lambda} C^{N,m}_{N^+,m^+;l,\lambda} \Psi^{v^+ g_I \Pi^+}_{N^+ m^+} Y_{l\lambda}, \tag{3.10}$$

where $C^{N,m}_{N^+,m^+;l,\lambda}$ denotes the appropriate Clebsch-Gordan coefficient.

In the body-frame, the is specified state by the projection of theelectron angular momentum on the molecular Z-axis Λ, by the total angular momentum of the system N including the electron contribution l and the projection m of N on the laboratory z-axis. Applying the transformation between body-frame and lab-frame

$$Y_{l\lambda}(\theta_e, \varphi_e) = \sum_{\Lambda} \left[D^l_{\lambda\Lambda}(\alpha, \beta, \gamma) \right]^* Y_{l\Lambda}\left(\theta'_e, \varphi'_e\right), \tag{3.11}$$

the expansion of the product of two Wigner functions,

$$D^{N^+}_{m^+K^+} D^l_{\lambda\Lambda} = \sum_{N} D^N_{mK} C^{N,K}_{N^+,K^+;l.\Lambda} C^{N,m}_{N^+m^+;l,\lambda}, \tag{3.12}$$

we have the following equation,

$$\sum_{\lambda} C^{N,m}_{N^+,m^+;l,\lambda} \left[D^{N^+}_{m^+K^+} \right]^* Y_{l\lambda}(\theta_e, \varphi_e) = \sum_{\Lambda} (-)^{l-\Lambda} C^{N^+,K^+}_{l,-\Lambda;N,K} \left[D^N_{mK} \right]^* Y_{l\Lambda}\left(\theta'_e, \varphi'_e\right), \tag{3.13}$$

with some manipulation of algebra, where θ'_e and φ'_e are the spherical angles of the electron in the body-frame. Using Eq. (3.13), we derive the transformation between the body-frame and laboratory-frame states as,

$$\langle \alpha \, | i \rangle = \langle R, \Omega; \Lambda \left| N^+, \nu^+ \right\rangle^{(N,l,\Pi^+,g_I)} = \tilde{\Psi}^{N m g_I \Pi^+}_{N^+ v^+ \Lambda}, \tag{3.14}$$

where $\tilde{\Psi}^{N m g_I \Pi^+}_{N^+ v^+ \Lambda}$ is defined as,

$$\tilde{\Psi}^{N m g_I \Pi^+}_{N^+ v^+ \Lambda} = \sum_{n\nu} c^{(v^+)}_{n\nu} \pi_i(R) \sum_{j m_2 K^+} a^{(v)}_{j m_2 K^+}(R_n) \tilde{\Phi}^{N m g_I}_{j m_2 N^+ K^+ \Lambda}. \tag{3.15}$$

The explicit form of $\tilde{\Phi}^{Nmg_I}_{jm_2N^+K^+\Lambda}$ is given in Appendix C. The rovibrational frame transformation can be accomplished as follows:

$$K^{\left(Nmg_I\Pi^+\right)}_{N^+v^+;N^{+\prime}v^{+\prime}} = \sum_{\Lambda,\Lambda'} \int d\mathcal{Q} d\Omega_E \tilde{\Psi}^{Nm\Pi^+g_I*}_{N^+v^+\Lambda} K_{\Lambda\Lambda'}\left(\mathcal{Q}\right) \tilde{\Psi}^{Nm\Pi^+g_I}_{N^{+\prime}v^{+\prime}\Lambda'}, \tag{3.16}$$

where Ω_E denotes the Euler angles, and $\mathcal{Q}$ contains the three vibrational degrees of freedom.

3.3 p-wave energy levels of H_3

The body-frame reaction matrix for a p-wave electron is described by the short-range interaction extracted from an **ab initio** calculation [80]. In practice, the quantum defects are smoother than the reaction matrix elements because the latter can have poles. Hence in this work, we extract the body-frame quantum defects $\mu\left(\mathcal{Q}\right)$ from the **ab initio** energy surface directly. After replacing $K_{\Lambda\Lambda'}\left(\mathcal{Q}\right)$ by $\mu_{\Lambda\Lambda'}\left(\mathcal{Q}\right)$ in Eq.(3.16), we perform a rovibrational transformation to get the laboratory-frame quantum-defect matrix. Finally, we get the laboratory K matrix by using the eigenvalues μ_e from the laboratory-frame quantum-defect matrix,

$$K = U \tan\left(\pi\mu_e\right) U^T, \tag{3.17}$$

where U denotes the unitary transformation that diagonalizes the laboratory-frame quantum-defect matrix.

3.3.1 Body-frame quantum defects for p-waves

Because of Jahn-Teller effects, the body-frame quantum-defect matrix is generally not diagonal in the electronic projections Λ, Λ'. Similar to the body-frame K matrix proposed by Staib and Domcke [81], it has the form

$$\mu\left(\mathcal{Q}\right) = \begin{bmatrix} \mu_{00}\left(\mathcal{Q}\right) & 0 & 0 \\ 0 & \mu_{11}\left(\mathcal{Q}\right) & \mu_{1-1}\left(\mathcal{Q}\right) \\ 0 & \mu_{-11}\left(\mathcal{Q}\right) & \mu_{-1-1}\left(\mathcal{Q}\right) \end{bmatrix}. \tag{3.18}$$

We express each matrix element by using the vibrational symmetry coordinates $\mathcal{Q} = (Q_1, Q_x, Q_y)$ as

$$\begin{aligned} Q_1 &= f\frac{1}{\sqrt{3}}\left(\Delta r_1 + \Delta r_2 + \Delta r_3\right), && (3.19)\\ Q_x &= f\frac{1}{\sqrt{3}}\left(2\Delta r_3 - \Delta r_2 - \Delta r_1\right), && (3.20)\\ Q_y &= f\left(\Delta r_1 - \Delta r_2\right). && (3.21)\\ & && (3.22) \end{aligned}$$

where $f = 2.639\ 255\ \text{bohr}^{-1}$ is a constant and Δr_i describe displacements of the nuclei from the equilibrium geometry at which $r_{12} = r_{23} = r_{31} = r_{equi} = 1.6504\ a.u.$. For example, $\Delta r_1 = r_{23} - r_{\text{equi}}$. (Q_x, Q_y) can be alternatively described by another pair of coordinates (ρ, ϕ) as $Q_x = \rho\cos\phi$ and $Q_y = \rho\sin\phi$. Q_1 describes the symmetric stretch of the molecule, while (Q_x, Q_y) or (ρ, ϕ) describe bends and the asymmetric stretch. These coordinates are very useful here for our Taylor expansion of the body-frame quantum defects around an equilibrium position. We use the following forms,

$$\mu_{00}\left(\mathcal{Q}\right) = \mu_{00}\left(\mathcal{Q} = 0\right) + a_1 Q_1 + a_2 Q_1^2 + a_3 Q_1^3 + a_4\rho^2, \tag{3.23}$$

$$\begin{aligned} \mu_{11}\left(\mathcal{Q}\right) &= \mu_{-1-1}\left(\mathcal{Q}\right) && (3.24)\\ &= \mu_{11}\left(\mathcal{Q} = 0\right) + b_1 Q_1 + b_2 Q_1^2 + b_3 Q_1^3 + \delta\rho^2, \end{aligned}$$

and

$$\mu_{1-1}\left(\mathcal{Q}\right) = \mu_{-11}\left(\mathcal{Q}\right) = \lambda\rho. \tag{3.25}$$

The form of our off-diagonal matrix elements $\mu_{1-1}\left(\mathcal{Q}\right)$ and $\mu_{-11}\left(\mathcal{Q}\right)$ differs from the usual adopted form in Ref. [31] by a phase factor $\exp\left(\pm i\phi\right)$. This different phase convention is due to the fact that the usual adopted form was derived in a body frame that is rotated from our body frame by $\phi/2$. We develop the detailed proof in Appendix D. The effective quantum numbers are calculated by diagonalizing the quantum defect matrix. This calculation gives,

$$\nu_{n,\pi_{1,2}}\left(\mathcal{Q}\right) = n - \left[\mu_{11}\left(\mathcal{Q}\right) \pm \left|\mu_{1-1}\left(\mathcal{Q}\right)\right|\right], \tag{3.26}$$

an expression that can be used to fit the effective quantum numbers calculated **ab-initio** in Ref. [80].

3.3.2 $3p_1$ energy levels of H_3

We calculate the $3p_1$ energy levels of H_3 and compare them with empirical fits from Ref. [69]. Quantum defect parameters in Eqs.(3.23–3.25) are extracted from the **ab-initio** calculation in Ref. [80]. To fit the experiment results, we shift the quantum defects at equilibrium positions $\mu_{00}(\mathcal{Q}=0)=0.0683$ and $\mu_{11}(\mathcal{Q}=0)=0.4069$ by a small amount, 0.0043 and 0.0021 correspondingly.

In Ref. [69], Vervloet and Watson studied the H_3 emmision lines of $(3s, 3p_0, 3d) \rightarrow 2p_0$ bands and $(3s, 3p_0, 3d) \rightarrow 3p_0$ bands. They then fitted the lines with effective Hamiltonians of the following form,

$$\begin{aligned} & BN(N+1)+(C-B)K^2 \\ & -D_N N^2(N+1)^2 \\ & -D_{NK}N(N+1)K^2 \\ & -D_K K^4+\ldots \end{aligned} \tag{3.27}$$

where the explicit expressions can be found in Ref. [2, 3, 4, 5] and Ref. [69]. Table 3.2 compares our MQDT result with the experimental energy levels calculated from the fitted effective Hamiltonians. The labels N, g, U are fitting parameters, where N is also the total angular momentum of H_3, and g is related to the quantum number G by $G=|g|$. Evidently our calculations are in good agreement with the fitted and recalculated experimental results, with differences of around a few cm^{-1}.

3.4 Higher angular-momentum states

For higher electronic angular-momentum states with $l > 1$, the orbits are nonpenetrating and the short-range interaction is negligible. The long-range multipole potential model employing perturbation theory has successfully described the high orbital angular Rydberg states of H_2 [82, 83, 84]. In this work, we include the perturbations and interactions between levels of different n

Table 3.2: A comparison between several of our calculated $3p_1$ H_3 energy levels with empirically fitted experimental energy levels [2, 3, 4, 5].

Label[1] N, g, U	E_{cal}[2] (cm^{-1})	E_{fit} [3] (cm^{-1})	Differences [4] (cm^{-1})
$0, 1, 1$	12967.8	12966.863	0.9
$1, 0, 1$	12999.1	12998.196	0.9
$1, 1, 1$	13052.3	13050.966	1.3
$1, 2, 1$	13066.9	13068.700	-1.8
$2, 0, -1$	13139.9	13138.608	1.3
$2, 1, -1$	13056.1	13056.588	-0.5
$2, 1, 1$	13221.1	13219.125	1.9
$2, 2, 1$	13234.3	13235.522	-1.2
$2, -3, 1$	13203.8	13212.055	-8.3
$3, 0, 1$	13450.7	13446.072	4.6
$3, 1, -1$	13300.6	13300.119	0.5
$3, 2, -1$	13160.5	13165.030	-4.5
$3, 2, 1$	13485.4	13483.545	1.9
$3, 3, 1$	13453.2	13460.934	-7.7

[a]The label denotes the values of N, G, U adopted in Ref. [69] to fit the experimental energy levels.
[b]Theoretical results calculated in this study.
[c]Empirical fits for experimental energies determined in Ref. [69].
[d]Differences theory - experiment.

(principle quantum number) and l (angular-momentum quantum number) in a systematic fashion by incorporating the formalism of MQDT [85]. We use this long-range model to calculate the Rydberg states of H_3 with $l \geq 2$.

For a Rydberg electron with high orbital angular momentum ($l \geq 2$ in the case of H_3^+), the effects of core penetration are negligible. Hence, the interaction between the Rydberg electron and the ion core can be approximately described by two effects. First, the interaction potential between the Rydberg electron and the molecular ion is expanded into a multipole series, where the quadrupole moment of the H_3^+ core is the leading anisotropic term. Second, the induced dipole moment of the ion core interacts with the Rydberg electron by a potential characterized by the polarizability of the H_3^+ core. All higher angular momenta and higher-order polarizabilities are neglected here, as well as the anisotropic portion of the polarizability interaction.

In this approximation, the Hamiltonian is given in atomic units by

$$H = -\frac{1}{2}\nabla^2 - \frac{1}{r} + V_{eff} + H_{core}, \tag{3.28}$$

where H_{core} is the rovibrational energy of the H_3^+ core. V_{eff} includes quadrupole and polarizability interactions:

$$V_{eff} = V_{quad} + V_{pol} = -\frac{Q_2}{r^3} P_2\left(\cos\theta_e'\right) - \frac{\alpha}{2r^4} - \frac{\gamma}{3r^4} P_2\left(\cos\theta_e'\right). \tag{3.29}$$

where Q_2, α, and γ are respectively the quadrupole moment, isotropic polarizability and the cylindrically-symmetric anisotropic polarizability. Other components of the quadrupole moment tensor vanish for the undistorted equilateral triangle configuration. For the vibrational ground state, Q_2, α, and γ are taken from table III of Ref. [86, 87]. The polarizability and quadrupole interactions are much smaller than the Coulomb interaction and hence will be treated in perturbation theory. We also find that the quantum defect is small (of the order of 0.01), and the coupling between vibrational ground states of H_3^+ to excited vibrational states are negligible. Hence, in the rovibrational transformation, we only include the vibrational ground state. The body-frame reaction matrix thus can be written as

$$K_{\Lambda\Lambda'} \approx -\pi \int dr\, f_{nl}(r) \left\langle Y_{l\Lambda} \right| V_{eff} \left| Y_{l\Lambda'} \right\rangle f_{nl}(r), \tag{3.30}$$

Table 3.3: Comparison between several of our calculated $3d$ energy levels of H_3 with experimentally-determined energy levels[2, 3, 4, 5].

Label[1] N^+, K^+, N	E_{cal}[2] (cm^{-1})	E_{fit} [3] (cm^{-1})	Differences[4] (cm^{-1})
$2,1,0$	17399.14	17415.86	-15.89
$2,2,0$	17058.41	17039.61	18.80
$1,0,1$	17284.81	17296.57	-11.76
$3,0,1$	17742.32	17741.29	1.03
$1,1,1$	17005.99	16991.72	14.28
$2,1,1$	17403.89	17412.83	-8.94
$3,1,1$	17698.40	17700.43	-2.02
$2,2,1$	17107.24	17094.12	13.13
$3,2,1$	17540.96	17557.32	-16.35
$3,3,1$	17204.46	17188.48	15.98
$1,0,2$	17011.36	17001.08	10.27
$3,0,2$	17643.36	17655.58	-12.21

[a]The label denotes the quantum numbers N^+, K^+, N.
[b]Theoretical results calculated in this work.
[c]Empirical fits to the experimental energies determined in Ref. [69].
[d]Differences between theoretical and experimental results.

where f_{nl} is the regular Coulomb function with $l = 1$ as the angular momentum quantum number and n as the principal quantum number. As the quantum defect for d-wave electrons are small, we can use integers for n in calculating the radial functions. Here, r is the electronic radial coordinate. Again, we perform a rovibrational transformation (with only the vibrational ground states) to obtain the laboratory-frame K matrix and finally, calculate the energy levels using the standard determinantal equation of MQDT.

Table 3.3 compares our theoretical calculations with the experimentally-determined 3d energy levels [69]. The agreement somewhat poorer than the p-wave case.

3.5 Recombination-pumped triatomic hydrogen infrared lasers

The nice comparisons between our calculated low-lying Rydberg energy levels and the experiment results give us confidence of our method, and encourage us to apply it for higher Rydberg states. In a recent experiment, mid-infrared laser lines observed in hydrogen/rare gas discharges are assigned to three-body recombination processes involving an electron, a rare gas (He or Ne) atom, and the triatomic hydrogen ion (H_3^+). Calculations of radiative transitions between higher Rydberg states of neutral (H_3) Rydberg states support this interpretation, and link it to recent results for hydrogenic/rare gas afterglow plasmas. A mechanism for the population inversion is also proposed in this section.

In this experiment [44], laser emission lines were produced from an ultrahigh finesse optical supercavity containing a supersonically expanding plasma in the spectral range of 930 – 4370 cm^{-1}, with the majority occurring near 7 μm (1430 cm^{-1}). The supersonic slit expansion generates a weakly ionized plasma with neutral gas density expanding as the reciprocal of distance from the slit nozzle, such that the pressure in the region of observation is in the range of 0.1 to 10 Torr (densities of 10^{15} – 10^{17} cm^{-3}). Fifty-seven laser transitions were observed in both H_2 – He and H_2 – Ne gas mixtures. Twenty-nine laser transitions in H_2 – He were also observed in H_2O – He or H_2O – Ne discharges, which is not surprising, as these plasmas are known to produce significant amounts of hydrogen [88].

It was found that laser intensity was highly dependent on partial pressure of H_2 in the expanding gas mixture, maximizing when the mixing ratio was $< 1\%$. No lasing was observed when pure H_2 gas was used for the expansion. This most probably reflects the conversion of the dominant H_3^+ ion to the H_5^+ complex at higher hydrogen concentrations, as characterized by Glosik et al [89].

To test whether contaminants such as O_2 or H_2O could be involved in the lasing observed in the H_2/He plasma, three experiments were performed. First, O_2 was carefully added to the gas line through a needle valve to determine how the presence of O_2 affected laser intensity, revealing that it decreased significantly when O_2 was added to the gas mixture. Second, no lasing was observed when the H_2 cylinder was closed, indicating that the lasing species was indeed generated from the cylinder gas. Third, in case the cylinder was itself contaminated with traces of condensible, the gas was flowed through a long ($\sim$8 ft) liquid nitrogen trap. No difference was observed in the lasing intensity with or without the liquid N_2 trap, indicating that the lasing species originates from species produced from pure H_2 and He or Ne.

We applied the long-range multipole potentialmodel discussed in the section 3.4 to the d-wave Rydberg states of H_3. While the d-wave Rydberg states of H_3 were computed with this long-range model, the p-wave Rydberg states are computed separately using the method discussed in section 3.3, since they are mainly dominated by the short-range interaction between the outer electron and the ion core [90, 91]. These p-wave Rydberg states either autoionize or predissociate much more rapidly than do the d-wave Rydberg states because of their stronger Jahn-Teller couplings, or through ordinary l-uncoupling, which causes rotational autoionization and does not rely on the Jahn-Teller effect. The corresponding d-p H_3 dipole transitions thereby satisfy one of the golden rules of astrophysical lasers, viz. the lifetime of the lower level of a lasing transition should be much shorter than the lifetime of the upper level independent of the excitation mechanism;[] hence, a population inversion can be created by the recombination process, and mid-IR lasing can occur under proper conditions. Comparison of the measured lasing lines with the theoretical nd to np lines suggests that metastable H_3 created in the expanding plasma is indeed a likely candidate for

the carrier of these lasing transitions. Note, however, that the candidate lasing lines calculated in this study are primarily of the type 4d–4p, whereas the ternary recombination mechanism is believed to predominantly produce much higher Rydberg levels with principal quantum numbers in the range $n \approx 40 \sim 60$ or even higher. This view of the process therefore requires a cascade, i.e., a decay of these highly excited nf levels to the 4d states, which then have a population inversion and are able to lase while decaying to the 4p levels of H_3.

Because there are no laboratory measurements of the 4d – 4p transitions that appear to be the most likely candidates for the lasing lines reported here, the theoretical model has been tested (in section 2.3 and 2.4) against the experimental 3d to 3p transitions of H_3 that were measured by Herzberg, showing good agreement (the rms error for 14 tabulated transitions is below 13 cm^{-1}) [92]. A comparison between the current experiment and our theoretical calculation is shown in Fig. 3.2 and table 3.4. However, there are a few residual experimental lines having no corresponding theoretical transition. These may correspond to Rydberg levels of the ion core with other $\{N^+, K^+\}$, although we do not have specific candidates in mind at this point.

The conditions obtaining in the pulsed supersonic slit jet plasma used to generate the observed IR laser action described here are similar to those employed by Glosik et al. in their studies of H_3^+ recombination in flowing afterglow plasmas [89, 93]. The total gas pressure drops from the 1 – 2 atmosphere nozzle backing pressure as the reciprocal of distance from the 300 – 400 μm wide exit slit, yielding neutral gas densities of 10^{14} – 10^{17} cm^{-3} in the regions probed. Typical fractional ionizations in such plasmas are $\sim 10^{-5}$. Studies of the H_3O^+ ion in similar pulsed slit jet discharges yielded number densities near 10^{10} cm^{-3} and a rotational temperature near 110 K for this ion. Glosik et al. measured the temperature-dependent recombination rate of H_3^+ with electrons in recombination-limited $He/Ar/H_2$ plasmas at He densities of $0.5 - 6 \times 10^{17}$ cm^{-3} and temperatures of 77 – 300 K. They identified three different behaviors of the measured recombination coefficient with respect to hydrogen content. For $[H_2] < 10^{12}$ cm^{-3} (or $<10^{-5}$ of the total gas density), it increases with increasing H_2 density and the spin states of H_3^+ are not equilibrated. For $10^{12} < [H_2] < 5 \times 10^{13}$ cm^{-3}, the rate is independent of H_2 density and the ion is in thermal equilibrium.

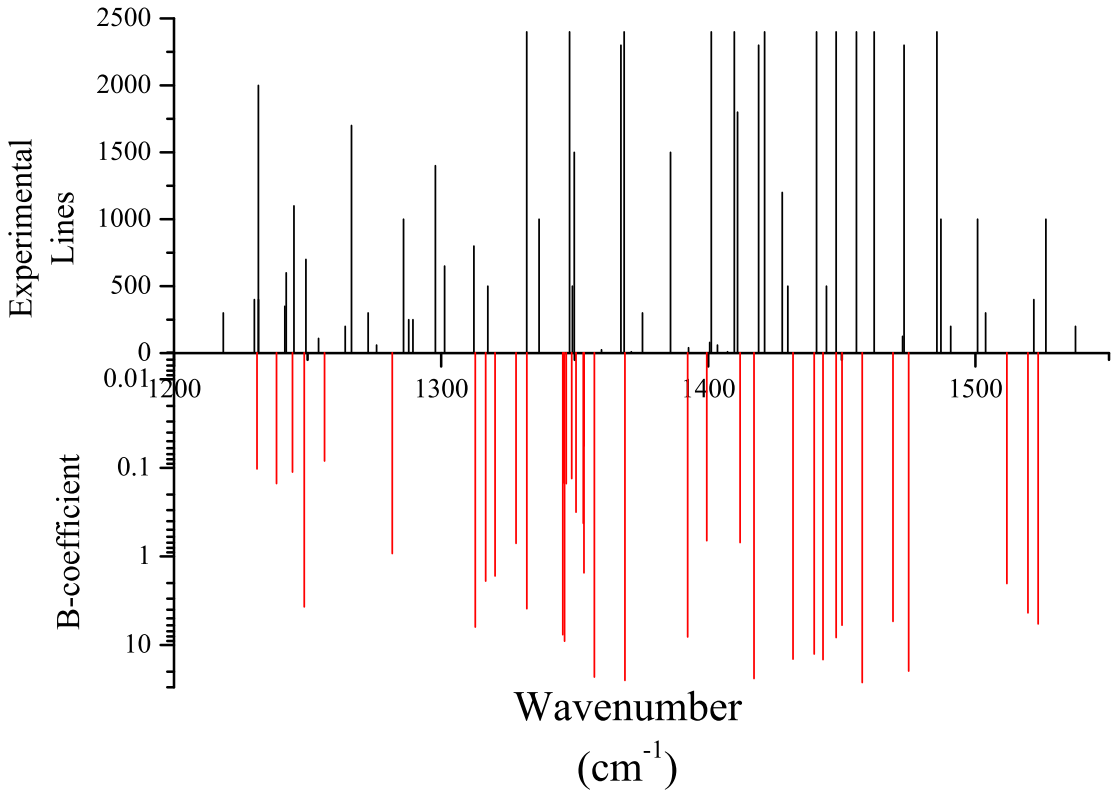

Figure 3.2: Comparison of experimental results with calculated $nd \rightarrow n'p$ transitions of H_3. The experimental laser strength is in arbitrary units with linear scale, while the present theoretical B-coefficients are in the units of 10^{22} (m/Js^2) on a logarithmic scale. The calculated line positions have a precision of about 13 cm^{-1}

Table 3.4: Possible assignment of laser lines observed in this work. We calculate the theory lines by using models described in this chapter. The experiment lines are chosen from the H_2O – He laser lines which are also observed in H_2O – He or H_2O – Ne experiments.

Initial[a] N^+,K^+,N,nd	Final[b] K^+,N,$n'p_\lambda$	Theory lines(cm^{-1})	H_2O-He lines(cm^{-1})	Difference[c] (cm^{-1})	B/10^{21} (m/Js^2)	H_2O – He intensity
3,1,3,5d	1,2,5pπ_-	1053.41	1054.63	1.22	2.26	130
3,1,1,5d	1,2,5pπ_-	1084.27	1082	-2.27	4.24	100
		1218.47				300
1,1,1,4d	1,2,4pπ_+	1231.06	1231.59	0.53	0.10	2000
1,1,3,4d	1,2,4pπ_+	1248.76	1249.37	0.61	3.71	700
1,0,1,7d	0,1,6pπ	1256.36	1254.13	-2.23	0.08	110
		1266.44				1700
3,1,3,6d	1,3,5pσ	1293.94	1297.83	3.89	961.95	1400
3,1,2,6d	1,3,5pσ	1302.57	1301.31	-1.26	0.44	650
1,0,2,4d	0,2,4pπ	1312.78	1312.26	-0.52	6.28	800
2,1,3,6d	1,2,5pσ	1316.66	1317.49	0.83	16.11	500
1,1,1,6d	1,1,5pσ	1332.07	1332.05	-0.02	3.90	2400
2,2,3,6d	2,2,5pσ	1337.16	1336.66	-0.50	8.22	1000
2,1,3,7d	1,2,6pπ_-	1346.83	1348.07	1.24	20.04	2400
2,1,1,7d	1,1,6pπ	1350.49	1349.14	-1.35	2.92	500
2,2,2,4d	2,2,4pπ	1350.74	1349.85	-0.89	8.40	1500
1,0,3,4d	0,2,4pπ	1368.81	1367.29	-1.52	25.12	2300
3,1,4,7d	1,3,6pπ_-	1370.69	1368.51	-2.18	2.34	2400
3,1,3,7d	1,3,6pπ_-	1371.75	1371.18	-0.57	5.78	10
3,1,2,7d	1,3,6pπ_-	1377.14	1375.35	-1.79	0.08	300
2,2,3,4d	2,2,4pπ	1387.33	1385.87	-1.46	9.59	1500
1,1,1,4d	1,1,4pπ	1392.30	1392.6	0.30	8.12	40
1,1,1,4d	1,2,4pπ_-	1399.42	1400.55	1.13	0.66	80
1,1,1,4d	1,1,4pπ	1392.30	1401.13	8.83	8.12	2400
1,1,1,4d	1,2,4pπ_-	1399.42	1403.42	4.00	0.66	60
1,0,1,4d	0,2,4pπ	1411.91	1407.2	-4.71	0.70	10
		1409.74				2400
1,1,3,4d	1,2,4pπ	1417.11	1418.84	1.73	23.93	2300
		1421.09				2400
2,1,2,4d	1,2,4pπ_+	1439.63	1440.54	0.91	19.17	2400
1,1,2,4d	1,1,4pπ	1442.93	1444.22	1.29	14.62	500
2,2,0,4d	2,1,4pπ	1445.25	1447.85	2.60	35.43	2400
1,0,2,4d	0,1,4pπ	1457.61	1455.45	-2.16	26.57	2400
2,1,1,4d	1,2,4pπ_+	1469.15	1462.08	-7.07	5.42	2400
2,2,1,4d	2,1,4pπ	1471.77	1472.73	0.96	26.57	125
1,1,1,4d	1,0,4pπ	1475.02	1473.27	-1.75	19.68	2300

[a]The initial states, labeled by the quantum number N^+, K^+, N, nd.
[b]The final states, labeled by the quantum number $K^+, N, n'p_\lambda$. An additional + or − denotes the possible Jahn–Teller splitting of two p states: +(−) denotes the higher (lower) energy level.
[c]The difference between the theory lines and H_2O – He laser lines.

For $[H_2] > 10^{13}$ cm^{-3}, it again increases with increasing hydrogen density due to the conversion of H_3^+ to the H_5^+ complex [89], which recombines very rapidly, but which apparently does not produce observable laser action in our experiments. Analysis of these data indicated that three-body recombination processes dominated over two-body processes at pressures of a few Torr (10^{16} – 10^{17} cm^{-3}) and temperatures near 300 K, and that this ternary rate maximizes at temperatures of 130 – 170 K. Hence, we can reasonably conclude that the three-body recombination processes also dominate the ion loss in our recombination-limited supersonic plasmas. Glosik et al. [89, 93] show that such processes are ca. 100 times faster than that previously described by Bates and Khare [94], and they present a theoretical model for them. In this model, the resonant H_3^+ + e. complex [i.e., the highly excited ($n \approx$40 – 60) H_3 Rydberg molecule], which efficiently decays back into the ion and electron via rotational autoionization, collides with a He atom during its lifetime, changing the l-state of the complex to higher, longer-lived values. In particular, the l = 1(p) electronic states are strongly coupled to the ion core and autoionize rapidly, whereas $l \geq 2$(d) states are much more longlived. These l-changing collisions of the H_3 molecule thus produce the population inversion required for the laser action observed in our experiments.

Glosik et al. have shown that in the low H_3^+ + e. collision energy regime, rotational excitation of the vibrational ground state of the ion core with $\{N^+, K^+\} = \{1, 1\}$ produces long-lived Rydberg states most efficiently. Hence, the most likely product immediately following collision would be a highly excited ($n \approx 40$ – 60) p-wave Rydberg electron attached to a $\{N^+, K^+\} = \{2, 1\}$ ion core. A subsequent collision of the H_3 neutral molecule with a rare gas atom changes the Rydberg electron angular momentum to a longer-lived, higher value, and/or the collision of the He atom with the H_3^+ core might deexcite the ion core, which would close the rotational autoionization decay route. Radiative cascade can then populate the 4d levels that are the primary lasing candidates in transitions to the 4p states. Hence, in the theoretical calculation, we include the transitions from a 4d electron attached to $\{2, 1\}$, $\{1, 1\}$, and $\{1, 0\}$ cores to the n→p energy levels of H_3. Other transitions of the type nf→nd and ng→nf of H_3 have also been checked, but they do not appear to be connected with the present experimental results.

3.6 Summary

In this chapter, we have calculated the Rydberg energy levels of H_3 molecules. Using an accurate **ab-initio** quantum-defect surface and **ab-initio** core energies of H_3^+, our theoretical results for the p-wave Rydberg states from the present MQDT calculations are in good agreement with experimental results from J. K. G. Watson [69]. We also study higher-momentum states by a using a long-range multipole potential model in conjunction with MQDT, and find encouraging agreement with experimental results from Ref. [69]. Finally, applying such models for higher Rydberg states gives supportive explanation of the mid-infrared laser lines in a recent experiment [44].

Chapter 4

Numerical study of three-body recombination

This chapter focus on another type of three-body systems: recombination of three particles at ultracold temperature. Here, three-body recombination processes are treated numerically for a system of three identical bosons. The two-body model potentials utilized support many bound states, a major leap in complexity that produces an intricate structure of sharp nonadiabatic avoided crossings in the three-body hyperradial adiabatic potentials at short distances. This model thus displays the usual difficulties of more realistic systems. To overcome the numerical challenges associated with sharp avoided crossings, the slow variable discretization (SVD) approach is adopted in the region of small hyperradii. At larger hyperradii, where the adiabatic potentials and couplings are smooth, the traditional adiabatic method suffices. Despite the high degree of complexity, recombination into deeply bound states behaves regularly due to the dominance of one decay pathway, resulting from the strong coupling between different recombination channels. Moreover, the usual Wigner threshold law must be modified for excited incident recombination channels.

Note that the material in this chapter has been published in Ref. [95].

4.1 Introduction

Three-body recombination has attracted much theoretical and experimental research interest in recent years. Recombination is the process in which three free particles collide to form a two-body state and a free particle, with the released kinetic energy being distributed between the final collisional partners. Such reactions are common and important in chemical reactions and in atomic,

molecular, and nuclear physics. In ultracold degenerate Fermi gases [96, 97, 98] recombination has been used as a process to form weakly bound diatomic states, crucial for the experimental realization of the BEC-BCS crossover physics. In fact, it was shown in Ref. [99] that the use of recombination as an efficient way to produce weakly bound diatomic molecules can be extended to systems other than fermionic gases. For colliding BECs at precisely-tuned relative velocity, the formation of molecules via 3-body recombination can also be used to form molecules efficiently owing to a double Bose enhancement [100]. Recombination processes normally release a high amount of kinetic energy, producing atomic losses that often limit the lifetimes of Bose-Einstein condensates (BEC) [101]. Moreover, three-body recombination has been recognized as one of the most important scattering observables in which features related to the universal Efimov physics can be manifested [102, 35, 103, 104, 32, 105]. Near a two-body Fano-Feshbach resonance, i.e., when the s-wave scattering length a is much larger than the range r_0 of the interactions, Efimov states can occur, causing interference and resonant effects in recombination. The experimental observation of these features in recombination has been recently used as evidence of Efimov physics in ultracold quantum gases [106].

From the theoretical viewpoint, quantitative calculations of recombination for the typical alkali atoms used in experiments in ultracold gases are limited by the large number of diatomic states existing in such systems. Most of the available calculations for recombination for realistic systems have been confined to model systems possessing just a few bound states and/or systems with small scattering lengths, and even these are challenging calculations [107, 108, 47, 109]. As a result, recombination calculations relevant for ultracold gases can only be made in the universal regime $|a| \gg r_0$, by using simple potential models (with a few-bound states) or else by simply modeling the decay into all deeply bound molecular states through a single inelastic parameter [104]. However, in ultracold gases experiments the condition of universality is typically **not** satisfied, making it desirable to perform more realistic calculations involving more sophisticated two-body models with, eventually, a larger number of deeply bound states. This paper develops a methodology within the hyperspherical adiabatic representation that permits the treatment of systems with many bound

states.

The present study still utilizes two-body potentials models that are, however, designed to support many bound states, and therefore mimic three-body collisions for more realistic scenarios. In the hyperspherical representation, the existence of many bound states leads to a complex set of sharp nonadiabatic avoided crossings in the hyperspherical potential curves at short distances. The large number of sharp avoided crossings creates numerical difficulties for the traditional adiabatic representation as formulated with d/dR couplings [110]. To overcome these numerical difficulties, one solution is to use the slow variable discretiazation (SVD) method proposed by Tolstikhin **et al** [75]. The SVD method has been successfully applied to three-body bound-state calculations [110, 63] and three-body collisions for the $H + Ne_2$ system [111, 112]. Those calculations, however, did not require numerical solution of the hyperradial equation [see Eq. (2.17) below] out to large distances. To study ultracold collision processes such as recombination in the large scattering length limit, it is crucial to solve the hyperradial equation out to very large distances. Since application of SVD over the entire space is demanding in terms of memory and cpu-time, it is in fact much more efficient to separate the domain of hyperradii into two regimes. At short distances, where many avoided crossings appear, the SVD method is applied, while at large distances, where the adiabatic potential curves are smooth, the traditional adiabatic method [54] is utilized.

This two-pronged strategy enables efficient calculation of the three-body recombination rate at low collision energy, with extremely stable results for a two-body potential model supporting up to about 10 bound states. This numerical capability of calculating recombination with many bound states permits us to study the final state distribution of the recombination rate, K_3. One unexpectedly simple finding is that the branching ratio of recombination into a particular final (f) channel, defined as

$$r_3^{(f\leftarrow i)} = \frac{K_3^{(f\leftarrow i)}}{\sum_f K_3^{(f\leftarrow i)}} \tag{4.1}$$

is the **same** for different initial (i) three-body collision channels. In the above equation, $K_3^{(f\leftarrow i)}$ is the partial recombination from the initial three-body channel i to a particular final channel f.

The threshold laws for the partial recombination rates have also been considered, i.e., recombination processes occurring from excited three-body continua. These partial rates are observed to deviate from the usual Wigner threshold law. Specifically, the energy dependence of the partial recombination rates display a much weaker suppression than the usual Wigner analysis [113, 103] for excited continuum channels. These numerical results can be interpreted as the manifestation of a strong coupling between three-body continuum channels. This is further quantified through a perturbation series expansion of the scattering matrix that reveals the three-body recombination pathways at low collision energies.

This article is organized as follows. Section 4.2 discusses the numerical details in this study. Section 4.3 shows the numerical results for the three-body recombination rates , and Section 4.4 presents our analysis of the recombination pathways. Section 4.5 summarizes and concludes.

4.2 Adiabatic hyperspherical representation

The system studied here consists of three identical bosons with masses $m_1 = m_2 = m_3 = m$ with total angular momentum $J = 0$. The present study uses a two-body potential model in form of

$$v\left(r_{ij}\right) = D\mathrm{sech}^2\left(\frac{r_{ij}}{r_0}\right), \tag{4.2}$$

where the coefficient D is negative, and its magnitude is chosen to be large enough to support 8 to 10 two-body bound states (4 to 5 s-wave bound states). The total interaction potential can be approximated accurately by a pairwise sum of two-body interaction:

$$V\left(R,\theta,\varphi\right) = v\left(r_{12}\right) + v\left(r_{23}\right) + v\left(r_{31}\right). \tag{4.3}$$

The first correction to this expression, the Axilrod-Teller term [114], is included latter and found unimportant. Using the numerical basis discussed in Ref. [47], Eq. (2.12) is solved for the adiabatic potential and channel functions.

Figures 4.1 and 4.2 show the typical adiabatic potential curves for the parameter $m = 7.2963\times 10^3$ a.u., $D = -5.500 \times 10^{-5}$ a.u. and $r_0 = 15$ a.u. Figure 4.1 exhibits several sharp nonadiabatic

avoided crossings at short distances. Although in our representation sharp crossings are associated with vanishingly small transition probabilities, these avoided crossings can cause several numerical difficulties when solving for the hyperradial motion in the traditional adiabatic approach. As mentioned above, such difficulties are overcome by implementing the SVD method described in Ref. [75]. Figure 4.2 shows, however, that the adiabatic potentials at long distances are smooth and, therefore, are more suitable for traditional approaches. The R-matrix propagation method was discussed in subsection 4.2.4 and Appendix B. With this method, R-matrix at very large distance can be obtained. The scattering matrix $\underline{\mathcal{S}}$ is then given by Eq. (2.22).

The three-body recombination rate is therefore given by [47]

$$K_3^{(f\leftarrow i)} = \frac{192\pi^2\,(2J+1)}{\mu_{3b}k^4}\left|\mathcal{S}_{fi}\right|^2, \tag{4.4}$$

where $\mathcal{S}_{fi}$ is the appropriate S-matrix elements, J is the total angular momentum of the system, and $k = \sqrt{2\mu_{3b}E}$ gives the hyperradial wave numbers in the incident channels.

4.3 Three-body recombination rates

The present numerical study focuses on systems of three identical bosons with total angular momentum $J = 0$, with parameters adjusted to represent the ^{4}He system ($m_1 = m_2 = m_3 = 7.2963 \times 10^3$ a.u. and $r_0 = 15$ a.u., the same as in Fig. 4.1). The two-body potential depth D [see Eq. (4.2)] is adjusted to tune the scattering length a and explore both the positive- and negative-scattering length cases while supporting 8-10 bound states. The recombination rate near the unitary regime ($k\,|a| \approx 1$), is explored next for two sets of typical parameters: $D = -5.500 \times 10^{-5}$ a.u. for the positive-scattering length case, $a = 1020.36$ a.u.; $D = -5.467\times10^{-5}$ a.u. for negative-scattering length case, $a = -1096.07$ a.u. For both cases a is much larger than r_0 ($|a|/r_0 \approx 70$) and therefore such calculations are solidly within the universal regime [104, 103].

The black dashed lines in Figs. 4.1 and 4.2 denote the recombination channels, i.e., the final state channels of the recombination process. The effective hyperradial potentials $\widetilde{U}_\nu\,(R) \equiv$

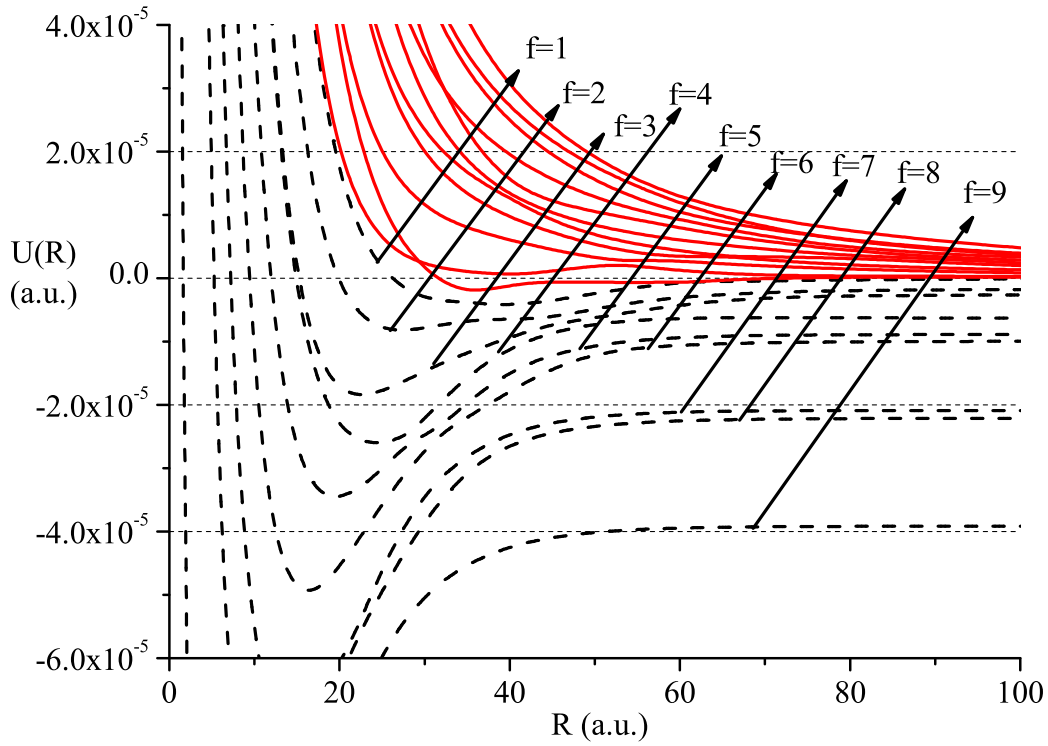

Figure 4.1: (Color online) Adiabatic potential curves $U(R)$ at short distances R. Red solid lines represent the three-body continuum channels, i.e., the initial channels for recombination processes, and black dashed lines represent the final recombination channels.

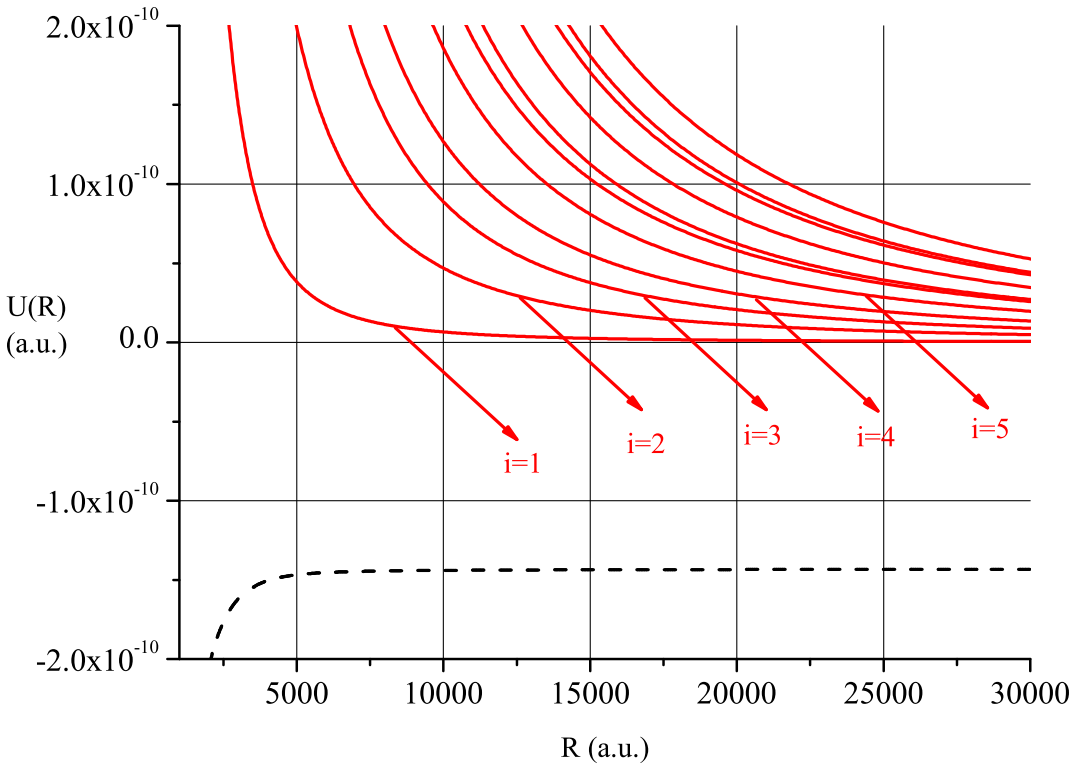

Figure 4.2: (Color online) Same as Fig. 4.1, but for the adiabatic potential curves $U(R)$ at large distances R. This figure contrasts with Fig. 4.1 in the characteristically smooth behavior at large distances.

$U_\nu(R) - Q_{\nu\nu}/(2\mu_{3b})$ for these channels have asymptotic behavior given by

$$\widetilde{U}_f(R) \overset{R\to\infty}{\approx} \frac{l_f(l_f+1)}{2\mu_{3b}R^2} + E_{2b}^{(f)}, \tag{4.5}$$

where $E_{2b}^{(f)}$ is the two-body bound state (dimer) energies, and l_f is the corresponding angular momentum of the third particle relative to the dimer. The subscript f labels these recombination channels in ascending order, i.e., from high-to-low two-body bound state energies. In Figs. 1 and 2, red solid lines denote the three-body break-up channels (or entrance channels) whose asymptotic is described by

$$\widetilde{U}_i(R) \overset{R\to\infty}{\approx} \frac{\lambda_i(\lambda_i+4)+15/4}{2\mu_{3b}R^2}, \tag{4.6}$$

where $\lambda_i(\lambda_i+4)$ is the eigenvalue of the grand angular momentum operator Λ^2 (here, $\lambda_i = 0, 4, 6, 8...$, where $\lambda_i = 2$ is absent for symmetry considerations). The subscript i labels three-body break-up channels in ascending order, i.e., from low-to-high eigenvalues λ_i.

As Ref. [113, 103] points out, the asymptotic form of $\widetilde{U}_i$ determines the Wigner threshold laws for recombination, i.e., the low energy behavior of the recombination rate. A simple extension of the results of Ref. [113, 103] yields the Wigner threshold laws for all three-body channels as

$$K_3^{(f\leftarrow i)} \propto E^{\lambda_i} \tag{4.7}$$

Our numerical results, however, show that Eq. (4.7) only holds for the lowest entrance channel ($i = 1$) while it fails to describe the threshold laws for higher incident channels ($i > 1$). This is apparent from Figs. 4.3 and 4.4, which show our numerical calculations for recombination with positive and negative values of the scattering lengths, respectively.

In fact, Figs. 4.3 and 4.4 illustrate that for the partial recombination rate from the lowest three-body incidence channel ($\lambda_1 = 0$), the threshold behavior does follow the Wigner threshold law prediction, $K_3^{(f\leftarrow 1)} \propto E^0$. However, for higher incident channels $\lambda_2 = 4$, $\lambda_3 = 6$, the threshold energy exponent is independent of λ_i and recombination rates are only proportional to E^1. Therefore the low-energy suppression for higher three-body break-up channels is much weaker than what Wigner's threshold law would predict (see Eq. (4.7)). Note that we have used different line-styles

to indicate the recombination rate for different incident channels, and use different color and thickness of lines for different final channels. The solid, dashed, dot, dash-dot and short dashed lines indicate recombination rate to different recombination channels: $f = 1, 2, 3, 4, 5$. The thick black lines, thinner red lines, and thinnest blue lines indicate recombination rates from different incident channels: $i = 1, 2, 3$.

Another important property that has emerged from our numerical calculations is that the branching ratio [Eq. (4.1)] for the three-body recombination rates into different final channels are the *same* for the few lowest initial channel in the low collision energy limit (see Figs. 4.5 and 4.6). For instance, for the three different initial channels shown in Fig. 4.5, a case with positive scattering length, the branching ratio into the highest bound state is about 0.35 for each of the three lowest incident channels throughout the energy range $E \lesssim 10\mu$K. Similar results are seen for the branching ratios at negative scattering lengths, as is documented by Fig. 4.6. Note, however, that the branching ratios for positive scattering lengths are not the same for $E > 10\mu$K (see Fig. 4.5) while they remain the same for negative scattering length (see Fig. 4.6). This is a result of destructive interference effects that reduces the recombination probability for the most weakly bound recombination channel for positive scattering length, and it is related to the universal Efimov physics [104, 103]. In fact, such interference effect is only significant in the shallowest final channel. Hence, if the $f = 1$ channel is excluded from the summation in the denominator on the right hand side of Eq. (4.1), the calculated branching ratio between the deep bound states should be the same for the whole energy range considered, as the inset of Fig. 4.5 shows.

Both the branching ratio properties uncovered in the present numerical exploration and the deviations from the recombination Wigner threshold laws can be understood using the analytical model developed in the next section. As we will see, these results are driven simply by the strong long-range coupling between the three-body incident channels; this analysis gives further insight into the pathways controlling three-body recombination.

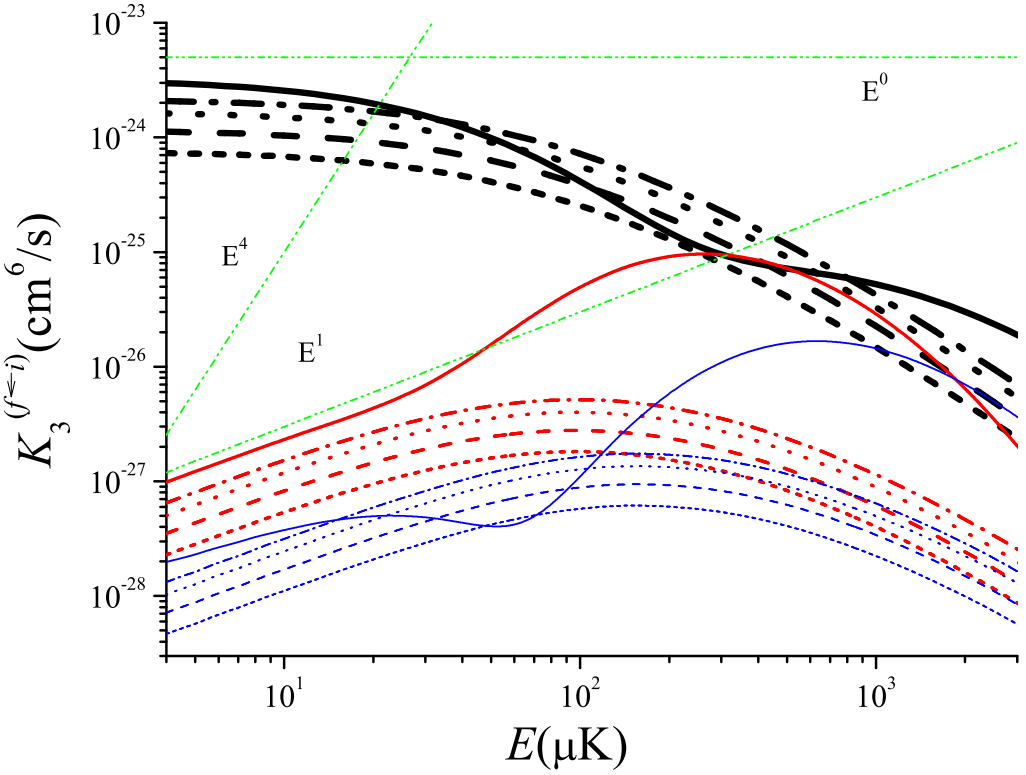

Figure 4.3: (Color online) Partial recombination rate $K_3^{(f\leftarrow i)}$ as a function of the collision energy E for the positive-scattering length case. The solid, dashed, dot, dash-dot and short dashed lines indicate partial recombination rates to different recombination channels: $f = 1, 2, 3, 4, 5$, respectively. The thick black lines, thinner red lines and thinnest blue lines indicate recombination rates from different incident channels: $i = 1, 2, 3$. The three green dash-dot-dot lines are proportional to E^0, E^1 and E^4 as indicated in the figure.

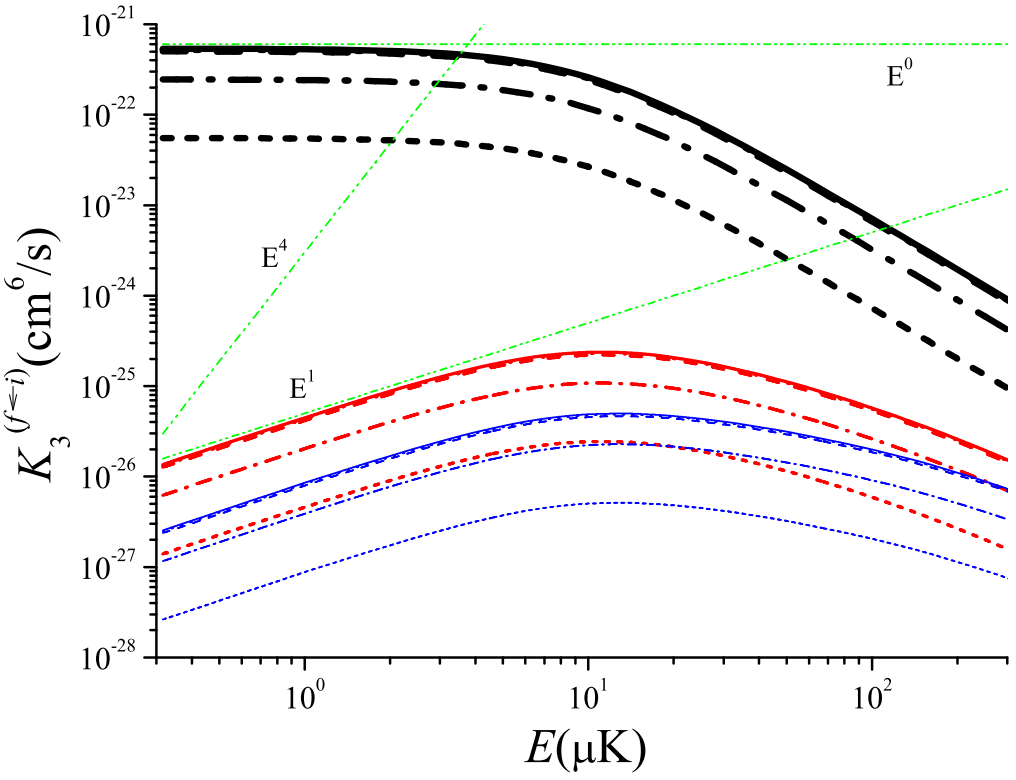

Figure 4.4: (Color online) Same as Fig. 4.3 but for the negative scattering length case.

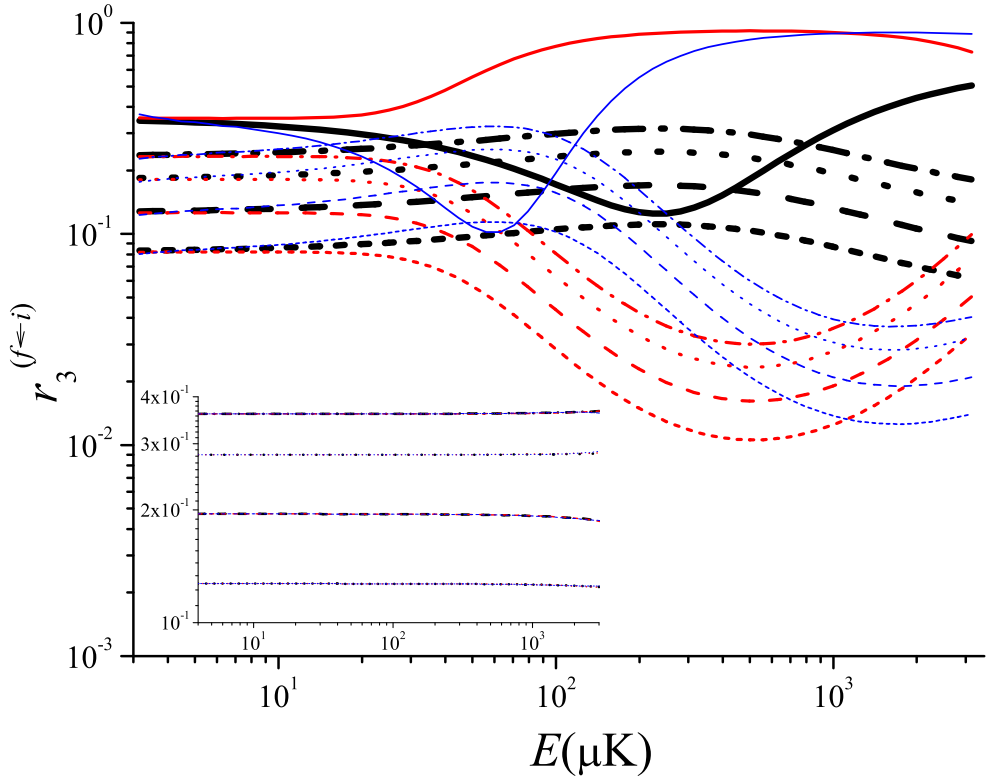

Figure 4.5: (Color online) Branching ratio of the calculated recombination rates $r_3^{(f\leftarrow i)}$ as functions of the collision energy E for the positive-scattering length case. The line-styles solid, dashed, dot, dash-dot and short-dashed indicate recombination rate to different recombination channels: $f = 1, 2, 3, 4, 5$, respectively. The thick black lines, thinner red lines and thinnest blue lines indicate recombination rates from three different incident channels: $i = 1, 2, 3$. The inset shows the branching ratio between the deep bound states only and it excludes the shallowest bound state (see the text for further details).

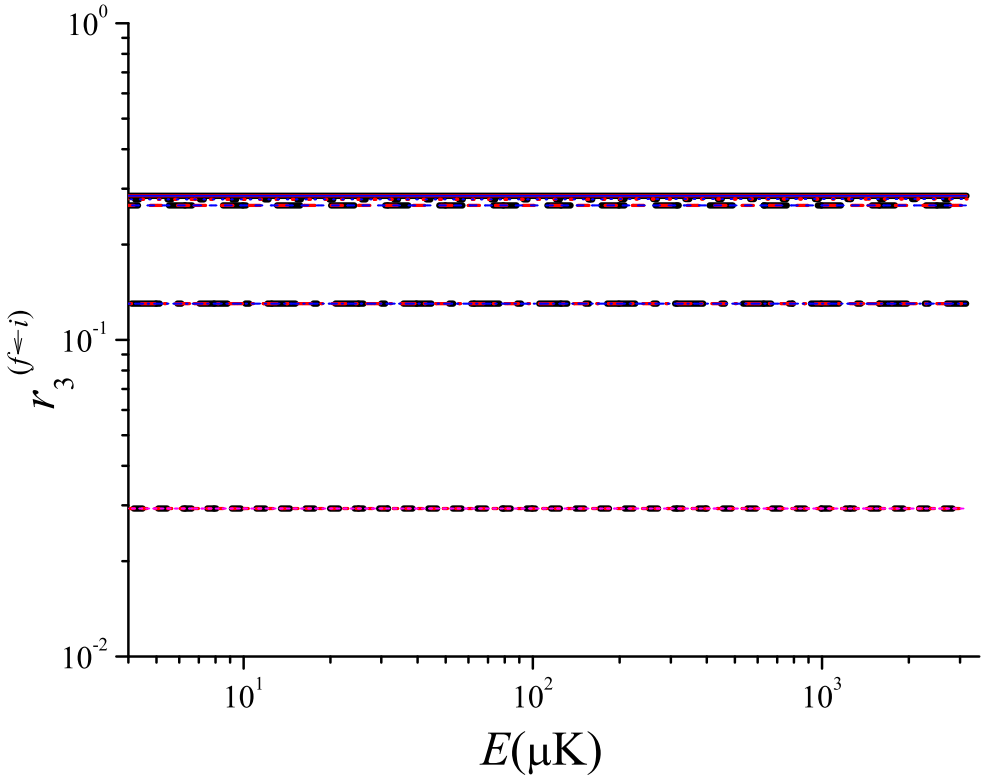

Figure 4.6: (Color online) Same as Fig. 4.5 but for the negative scattering length case.

4.4 Dominant recombination pathways

The extensive numerical three-body recombination rates presented in the preceding section are now interpreted in order to extract the important recombination pathways. Once these are identified, the surprising low-energy threshold behavior and the branching ratio regularities cited above become clear.

Our model consists of carrying out a perturbation expansion of the S-matrix and then associating each term to a specific pathway. As a first step, Eq. (2.17) is recast in matrix form as

$$\left[\underline{T_R} + \underline{W} - E\underline{1}\right]\underline{F} = 0, \tag{4.8}$$

where

$$(T_R)_{\mu\nu} = -\frac{1}{2\mu_{3b}}\frac{d^2}{dR^2}\delta_{\mu\nu} \tag{4.9}$$

and

$$W_{\nu\mu} = U_\nu\delta_{\nu\mu} - \frac{1}{2\mu_{3b}}\left[2P_{\nu\mu}\frac{d}{dR} + Q_{\nu\mu}\right]. \tag{4.10}$$

The off-diagonal terms of $\underline{W}$ are treated perturbatively, suggesting that the hyperradial Green's function matrix should be defined as the solution of

$$\left(\underline{T}_R + \underline{\widetilde{U}} - E\underline{1}\right)\underline{G}\left(R, R'\right) = \delta\left(R - R'\right)\underline{1} \tag{4.11}$$

where $\underline{\widetilde{U}}$ is the diagonal submatrix of $\underline{W}$, whose matrix elements coincide with $\widetilde{U}_\nu$ in Eqs. (4.5) and (4.6). One can, therefore, write the hyperradial Green's function as

$$\underline{G}\left(R, R'\right) = -\pi i\underline{f}\left(R_<\right)\underline{h}^{(+)}\left(R_>\right), \tag{4.12}$$

where $\underline{f}$ and $\underline{h}^{(+)}$ are both diagonal matrices. The matrix elements of $\underline{f}$ are the solutions of Eq. (4.11) regular at $R = 0$, and the outgoing Hankel solutions $\underline{h}$ are given by

$$h^{(+)}(R) = f(R) + ig(R), \tag{4.13}$$

where g represent the corresponding irregular solutions. For the three-body break-up channels, since the centrifugal barriers are dominant, the regular and irregular energy-normalized basis pair f_i and g_i are well approximated in terms of Bessel functions as

$$f_i(R) \approx \sqrt{\mu_{3b}R}J_{\lambda_i+2}(kR), \tag{4.14}$$

$$g_i(R) \approx \sqrt{\mu_{3b}R}Y_{\lambda_i+2}(kR). \tag{4.15}$$

The above hyperradial Green's function can now be used to expand the S-matrix in a distorted-wave Born series,

$$\mathcal{S}_{fi} = \mathcal{S}_{fi}^{(0)} + \mathcal{S}_{fi}^{(1)} + \mathcal{S}_{fi}^{(2)} + ..., \tag{4.16}$$

where

$$\mathcal{S}_{fi}^{(0)} = \delta_{fi} = 0, \tag{4.17}$$

($f \neq i$). In Eq. (4.16), the first order expansion of the scattering matrix element is simply given by,

$$\mathcal{S}_{fi}^{(1)} = 2\pi i \int_0^\infty dR f_f(R) W_{fi}(R) f_i(R), \tag{4.18}$$

and the low energy behavior of the S-matrix elements can be easily determined by inspection. The integrand in Eq. (4.18) is only significant at small values of kR where $f_i(R) = \sqrt{R}J_{\lambda_i+2}(kR) \propto k^{\lambda_i+2}$. Therefore,

$$\mathcal{S}_{fi}^{(1)} \propto k^{\lambda_i+2}. \tag{4.19}$$

In terms of the pathways, the first order S-matrix element is the probability amplitude to transit from the incident channel i and then tunnel through the centrifugal barrier and scatter into recombination channels at short distances ($R \propto r_0$). Therefore, if the recombination process were solely described by this pathway, the low energy behavior of recombination would be given by

$$K_3^{(f\leftarrow i)} = \frac{192\pi^2(2J+1)}{\mu_{3b}k^4}\left|\mathcal{S}_{fi}^{(1)}\right|^2 \propto k^{2\lambda_i} = E^{\lambda_i}, \tag{4.20}$$

recovering the usual threshold laws from Wigner's analysis [113, 103].

The first-order result shown in Eq. (4.20) for the low energy behavior of recombination fails, however, to explain our numerical coupled-channel results [see Figs. 3 and 5] implying that high order perturbation terms in Eq. (4.16) are crucial in order to determine the actual threshold laws. Hence we consider the second order partial-wave Born expansion, given by

$$\mathcal{S}_{fi}^{(2)} = -2\pi^2 \left(I_1 + I_2\right), \tag{4.21}$$

where,

$$\begin{aligned} I_1 &= \sum_{m\neq i\neq f} \int_0^\infty dR f_f\left(R\right) W_{fm}\left(R\right) f_m\left(R\right) \\ &\quad \times \int_R^\infty dR' h_m^{(+)}\left(R'\right) W_{mi}\left(R'\right) f_i\left(R'\right), \qquad (4.22) \\ I_2 &= \sum_{m\neq i\neq f} \int_0^\infty dR f_f\left(R\right) W_{fm}\left(R\right) h_m^{(+)}\left(R\right) \\ &\quad \times \int_0^R dR' f_m\left(R'\right) W_{mi}\left(R'\right) f_i\left(R'\right). \qquad (4.23) \end{aligned}$$

The first integral I_1 describes the quantum amplitude for a pathway in which the system coming inward in incident channel i to first scatter into an intermediate state m via a long-range coupling and then scatters to the final channel f at short distances. I_2 describes the amplitude for a different second-order pathway for which the system first scatters into an intermediate state m at short distances and then scatters into the final channel f in a second step. Accordingly in our analysis, the most important pathway for all incident channels is the one associated with the I_1 term in Eq. (4.21), i.e., the pathways incorporated in I_2 are much more strongly suppressed in the low-energy limit.

Interestingly, the second-order correction for the S-matrix element associated with the lowest three-body incidence channel ($i = 1$) can only be associated with an intermediate state (m) which is a deeply-bound molecular channel or else an excited three-body continuum channel. In both cases, our analysis shows that these contributions are unimportant in the low-energy limit. Therefore, the threshold law for the lowest three-body channel is still given by Eq. (4.20) [with $i = 1$, $\lambda_1 =$

0]. For recombination events starting from excited three-body channels ($i > 1$), however, the situation is different. In this case the dominant pathway is the one that involves the lowest three-body continuum channel as an intermediate channel ($m = 1$), with a corresponding second order correction:

$$\begin{aligned} S_{fi}^{(2)} \quad &\approx -2\pi^2 \int_0^\infty dR f_f\left(R\right) W_{f1}\left(R\right) f_1\left(R\right) \\ &\times \int_R^\infty dR' h_1^{(+)}\left(R'\right) W_{1i}\left(R'\right) f_i\left(R'\right). \end{aligned} \tag{4.24}$$

The long-range coupling W_{1i} between the lowest three-body break-up channel and a higher incident channel is dominated by the P-matrix element between the two channels. For different $i > 1$, the P-matrix element P_{1i} follows the same asymptotic behavior [54]

$$P_{1i}\left(R\right) \propto \frac{1}{R^2}, \qquad \left(R \to \infty\right). \tag{4.25}$$

Using the above equation and definition of $W_{\nu\mu}$ in Eq. (4.10), the integral in the second line of Eq. (4.24) has the property that

$$\int_R^\infty dR' h_1^{(+)}\left(R'\right) W_{1i}\left(R'\right) f_i\left(R'\right) \propto k. \tag{4.26}$$

The integral in the first line of Eq. (4.24) is the same as Eq. (4.18). Therefore, the second-order scattering-matrix element for the $i > 1$ three-body break-up channels follows

$$\mathcal{S}_{if}^{(2)} \propto k^{\lambda_1+2} k = k^3, \tag{4.27}$$

which is larger than the first-order S-matrix for channels $i > 1$ in the small k limit [see Eq. (4.19)]. Therefore, based on the discussions above, the threshold behavior of the partial recombination rate for any incident channel can be summarized as

$$K_3^{(i\leftarrow f)} \propto \begin{cases} E^0, & i = 1, \\ E^1, & i > 1, \end{cases} \tag{4.28}$$

which is consistent with our numerical results shown in Figs. 3 and 5.

The present analysis, therefore, demonstrates that the important recombination pathway for excited three-body incidence channels involves an intermediate transition to the lowest three-body incidence channel, controlled by a strong and long-range coupling between continuum channels [Eq. (4.25)]. This recombination pathway also explains why the relative recombination rate to reach the same final recombination channel from different incident three-body channels is the same. For ultracold collisions triggered from every excited three-body incidence channel ($i > 1$), our analysis shows that the final state contribution for recombination is mainly controlled by the coupling between the lowest three-body break-up channel at short distances. Therefore, the corresponding relative final state contribution are independent of the initial excited three-body channel.

4.5 Summary

The methodology elaborated in this chapter is capable of calculating recombination rate and, similarly, any other three-body scattering observable for systems that possess many two-body bound states. Our numerical study was performed for systems with up to 10 bound states, but it can be extended to larger problems with a good level of accuracy. Although our calculations for larger systems might be limited by memory usage and CPU time, our approach still allows for the analysis of increasingly more complex systems.

A key outcome is an understanding of the modified threshold laws for partial channel contributions to three-body recombination of three identical bosons with angular momentum $J = 0$. Our analysis for the important recombination pathways reveals that the threshold behavior of the recombination rate for excited three-body incidence channels is significantly less suppressed at low energy than a simple generalization of the Wigner's threshold laws predicts. In addition, the branching ratio of recombination into any given final state f is found to be the same for different incident channels.

Chapter 5

Origin of the Three-body Parameter Universality in Efimov Physics

Three-body recombination has been recognized as one of the most important scattering observables in which features related to universal Efimov physics can be manifested. This chapter focuses on studies of Efimov physics for $a \leq 0$. The field-free recombination rate at the negative site has an a^4 scaling plus some resonance features. These resonances, as was pointed out initially by [35], are closely related with the Efimov states. In principle, there are an infinite number of these resonances corresponding to the infinite expected number of Efimov states. In addition, the ratio between the positions of nearby resonances are universal, i.e., the ratio does not depend on the details of the short-range two- and three-body interactions. This fact implies that all resonance positions can be determined solely by a single parameter, known in the literature as the "three-body parameter". While previous fundamental assumptions in the theory of the Efimov effect suggest that the three-body parameter should not be universal, recent experiments support the opposite conclusion. The theoretical investigation in this chapter resolves this apparent contradiction by elucidating the unanticipated implications of two-body interactions. Our study shows that the three-body parameter universality emerges because a universal effective barrier in the three-body potentials prevents the three particles from simultaneously getting close to each other. Our results also show the limitations on this universality; it is more likely to occur for neutral atoms and less likely to extend to light nuclei.

Note that the material in this chapter has recently been published [115], and some of the text is adapted from that publication almost verbatim.

5.1 Introduction

Efimov physics was discovered by V. Efimov in the 1970's [26]. He predicted that when the two-body s-wave scattering length $a \to \infty$, there would be an infinite number of three-body bound states for a system consisting of three identical bosons. The energies of these three-body states obey the simple relation:

$$E_{3b}^{k+1}/E_{3b}^{k} = \exp\left(-2\pi/s_0\right), \tag{5.1}$$

where the integer k denotes the energy levels in ascending order. The geometric scaling factor $\exp\left(\pi/s_0\right) \approx 22.7$ is universal, i.e., it does not depend on the details of the two-body interaction nor additional three-body forces as long as both two- and three-body interactions are shortrange.

Equation (5.1) implies that we only need to know one additional "three-body parameter" to determine the absolute values of all the weakly bound Efimov spectra. One of the most fundamental assumptions underlying our theoretical understanding of this peculiar effect is that this three-body parameter should encapsulate all the details of the interactions at short distances [33]. For this reason, the three-body parameter has been viewed as nonuniversal since its value for any specific system would depend on the precise details of the underlying two- and three-body interactions [116, 117, 118]. Indeed, in nuclear physics, this picture seems to be consistent, i.e., three-body weakly bound state properties seem to be sensitive to the nature of the two- and three-body short-range interactions [117]. However, a recent experiment in ultracold atomic gases to study Efimov effects gives the opposite conclusion: the three-body parameter is universal for several different alkali atomic species.

Although the universality of the geometric scaling factor implies that the Efimov physics can be observed in any system consisting of three identical bosons, ultracold atom gases provide a perfect playground because of the extraordinary degree of control for such systems. One of the key experimental tools is to use a Fano-Feshbach resonance to magnetically tune the scattering length [119]. Tuning the scattering length a from infinity to finite and negative, but still much larger than the interaction range r_0, the Efimov energies cross the three-body threshold one by

one at some scattering length a_k^- (corresponding to the k^{th} Efimov state) and cause resonances in the three-body recombination. The resonance positions also obey a simple relation: $a_{k+1}^-/a_k^- = \exp(\pi/s_0)$. People usually use $a_{3\mathrm{b}}^- \equiv a_0^-$ corresponding to the Efimov ground state as the three-body parameter. Equivalently, the Efimov ground state energy E_{3b}^0 or the corresponding wave number $\kappa^* = \left(m_a \left|E_{3b}^0\right|/\hbar^2\right)^{1/2}$, where m_a is the atomic mass, can also be used as the three-body parameter.

Recently, Berninger et al. measured $a_{3\mathrm{b}}^-$ near four different Fano-Feshbach resonances with ultracold atomic gases of ^{133}Cs. Even though the short-range physics was expected to vary from one resonance to another, Efimov resonances were found for values of the magnetic field at which $a{=}a_{3\mathrm{b}}^-{=}{-}9.1(2)r_{\mathrm{vdW}}$, where r_{vdW} is the van der Waals length [120].[1] Therefore, in each of these cases, the three-body parameter was approximately the same, thus challenging a fundamental assumption of the universal theory. Even more striking is the observation in Ref. [6] that the Efimov resonance positions obtained for ^{39}K [7],[2] ^{7}Li [8, 9, 10], ^{6}Li [11, 12, 13, 14], and ^{85}Rb [15] are also consistent with values of $a_{3\mathrm{b}}^-/r_{\mathrm{vdW}}$ found for ^{133}Cs. These observations provide strong evidence that the three-body parameter has a universal character for spherically symmetric neutral atoms, therefore suggesting that **something else** beyond the universal theory needs to be understood.

5.2 Van der Waals interaction and classical suppression

Our theoretical model for two-body interactions mimics the tunability of the interatomic interactions via Fano-Feshbach resonances by directly altering the strength of the interparticle interactions and, consequently, leads to the desired changes in a. A Fano-Feshbach resonance is fundamentally a multichannel problem. However, for a broad resonance that is open-channel dominated, a single channel potential with van der Waals tail is a very good approximation [119]. This work considers various model interactions to test the universality of our three-body calculations.

[1] The van der Waals length is defined as $r_{\mathrm{vdW}} \equiv (2\mu_{2\mathrm{b}}C_6/\hbar^2)^{1/4}/2$ where C_6 is the van der Waals coefficient and the two-body reduced mass $\mu_{2\mathrm{b}}$. Note also that in Ref [6] the results were quoted in terms of the mean scattering length $\bar{a} \approx 0.9556 r_{\mathrm{vdW}}$ as defined in Ref. [120].

[2] Here, we are speculating that the feature observed in this experiment at $a = -11.02$ a.u. might in fact be a three-body resonance, instead of a four-body resonance. The possibility of such a reassignment is by no means proven, of course, and can only be answered through additional experimental studies.

The models we have used for the two-body interactions are:

$$v_{\rm sch}(r) = -D{\rm sech}^2\left(r/r_0\right), \tag{5.2}$$

$$v_\lambda^a(r) = -\tfrac{C_6}{r^6}\left(1-\lambda^6/r^6\right), \tag{5.3}$$

$$v_\lambda^b(r) = -\tfrac{C_6}{r^6}\exp\left(-\lambda^6/r^6\right), \tag{5.4}$$

$$v_{\rm vdW}^{\rm hs}(r) = B_{\rm hs}\Theta\left(r_{\rm hs}-r\right) - \tfrac{C_6}{r^6}\Theta\left(r-r_{\rm hs}\right). \tag{5.5}$$

The potential model in Eq. (5.2) is the modified Pöschl-Teller potential, where D determines the potential depth. Equation (5.3) is the usual Lennard-Jones potential, and Eq. (5.4) is a dispersion potential with a soft wall at short range. In Eq. (5.5), $\Theta(x)$ the step-function [$\Theta(x)=0$ for $x<0$ and 1 elsewhere. In practice, however, we have used a smooth representation of the step-function Θ in order to simplify our numerical calculations.] The potential in Eq. (5.5), therefore, consists of a hard-sphere potential for $r<r_{\rm hs}$ ($B_{\rm hs}\gg C_6/r_{\rm hs}^6$) and a long-range dispersion $-1/r^6$ potential for $r>r_{\rm hs}$. In the present study, the parameters D and λ in Eqs. (5.2)–(5.4) are adjusted to give the desired a and number of bound states. For convenience, we denote the values of D and λ at which there exist zero-energy bound states ($|a|\to\infty$) as D_n^* and λ_n^*, where n corresponds to the number of s-wave bound states. For the potential model in Eq. (5.5), however, we adjusted $r_{\rm hs}$ to produce the changes in a, but we only performed three-body calculations near the first pole at $r_{\rm hs}\approx 0.8828 r_{\rm vdW}$. While $v_{\rm sch}(r)$ is usually used to mimic the interaction potential between nuclei, potentials with van der Waals tails are very good models for interaction between neutral atoms.

5.2.1 Van der Waals interaction

One of the important properties of atomic gases is that the long-range two-body interaction between two neutral atoms can be very well described by a van der Waals interaction: $V_{\rm 2b}\left(r\right)\to -C_6/r^6$, where r is the interatomic distance. The asymptotic parameter C_6 is known quite well for most atomic pairs of interest, and determines the van der Waals length $r_{\rm vdW}=\left(2\mu_{2b}C_6/\hbar^2\right)^{1/4}/2$, where μ_{2b} is the two-body reduced mass. A corresponding energy scale $E_{\rm vdW}=\hbar^2/\left(2\mu_{2b}r_{\rm vdW}^2\right)$, called van der Waals energy, can also be defined. In general, when $r\gg r_{\rm vdW}$, the interaction is

described by the asymptotic van der waals interaction; when $r \ll r_{\mathrm{vdW}}$, $V_{2\mathrm{b}}(r)$ is dominated by complicated short-range physics.

Flambaum et al. have shown that, for a short-range potential well with a $-C_m/r^m$ tail (where m are integers), the low-energy two-body scattering properties have some "universal" features, providing that the short-range potential is "deep" enough to enable one to use semiclassical (or WKB) approximation within the potential well [121, 120]. In this case, the s-wave scattering length a and effective range r_{eff} are related by

$$r_{\mathrm{eff}} = F_m - \frac{G_m}{a} + \frac{H_m}{a^2}, \tag{5.6}$$

where F_m, G_m, and H_m only depend on the characteristic length scale $r_m = \left(2\mu C_m/\hbar^2\right)^{1/(m-2)}/2$ ($r_6 \equiv r_{\mathrm{vdW}}$ for van der Waals potential) and $\nu = 1/(m-2)$:

$$F_m = \frac{4}{3}\frac{\pi}{\sin\nu\pi}\nu^{2\nu}\frac{\Gamma(\nu)\Gamma(4\nu)}{[\Gamma(2\nu)]^2\Gamma(3\nu)}r_m, \tag{5.7}$$

$$G_m = \frac{16}{3}\frac{\pi}{\sin\nu\pi}\nu^{4\nu}\frac{\Gamma(1-2\nu)\Gamma(4\nu)}{\nu\Gamma(\nu)\Gamma(2\nu)\Gamma(3\nu)}r_m^2, \tag{5.8}$$

$$H_m = \frac{16}{3}\frac{\pi}{\sin\nu\pi}\nu^{6\nu}\frac{\Gamma(1-3\nu)\Gamma(1-\nu)\Gamma(4\nu)}{\nu^2[\Gamma(\nu)]^2[\Gamma(2\nu)]^2}r_m^3. \tag{5.9}$$

Equation (5.6) implies that the relation between effective range and scattering length only depends on the long-range behavior of the potential and does not depend on the complicated short-range physics. In another word, the relation is "universal". For a van der Waals potential, the effective range can be expressed as,

$$r_{\mathrm{eff}} \approx r_{\mathrm{vdW}}\left[2.78946 - 5.33333\frac{r_{\mathrm{vdW}}}{a} + 5.09856\left(\frac{r_{\mathrm{vdW}}}{a}\right)^2\right]. \tag{5.10}$$

In particular, at the pole $a \to \infty$, the effective range approximately equals to 2.78946 r_{vdW}.

5.2.2 Classical (WKB) Suppression

The universal relation between effective range and scattering length for potentials with van der Waals tails relies on the fact that the two-body zero-energy wave function at short-range can be well described by the WKB approximation. When the short-range potential well is deep, the WKB

approximation becomes very good, and the zero-energy wave function amplitude at short distances becomes very small. This WKB suppression could derive from the usual classical suppression (or WKB suppression) of the probability for two particles to exist between r and $r+dr$ in regions of high **local** velocity $\hbar k_L(r)$, which is proportional to $[\hbar k_L(r)/mdr]^{-1}$ (m being the particle mass), the time spent in that interval dr. It is possible that there could be an additional suppression as well, through quantum reflection from a potential **cliff** [122]. Systems supporting many bound states, such as the neutral atoms used in ultracold experiments with their strong van der Waals attraction, clearly exhibit this suppression. In general, a finite-range two-body potential that supports many bound states decreases steeply with decreasing interparticle distance r, starting when $r/r_{\rm vdW} \lesssim 1$, at which point the potential cliff plays a role analogous to a repulsive potential for low-energy scattering. As will be seen latter, the origin of the universality of the three-body parameter is also related to the suppression of the probability of finding two particles at distances $r < r_{\rm vdW}$. This suppression at the two-body level is studied here with different numerical models.

The first two-body model utilized in this chapter is the Lennard-Jones potential v^a_λ. Figure 5.1 shows three Lennard-Jones potentials with $\lambda = \lambda^*_2$, λ^*_3, λ^*_4 so that the 2nd, 3rd and 4th s-wave bound states are exactly at the threshold, and $a \to \infty$ for all the three cases. It is clear that these potentials agree with $-C_6/r^6$ for $r \gg r_{\rm vdW}$ and are very different at short distances $r \ll r_{\rm vdW}$. The inset shows the corresponding zero-energy wave functions. The wave functions again agree with each other at large distances and differ at short distances. However, the differences at short distances are very small, mainly because the wave function amplitude itself is very small. The amplitude of the zero-energy wave function at short-range becomes small because of classical suppression. Next, a detailed quantitative study of the suppression is carried out with all the model potentials in Eqs. (5.2)–(5.5).

The potential models in Eqs. (5.3)–(5.5) have in common the same large r behavior given by the van der Waals interaction with the characteristic length scale $r_{\rm vdW}$. Therefore, in order to compare the results from these models to those for $v_{\rm sch}$, we define an equivalent $r_{\rm vdW}$ for $v_{\rm sch}$ through the relationship between $r_{\rm vdW}$ and the effective range $r_{\rm eff}$ for $v_{\rm sch}$, namely, $r_{\rm vdW} \approx r_{\rm eff}/2.78947$

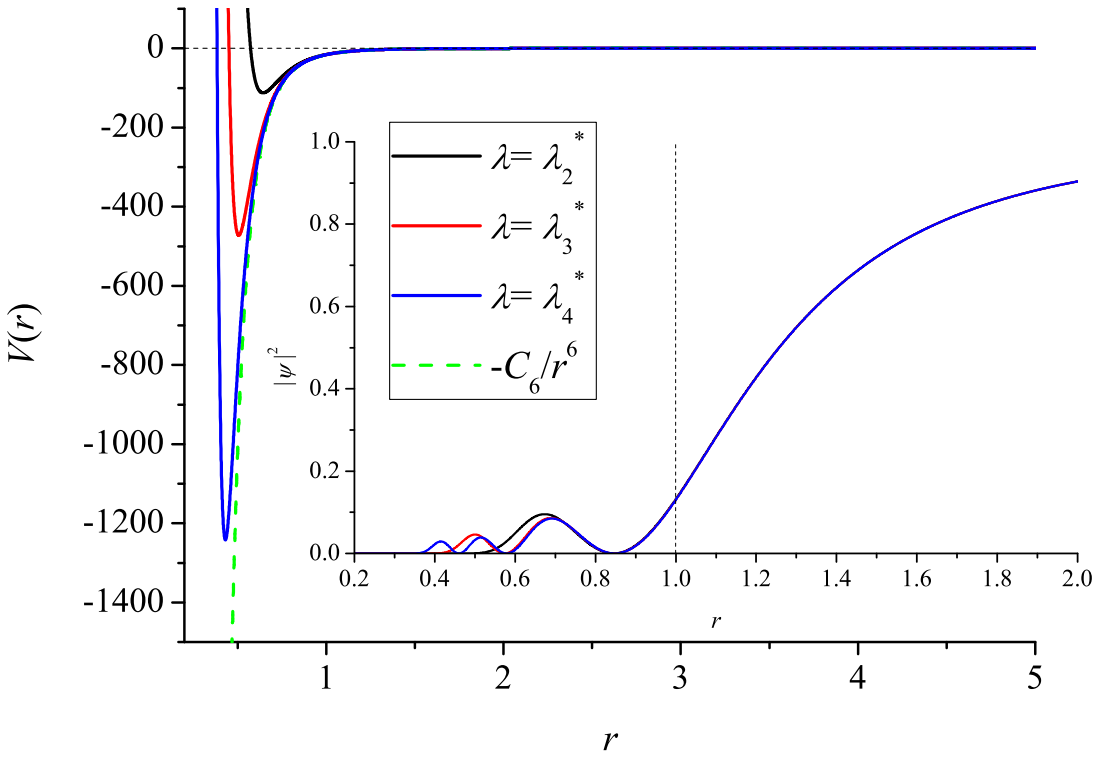

Figure 5.1: Lennard-Jones potential with the 2nd, 3rd and 4th s-wave bound state exactly at the threshold (denoted by $\lambda = \lambda_2^*, \lambda_3^*, \lambda_4^*$). The insert shows the corresponding zero-energy wave function.

[121, 120], which is valid for values of $|a| \gg r_0$. In fact, for $v_{\rm sch}$ we have found that $r_{\rm eff}(|a| = \infty)$ strongly depends on the potential depth D_n^* (shown in Fig. 5.2), while for van der Waals type of interactions, such as those in Eqs. (5.3)-(5.5), $r_{\rm eff}$ is fixed by $r_{\rm eff} \approx 2.78947(2\mu_{\rm 2b}C_6/\hbar^2)^{1/4}/2$.

Next we explore the origin of this suppression at the two-body level with these model potentials. To gain some insight into the likelihood of finding particles inside the potential well, we start by defining the following quantities,

$$\xi_p^{\rm in}(k) = \frac{1}{r_0}\int_0^{r_0} |\psi_k(r)|^2 {\rm d}r, \tag{5.11}$$

$$\xi_p^{\rm out}(k) = \lim_{r\to\infty} \frac{1}{r-r_0}\int_{r_0}^{r} |\psi_k(r)|^2 {\rm d}r, \tag{5.12}$$

where $\psi_k(r)$ is the two-body scattering wave function at energy $E_{\rm 2b} = k^2/2\mu_{\rm 2b}$, defined such that

$$\psi_k(r) \stackrel{r\to\infty}{=} \frac{\sin(kr+\delta)}{\sin\delta}, \tag{5.13}$$

with $\delta \equiv \delta(k)$ being the s-wave scattering phase shift. This definition for $\psi_k(r)$, therefore, leads to a zero-energy ($k \to 0$) wave function of the form: $\psi_0(r) = 1 - r/a$. [Note that in the above equations r_0 is the characteristic range of the two-body interaction. For the potential model in Eq. (5.2), r_0 is just the quantity in the argument of the sech function, while for the potential models in Eqs. (5.3)–(5.5) it is defined to be $r_0 = r_{\rm vdW}$].

The parameters $\xi_p^{\rm in}$ and $\xi_p^{\rm out}$ can be associated with the "average" amplitude of the wave function inside and outside the potential well, respectively. The amplitude inside the well **relative to the amplitude outside the well** is therefore defined as:

$$\xi_p^{\rm rel}(k) = \frac{\xi_p^{\rm in}(k)}{\xi_p^{\rm out}(k)} = 2\,\xi_p^{\rm in}(k)\sin^2\delta. \tag{5.14}$$

This relative amplitude vanishes in the limit $k \to 0$ ($\sin\delta \approx -ka$) as a result of our choice for the asymptotic solution in Eq. (5.13), except at $|a| = \infty$, when δ is an odd multiple of $\pi/2$. The quantity $\xi_p^{\rm in}(k)$, however, remains finite in the $k \to 0$ limit. Accordingly, this analysis suggests that $\xi_p^{\rm in}(k \to 0)$ is the most relevant parameter for our analysis of the suppression inside the well. Rigorously speaking, $\xi_p^{\rm in}$ is **not** a probability, but it does measure the likelihood of finding two

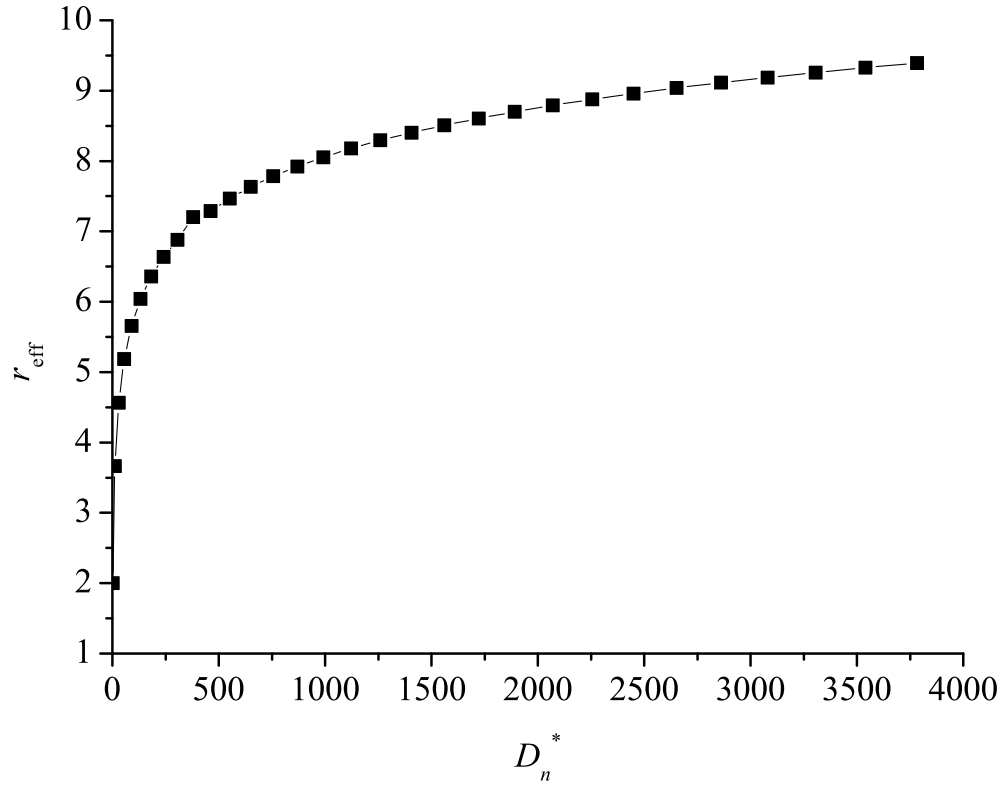

Figure 5.2: Effective ranges at the pole as a function of the potential depths D_n^* for v_{sch}.

particles within $r < r_0$, where the short-range interactions are experienced. Figure 5.3 presents a typical result for $|a|/r_0$ and $\xi_p^{\rm in}(k \to 0)$ for the two-body potential in Eq. (5.2). It also shows that in the universal regime near the poles in a, the wave function is suppressed (small $\xi_p^{\rm in}$) and documents the fact that this suppression becomes more efficient as the potential becomes deeper and more two-body states are bound. The black filled circles, open circles and open squares in Fig. 5.3 which show the values of $\xi_p^{\rm in}$ at $|a| \to \infty$, $a = 5r_0$, and $a = -5r_0$, respectively, illustrate this trend. Note, however, that for values $|a| \lesssim r_0$, the parameter $\xi_p^{\rm in}$ quickly increases, indicating a higher likelihood of finding particles inside the potential well. Similar results are also obtained for the potentials v_λ^a and v_λ^b [Eqs. (5.3) and (5.4), respectively].

The suppression in $\xi_p^{\rm in}$ (for a fixed value of $|a| \gg r_0$) can be understood to be a result of the usual semiclassical suppression of the wave function. The wave function inside the well is given by

$$\psi_{\rm WKB}(r < r_0) = \frac{C}{k_L^{1/2}(r)} \sin\left[\int^r k_L(r')dr' + \frac{\pi}{4}\right], \tag{5.15}$$

where C is a normalization constant, and $k_L^2(r) = 2\mu_{\rm 2b}[E_{\rm 2b} - v(r)]$ defines the **local** wave number $k_L(r)$. Therefore, for deep potentials, the suppression of the wave function inside the potential well is simply related to the factor $k_L(r)^{-1/2}$ that leads to amplitude suppression of the WKB wave function [Eq. (5.15)] between r and $r + dr$. Physically, this can be interpreted as the increase of the **local** velocity $\hbar k_L(r)/m$ (m being the particle mass) and the corresponding decrease in the time spent in that interval dr, $[mdr/\hbar k_L(r)]$. Therefore, in the WKB approximation, one expects $\xi_p^{\rm in}$ to be simply proportional to $1/k_L$. This expectation is tested in the Fig. 5.3 plot of the value of $1/k_L(r_0)$ (black dash-dotted line), showing that the suppression in $\xi_p^{\rm in}(k \to 0)$ is consistent with the semiclassical suppression described above. The relation between the universality of the three-body parameter and this classical suppression can be studied in the three-body level through the adiabatic hyperspherical representation.

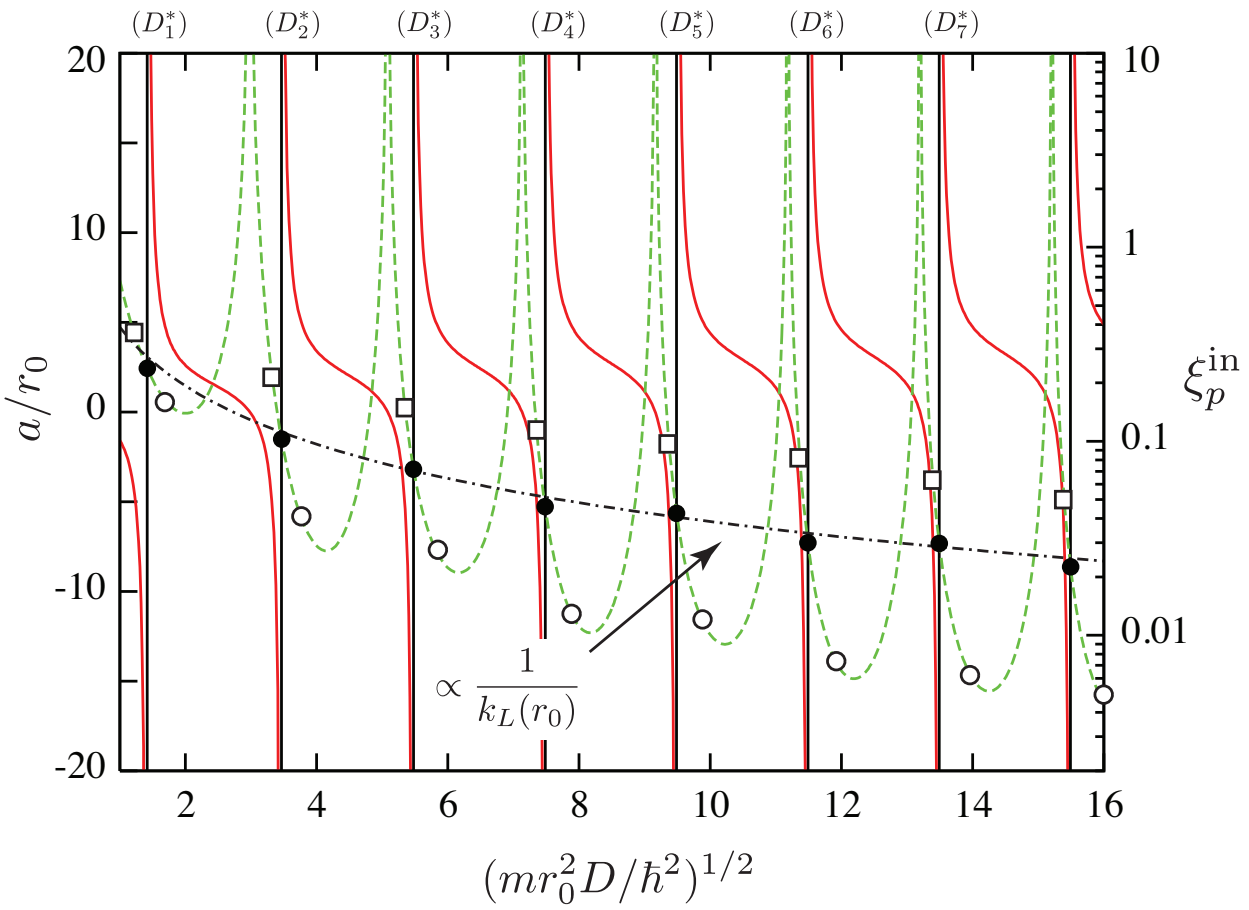

Figure 5.3: The red solid curve represents the scattering length, a/r_0, while the green dashed curve represents the parameter $\xi_p^{\rm in}(k \to 0)$. Both quantities are plotted as functions of the depth D of the two-body interaction model $v_{\rm sch}$ [Eq. (5.2)], whose values for which $|a| = \infty$ are indicated in the figure as D_n^*, where n is the number of s-wave states. The black circles, open circles, and open squares are the values of $\xi_p^{\rm in}$ at $|a| \to \infty$, $a = 5r_0$, and $a = -5r_0$, respectively. Their trends documents the suppression of the $\xi_p^{\rm in}$ as the number of bound states increases. The results for $\xi_p^{\rm in}$ also show higher efficiency of the suppression inside the well for $|a|/r_0 \gg 1$. The black dash-dotted curve shows the suppression factor $1/k_L(r_0)$, confirming the classical origin of the suppression mechanism.

5.3 Three-body adiabatic hyperspherical representation

Using the three-body potential as a summation of the two-body model potential from the last section, Eq. (2.12) is solved for the adiabatic potential and channel functions. Treating problems with deep two-body interactions — necessary to see strong inside-the-well suppression — requires us to solve Eq. (2.12) for two-body model interactions that support many bound states, a challenge for most theoretical approaches. Using our recently developed methodology in chapter 4 [95], however, we were able to treat systems with up to 100 two-body rovibrational bound states.

Figure 5.4(a) shows the adiabatic potentials U_ν at $|a| = \infty$ obtained using the two-body Lennard-Jones potential supporting 25 dimer bound states. At first glance, it is difficult to identify any universal properties of these potentials. Efimov physics, however, occurs at a very small energy scale near the three-body breakup threshold. Indeed, a closer analysis of the energy range $|E| < \hbar^2/mr_{\rm vdW}^2$ [Fig. 5.4 (b)] reveals the universal properties of the key potential curve controlling Efimov states and universal scattering properties.

Figure 5.4(b) shows one of our most important pieces of theoretical evidence for universality of the three-body parameter: the effective adiabatic potentials W_ν obtained using v_λ^a for more and more two-body bound states converge to a single universal curve. [In some cases in Fig. 5.4 (b) we have manually diabatized W_ν near sharp avoided crossings in order to improve the visualization. The details are discussed in Appendix E.] As one would expect, the usual Efimov behavior for the effective potentials, $W_\nu{=}-\hbar^2(s_0^2+1/4)/2\mu_{3\rm b}R^2$ with $s_0 \approx 1.00624$, is recovered for $R > 10r_{\rm vdW}$. It is remarkable, however, that W_ν also converge to a universal potential for $R < 10r_{\rm vdW}$ and, more importantly, these effective potentials display a repulsive wall or barrier at $R \approx 2r_{\rm vdW}$. This barrier prevents the close collisions that would probe the short-range three-body physics, including three-body forces known to be important in chemistry, thus making the three-body parameter universal, as we will confirm below. This is in fact our most striking result: **a sharp cliff or attraction in the two-body interactions produces a strongly repulsive universal barrier in the effective three-body interaction potential.**

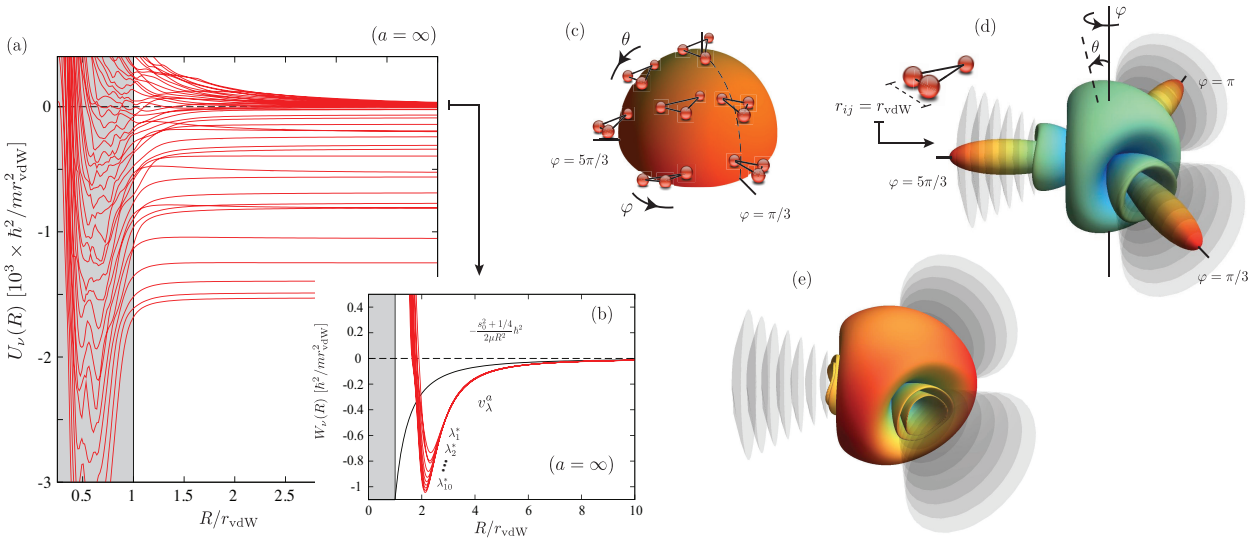

Figure 5.4: (a) Full energy landscape for the three-body potentials at $a=\infty$ for our v_λ^a model potential. (b) Effective diabatic potentials W_ν relevant for Efimov physics for v_λ^a with an increasingly large number of bound states (λ_n^* is the value of λ that produces $a=\infty$ and n s-wave bound states). The W_ν converge to a universal potential displaying the repulsive barrier at $R\approx 2r_{\rm vdW}$ that prevents particles access to short distances. (c)–(e) demonstrate the suppression of the wave function inside the potential well through the channel functions $\Phi_\nu(R;\theta,\varphi)$ for R fixed near the minima of the Efimov potentials in (b). (c) shows the mapping of the geometrical configurations onto the hyperangles θ and φ. (d) and (e) show the channel functions, where the "distance" from the origin determines $|\Phi_\nu|^{1/2}$, for two distinct cases: in (d) when there is a substantial probability of finding two particles inside the potential well (defined by the region containing the gray disks) and in (e) with a reduced probability — see also our discussion in Fig. 5.5. In (d) and (e), we used the potentials $v_{\rm sch}$ and v_λ^a, respectively, both with $n=3$.

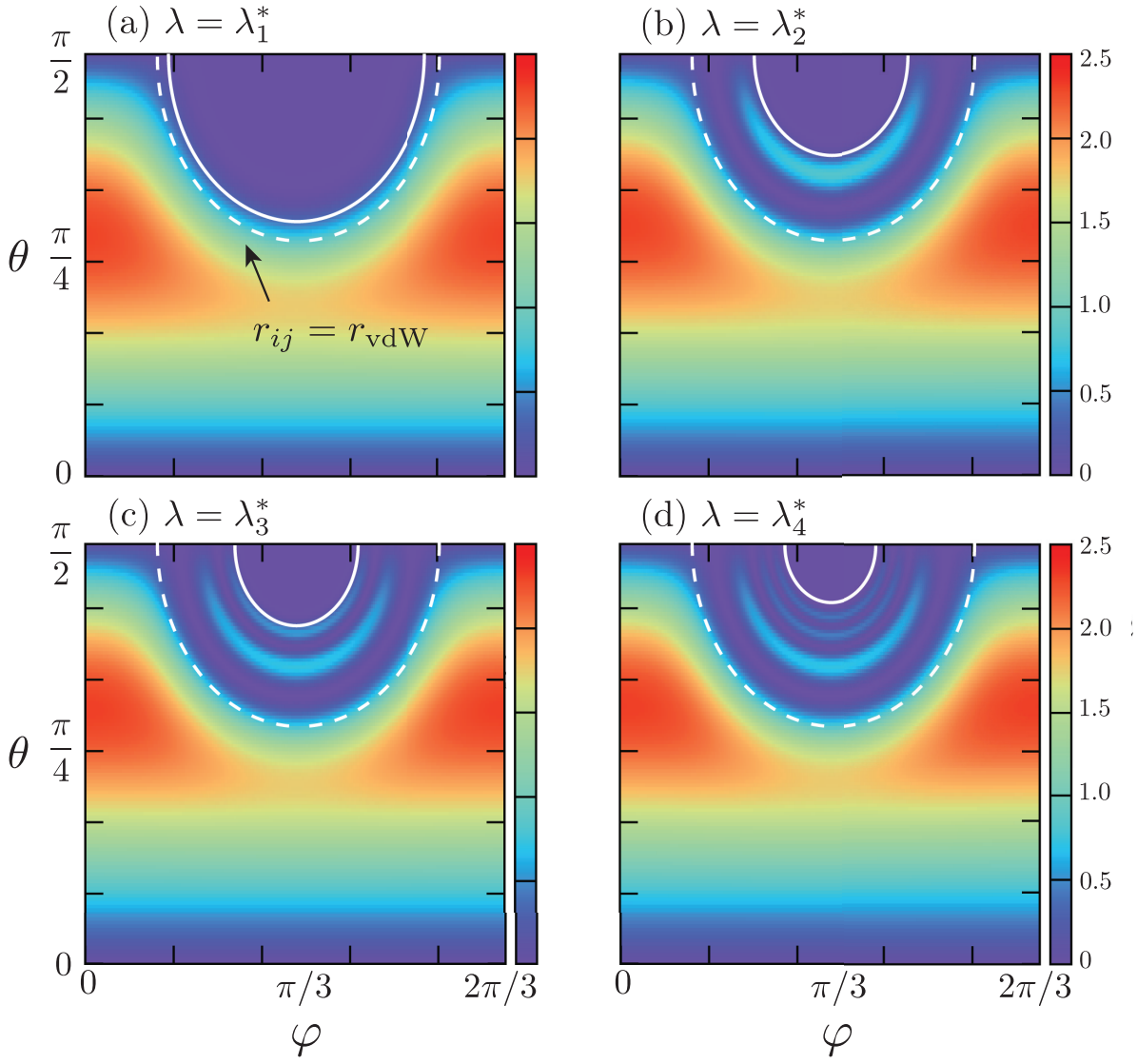

Figure 5.5: Density plot of the three-body probability density $|\Phi_\nu(R;\theta,\varphi)|^2 \sin 2\theta$ that determines the three particle configuration [see Fig. 5.4 (c)] in the θ-φ hyperangular plane for a fixed R ($\sin 2\theta$ is the volume element). (a)–(d) show the results for an R near the minima of the Efimov potentials in Fig. 5.4 (b) for the first four scattering length poles of the v_λ^a model, as indicated. (a) shows that there is a negligible probability of finding the particles at distances smaller than $r_{\rm vdW}$ (outer dashed circle) and, of course, inside the $1/r^{12}$ repulsive barrier (inner solid circle). For higher poles, i.e., as the strength of the hard-core part of v_λ^a potential decreases, the potential becomes deeper and penetration into the region $r < r_{\rm vdW}$ is now classically allowed. Nevertheless, (b)–(e) show that inside-the-well suppression still efficiently suppresses the probability of finding particle pairs at distances $r < r_{\rm vdW}$, found to be in the range 2–4%.

Qualitatively, this universality derives from the reduced probability of finding particles inside the attractive two-body potential well. This effect can be seen in terms of the channel functions Φ_ν, in Figs. 5.4 (c)–(d) and the hyperangular probability densities in Fig. 5.5. In the adiabatic hyperspherical representation, the space forbidden to the particles fills an increasingly larger portion of the hyperangular volume as R decreases. This evolution can be visualized as the dashed lines in Fig. 5.5 (a)–(d) expanding outward. In the process, the channel function Φ_ν is squeezed into an increasingly smaller volume, driving its kinetic energy higher and producing the repulsive barrier in the universal Efimov potential. Moreover, this suppression implies that the details of the interaction should be largely unimportant. Consequently, different two-body model potentials should give similar three-body potentials. Figure 5.6 demonstrates this universality by comparing W_ν obtained from different potential models supporting many bound states. Perhaps more importantly, it compares them with the results obtained from a two-body model that replaces the deep well by a hard wall, essentially eliminating the probability of observing any pair of atoms at short distances. [See $v_{\rm vdW}^{\rm hs}$ in Supplementary Eq. (5.5)]. Quantitatively, however, the fact that the barrier occurs only at $R \approx 2r_{\rm vdW}$ indicates that universality might not be as robust as in the cases discussed in Refs. [123, 124, 125, 126]. It is thus important to quantify the value of the three-body parameter to assess the size of nonuniversal effects. The next section focuses on the numerical study of the three-body parameter with different two-body model potentials and quantifies the universality.

In principle, the three-body parameter could be defined in terms of **any** observable related to Efimov physics [104]. Two of its possible definitions are [104]: the value of $a = a_{\rm 3b}^- < 0$ at which the first Efimov resonance appears in three-body recombination (see for instance Ref. [35]) and $\kappa_* = (m|E_{\rm 3b}^0|/\hbar^2)^{1/2}$, where $E_{\rm 3b}^0$ is the energy of the lowest Efimov state at $|a| \to \infty$.

5.4 Three-body parameters

Strictly speaking, when there are two or more s-wave bound states in the two-body model, the Efimov states are not real bound states but quasi-bound states with a finite width. This width is related to the decay processes to deeper dimer channels (than the Efimov channel) because of

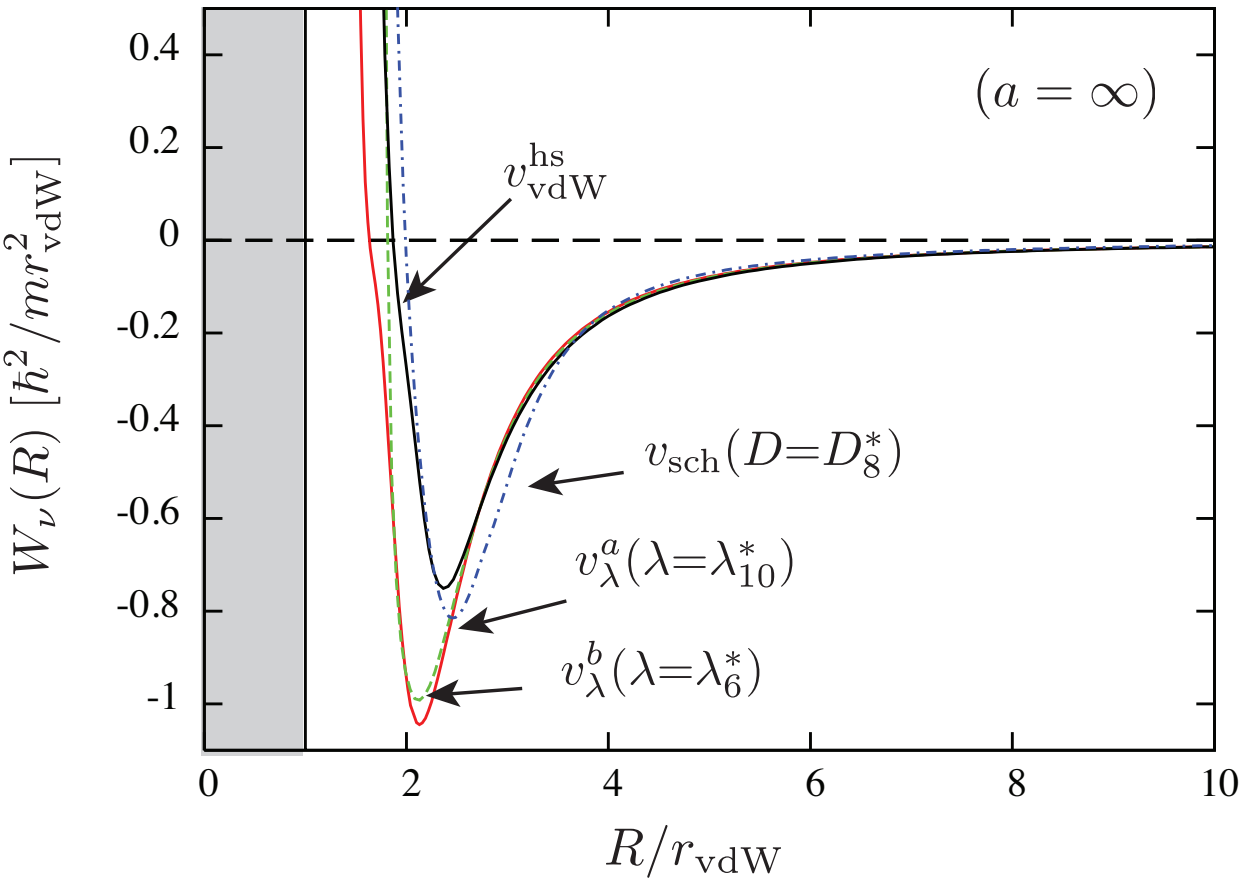

Figure 5.6: The Efimov potential obtained from the different two-body potential models used here. The reasonably good agreement between the results obtained using models supporting many bound states ($v_{\rm sch}$, v_λ^a and v_λ^b) and $v_{\rm vdW}^{\rm hs}$ [obtained by replacing the deep potential well with a hard wall but having only **one** (zero-energy) bound state] supports our conclusion that the inside-the-well suppression of the wave function is the main physical mechanism behind the universality of the three-body effective potentials. The differences between these potentials are seen to cause differences of a few percent in the three-body parameter.

the couplings at short distances. It is well known that when there is a quasi-bound state buried in the continua, the scattering amplitude in the continuous state and the quasi-bound state can interfere with each other and form a Fano resonance. In our case, the scattering matrix elements S_{ii} for deeper atom-dimer thresholds (denoted by i's) was calculated as a function of the energy E. Near the resonance due to an Efimov state, the quantity $|1 - S_{ii}|^2$ (which is closely related with the elastic scattering cross section) is fitted with the formula

$$|1 - S_{ii}|^2 = s_a \frac{(q + \varepsilon)^2}{1 + \varepsilon^2} + s_b, \tag{5.16}$$

where s_a, s_b, and q are fitting parameters, and $\varepsilon = \left(E - E^0_{3b}\right) / \left(\Gamma^0_{3b}/2\right)$ gives the resonance position (Efimov energy) E^0_{3b} and the width Γ^0_{3b}.

Figure 5.7 shows an example of fitting the resonance energy and the width using Fano lineshapes. The system studied here consists of three identical bosons with a total angular momentum of $J = 0$ interacting with each other via a Lennard-Jones potential v^a_λ. The λ is chosen to be equal to λ^*_2 corresponding to the case where the second s-wave bound state is exactly at the threshold. There are three deeper dimer channels corresponding to a g-wave dimer, a d-wave dimer, and a deep s-wave dimer. The calculated quantities $|1 - S_{ii}|^2$ for each atom-dimer channel are shown in the black squares, red triangles, and blue circles for the g-wave, d-wave and s-wave channel, correspondingly. The solid curves are the results of the fitting formula in Eq. (5.16), and show a very good agreement between the fitting and the numerical results. In this case, the Efimov energy $E^0_{3b} \approx -0.0498 E_{vdW}$ and $\Gamma^0_{3b} \approx 0.0078 E_{vdW}$ are deduced from the fitting.

This method can also be applied to finding higher Efimov states and to finite scattering length cases. Figure 5.8 shows the Efimov scenario using v^b_λ near the second pole $\lambda = \lambda^*_2$. The red curve with solid circles corresponds to the Efimov ground state, and the black curve with solid square symbols represents the Efimov first-excited state. The blue dashed curve shows the shallowest s-wave dimer energy. At the negative site, the Efimov energies cross the three-body break-up threshold at some values of a^-_k, which can be deduced from extrapolations. For the case studied here, $a^-_0 \approx -9.35$ and $a^-_1 \approx -158.37$ are deduced from extrapolations. The ratio $a^-_1/a^-_0 \approx 16.93$

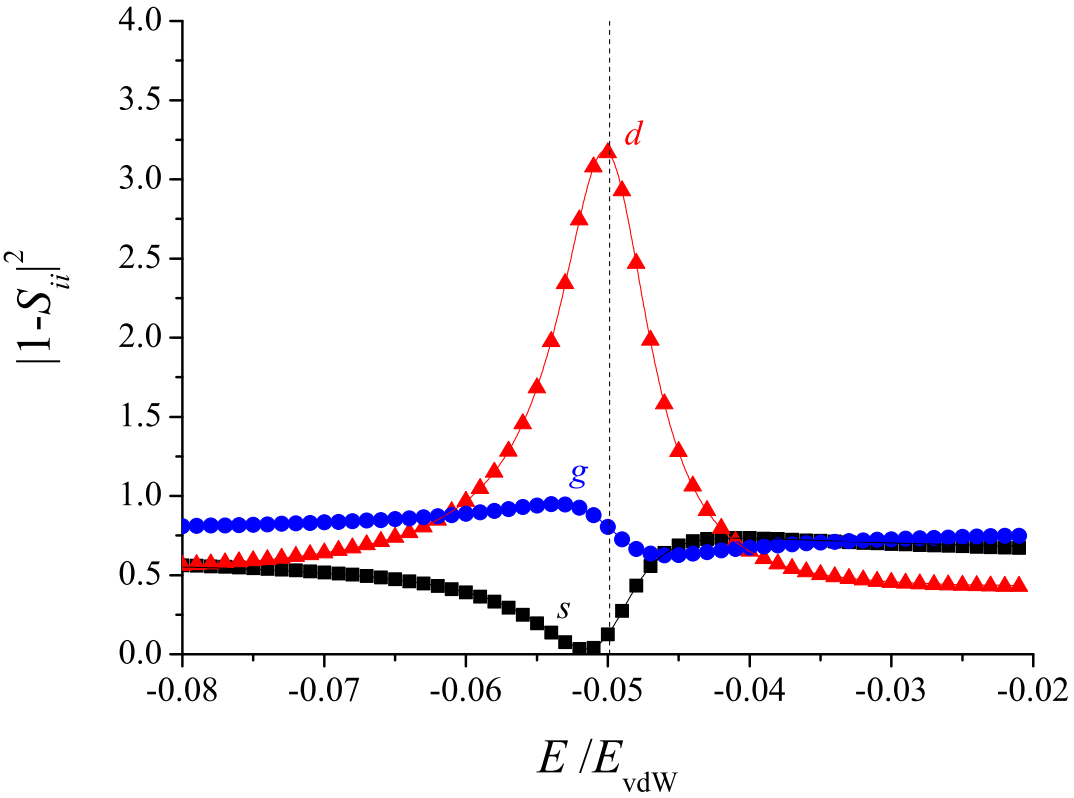

Figure 5.7: Fitting the Efimov resonance using a fano lineshape [Eq. (5.16)] for a system using the two-body model potential v_λ^a with $\lambda = \lambda_2^*$. The blue circles, red triangles, and black squares are the numerically calculated $|1 - S_{ii}|^2$ for the three deeper atom-dimer channels (a g-wave dimer, a d-wave dimer, and a deeper s-wave dimer, correspondingly.) The curves are fitting results from using Eq. (5.16).

deviates from the universal value 22.7 because of the finite range correction. When an Efimov state crosses the three-body break-up threshold, a resonance shows up in the three-body recombination rate.

Figure 5.9 shows the three-body recombination rate as a function of scattering length and exhibits a clear resonance structure. A zero-range model gives an analytical formula for the three-body recombination rate near an Efimov resonance at zero temperature ($E \to 0$) [104]:

$$K_3 = A_K \frac{\sinh(2\eta)}{\sin^2\left[s_0 \ln\left(a/a_0^-\right)\right] + \sinh^2\eta}. \tag{5.17}$$

This formula is used to fit the numerically calculated three-body recombination rate and to deduce the resonance position $a_0^- \approx -9.18$. This value is very close to the position of an Efimov state crossing the threshold given by the extrapolation method mentioned in the last paragraph (which is about -9.35). The small difference might be due to the finite range correction and the finite temperature corrections.

Directly calculating K_3 and extrapolating the Efimov energy can give approximately the same answer for a_k^-. This fact has also been checked numerically for several other two-body model potentials with 2–4 s-wave bound states. However, calculating the Efimov energy is usually faster and more stable. Therefore, in the next subsection, the extrapolation method is used to study $a_{3\mathrm{b}}^- \equiv a_0^-$ for all the different two-body potential models.

5.4.1 Universality of the three-body parameter

To study the universality of the three-body parameter, different two-body potential models are utilized. Our numerical results for κ_* and $a_{3\mathrm{b}}^-$ are summarized in Figs. 5.10(a) and (b), respectively, demonstrating their universality in the limit of many bound states. In fact, the values for κ_* and $a_{3\mathrm{b}}^-$ in this limit differ by no more than 15% from the $v_{\mathrm{vdW}}^{\mathrm{hs}}$ results — $\kappa_* = 0.226(2)/r_{\mathrm{vdW}}$ and $a_{3\mathrm{b}}^- = -9.73(3) r_{\mathrm{vdW}}$ [solid black line in Fig. 5.10(a) and (b)] — indicating, once again, that the universality of the three-body parameter is dependent upon the suppression of the probability density within the two-body potential wells. Given this picture, we attribute the variations of κ_*

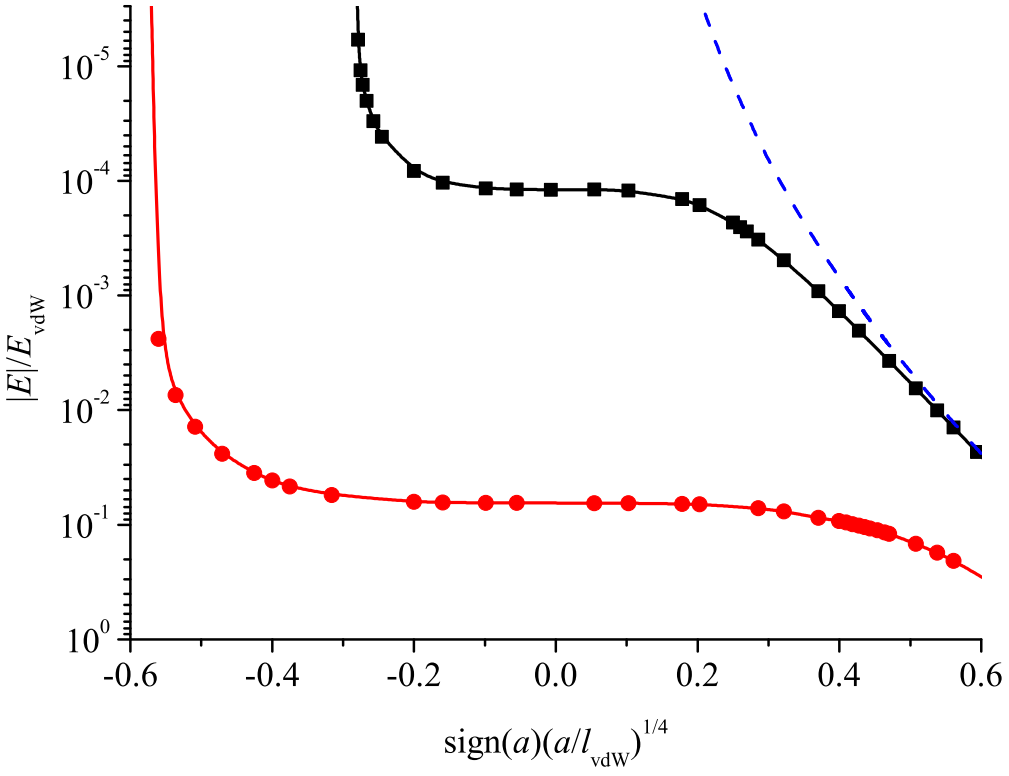

Figure 5.8: Efimov scenario calculated for v_λ^b with $\lambda = \lambda_2^*$. Both the ground and first excited Efimov spectra as a function of $\mathrm{sign}(a)(a/r_{\mathrm{vdW}})^{1/4}$are shown.

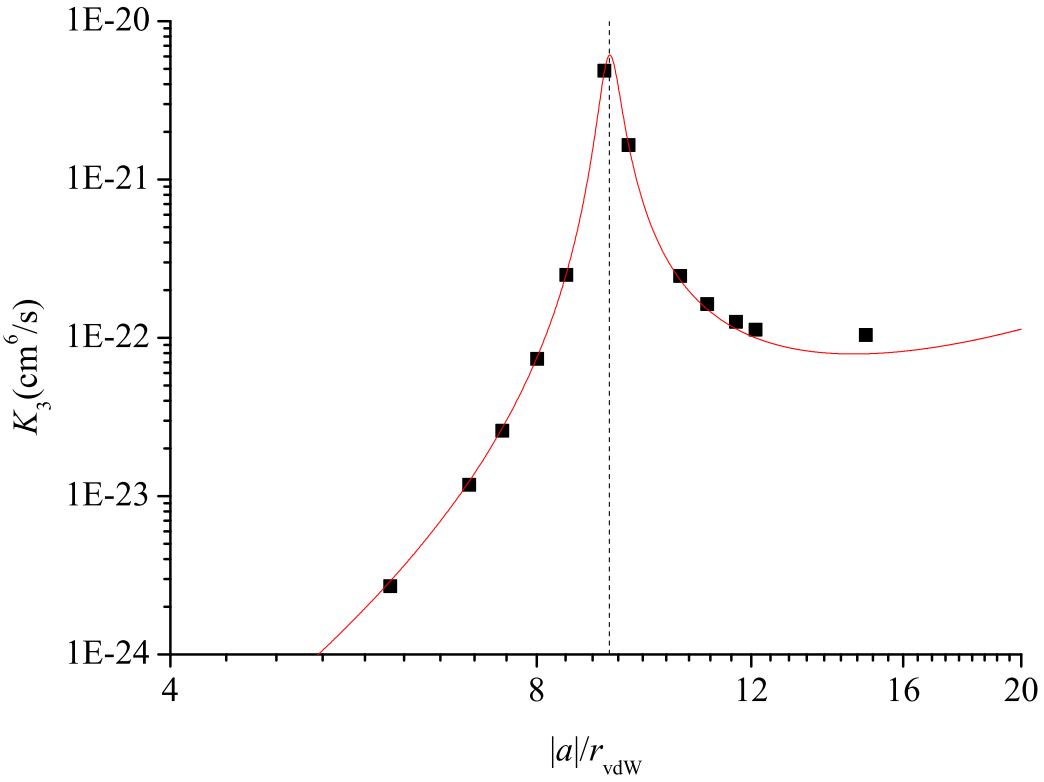

Figure 5.9: The Efimov resonance corresponding to the Efimov ground state. The black squares are numerically calculated results, and the solid curve is the fitting result from using Eq. (5.17).

and a_{3b}^{-} in Fig. 5.10 to the small, but finite, probability of reaching short distances, thus introducing nonuniversal effects related to the details of the two- and three-body forces. Nevertheless, our results for a_{3b}^{-} are consistent with the experimentally measured values for ^{133}Cs [34, 6], ^{39}K [7], ^{7}Li [8, 9, 10], ^{6}Li [11, 12, 13, 14],[3] and ^{85}Rb [15], all of which lie within about 15% of the $v_{\rm vdW}^{\rm hs}$ result. Curiously, if one simply averages the experimental values, then the result differs from the $v_{\rm vdW}^{\rm hs}$ result by less than 3%.

Previous treatments have failed to predict the universality of the three-body parameter for various reasons. In treatments using zero-range interactions, for instance, the three-body parameter enters as a free parameter to cure the Thomas collapse [33], preventing any statement about its universality. Finite-range models, such as those used in some of our own treatments [118] [corresponding to the results for $v_{\rm sch}$ with $n = 2$ and 3 in Figs. 5.10 (a) and (b)], have failed for lack of substantial suppression of the probability density in the two-body wells. This scenario, however, should reflect better the situation for light nuclei having few bound states and shallow attraction. In contrast to Ref. [118], other models [127, 128, 129, 125, 130, 131] have found better agreement with experiment. Our analysis of these treatments, however, indicates that the two-body models used have many of the characteristics of our $v_{\rm vdW}^{\rm hs}$, therefore satisfying the prerequisite for a universal three-body parameter.

A recent attempt [16] to explain the universality of the three-body parameter avoided explicit two-body models altogether, using instead an **ad hoc** hyperradial potential that bore little resemblance to our numerical potentials in Fig. 5.4. This **ad hoc** three-body potential displayed strong attraction at short distances in contrast to our key finding that a cliff of attraction for two bodies produces a universal **repulsive** barrier in the three-body system. Consequently, even though a universal three-body parameter was found in Ref. [16], the fundamental understanding provided by the approach is uncertain. We also construct a simple single channel model according to our numerical findings. The differences between the two models and our single channel model

[3] For the experiments with ^{6}Li [11, 12, 13, 14], we have determined a_{3b}^{-} by using the definition of the mean scattering length from: Wenz, A. N. **et al.**, Phys. Rev. A **80**, 040702(R) (2009).

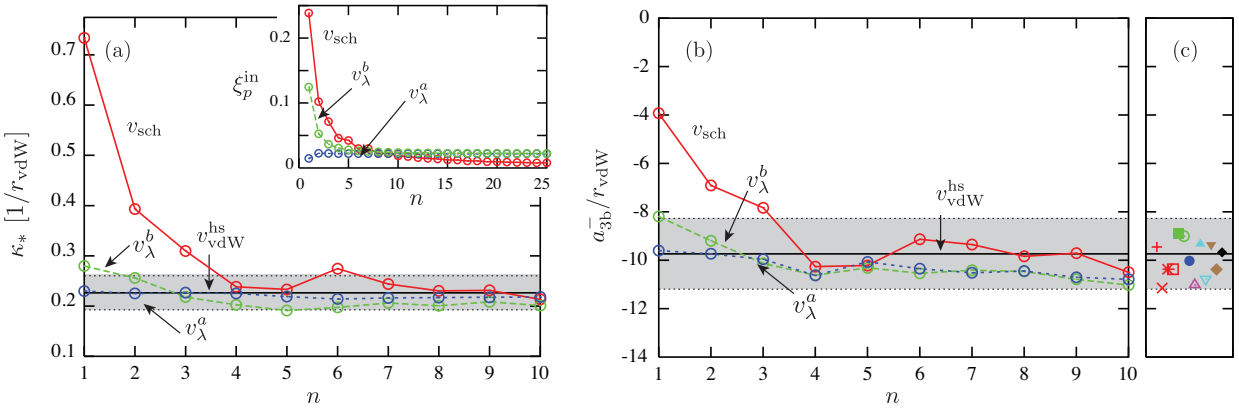

Figure 5.10: Values for the three-body parameter (a) κ_* and (b) $a_{\rm 3b}^-$ as functions of the number n of two-body s-wave bound states for each of the potential model studied here. (c) Experimental values for $a_{\rm 3b}^-$ for ^{133}Cs [6] (red: $\times$, $+$, $\square$, and $*$), ^{39}K [7] (magenta: $\triangle$), ^{7}Li [8] (blue: $\bullet$) and [9, 10] (green: $\blacksquare$ and $\circ$), ^{6}Li [11, 12] (cyan: $\blacktriangle$ and $\triangledown$) and [13, 14] (brown: $\blacktriangledown$ and $\Diamond$), and ^{85}Rb [15] (black: $\blacklozenge$). The gray region specifies a band where there is a $\pm 15\%$ deviation from the $v_{\rm vdW}^{\rm hs}$ results. The inset of (a) shows the suppression parameter $\xi_p^{\rm in}$ [Eq. (5.11)] which can be roughly understood as the degree of sensitivity to nonuniversal corrections. Since $\xi_p^{\rm in}$ is always finite — even in the large n limit — nonuniversal effects associated with the details of the short-range interactions can still play an important role. One example is the large deviation in κ_* found for the $v_{\rm sch}$ ($n = 6$) model, caused by a weakly bound g-wave state. For $n > 10$ we expect κ_* and $a_{\rm 3b}^-$ to lie within the range of 15% established for $n \leq 10$.

are presented in detail in the next subsection.

5.4.2 Single channel approximation

The strong multichannel nature of the problem can be illustrated by comparing the results obtained from a single channel approximation, i.e., $W_{\nu\nu'}(R) = 0$ ($\nu \neq \nu'$), with our solutions of the fully coupled system of equations. Figure 5.11 (a) shows the three-body parameter κ_* [related to the energy of the lowest Efimov state through the relation $\kappa_* = (mE/\hbar^2)^{1/2}$] obtained for the v_λ^a model obtained in the single channel approximation (open triangles) as well as our full numerical results (open circles). The disagreement between these quantities increases with the number of s-wave bound states n, meaning that the physics controlling the results becomes more and more multichannel in nature. Nevertheless, we find that by imposing a simple change in the adiabatic potentials near the barrier — to make the barrier **more** repulsive [see Fig. 5.11 (b)] — the single channel approximation for κ_* [filled circles in Fig. 5.11 (a)] reproduces the full numerical calculations much better. This agreement indicates that most of the nonadiabaticity of the problem is related to the exact shape of the barrier and that, to some extent, the effect of the nonadiabatic couplings is to make the effective potential W_ν more repulsive. For these reasons and, of course, the universality of our full calculations (see for instance Fig. 5.10), we believe that the short-range barrier in the three-body effective potentials indeed offers a physically valid explanation of the universality of the three-body parameter. We emphasize, though, that Fig. 4 only includes the results from our essentially exact solutions of the full calculations. The single channel results discussed here are intended only as support of our physical interpretation.

It is within this context that we analyzed the model proposed in Ref. [16]. In Ref. [16], the three-body effective potential important for Efimov physics was estimated by considering the different aspects controlling the physics at small and large distances. At distances comparable to $R = r_{\rm vdW}$, it was assumed that the effective three-body potential is dominated by the contributions from equilateral triangle geometries and included only on two-body interactions. Under these assumptions, $r_{12} = r_{23} = r_{31} = r$ giving $R = 3^{1/4} r$ (note that our definition for R differs from that

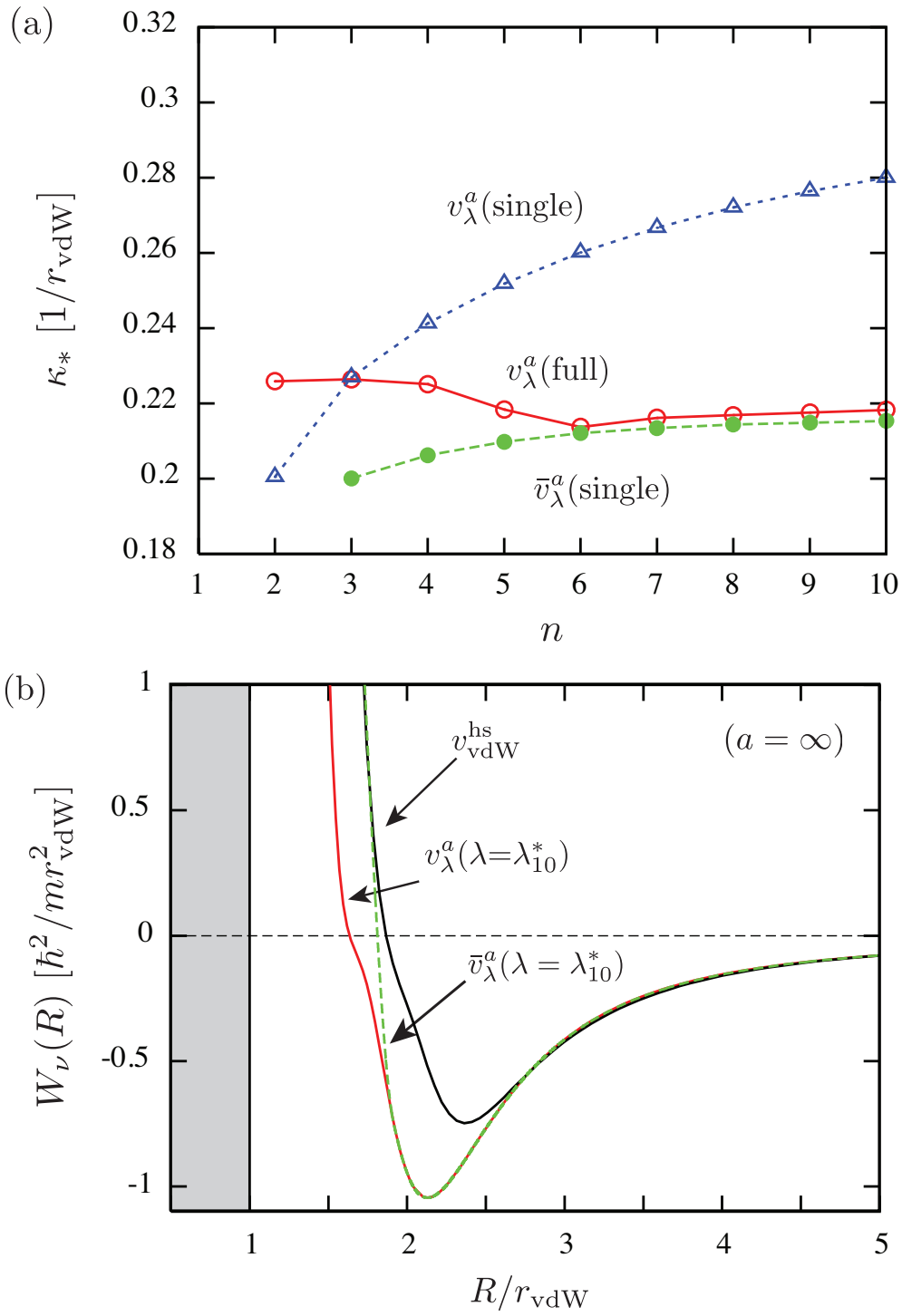

Figure 5.11: (a) This figure compares the energies (as characterized by the three-body parameter κ_*) obtained from a single channel approximation with our full calculations. The three-body parameter κ_* is shown for the v_λ^a model in the single channel approximation (open triangles) as well as for our full numerical results (open circles). The single channel approximation can be improved by imposing a simple change in the adiabatic potentials near the barrier, as is shown in (b). There we smoothly connect the potential for v_λ^a (red solid line) to the barrier obtained for $v_{\rm vdW}^{hs}$ (black solid line), resulting in the potential labeled by $\bar{v}_\lambda^a$ (green solid line). This new potential is actually more repulsive and has energies [filled circles in (a)] that are much closer to our full numerical calculations.

used in Ref. [16]), the effective potential can be written as

$$\begin{aligned} V_m(R) &= -C_6/r_{12}^6 - C_6/r_{23}^6 - C_6/r_{31}^6 \\ &= -3C_6/r^6 = -3\times 3^{3/2}C_6/R^6. \end{aligned} \tag{5.18}$$

This potential is expected to be valid for distances $R < \bar{A} = 4\pi\Gamma(1/4)^{-2}3^{1/4}3^{3/8}r_{\rm vdW} \approx 1.9r_{\rm vdW}$ [120]. With our method, however, we have the means to check the validity of Eq. (5.18) by comparing it with our numerically calculated potentials. Figure 5.12 shows the three-body potentials obtained using the $v_\lambda^a(\lambda = \lambda_{10}^*)$ model supporting a total of 100 two-body bound states. The potential from Eq. (5.18) is the black solid line passing near the series of avoided crossings and might be loosely viewed as diabatically connecting the fully numerical potentials. This relation is reasonable given that this sequence of avoided crossings has been shown in Ref. [132] to be related to the transition of the system from an equilateral triangle geometry to other geometries. This figure therefore suggests that approximating the short range physics by Eq. (5.18) is not wholly unphysical, but its validity depends on a strong assumption of diabaticity through a large number of avoided crossings and is thus probably **not** an approximation satisfactory for a more quantitative analysis.

The potential in Eq. (5.18), however, was not actually used in the calculations in Ref. [16]. Instead, it was used to motivate a claim that three-body quantum reflection plays an important role, allowing the short range behavior to be replaced by a repulsive potential for distances $R < \bar{A} \approx 1.9r_{\rm vdW}$. It is interesting to note that the value $R \approx 1.9r_{\rm vdW}$ obtained from Ref. [16] for the position of the hard wall is quite close to the hyperradius where our potentials exhibit the universal barrier (see Fig. E.1, for instance), indicating that $\bar{A}$ might have some physical meaning. It is worth mentioning, however, that the barrier we observed in our calculations is model independent, i.e., it doesn't rely on the particular model used for the two-body interaction. For distances $R > \bar{A}$, the model in Ref. [16] assumed the three-body effective potentials to be given by the universal Efimov formula,

$$V_E(R) = -\hbar^2\frac{s_0^2 + 1/4}{2\mu R^2}. \tag{5.19}$$

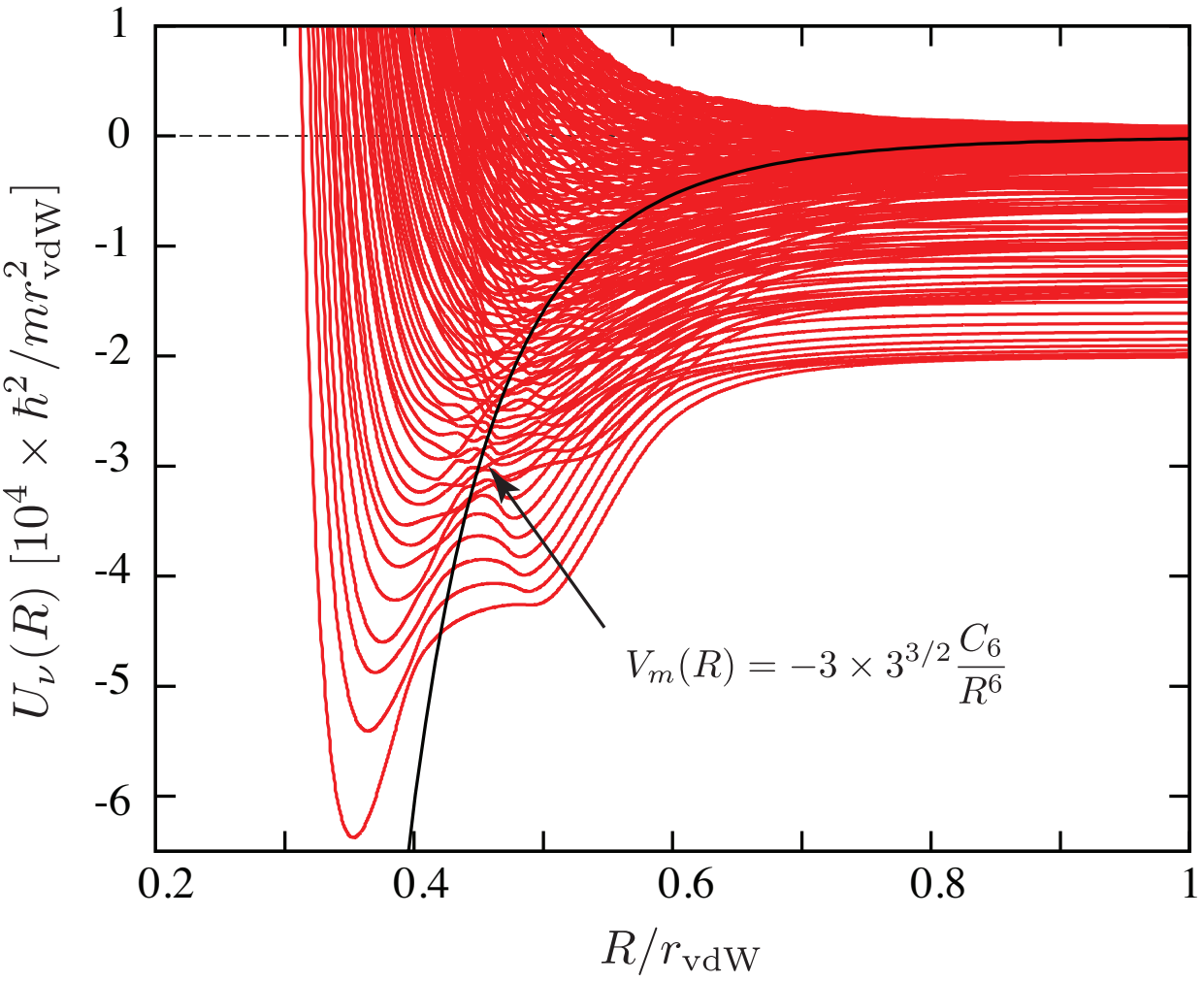

Figure 5.12: This figure shows the three-body potentials obtained using the $v_\lambda^a(\lambda = \lambda_{10}^*)$ model supporting a total of 100 bound states. Roughly speaking, the potential of Eq. (5.18) [16] (black solid line) can be seen as a diabatic potential since it passes near one of the series of avoided crossings.

It is well known [**?**], however, that this potential is valid for $r_{\rm vdW} \ll R \ll |a|$, and $R = 1.9 r_{\rm vdW}$ is certainly out of this range. In fact, one can see in Fig. 1 (b) that the use of the Efimov potential [Eq. (5.19)] for $R < 10 r_{\rm vdW}$ is a crude approximation. Nevertheless, using this model, Ref. [16] obtains $a_{\rm 3b}^{-} \approx -9.48 r_{\rm vdW}$, a value consistent with experiments [34, 6, 7, 8, 9, 10, 11, 12, 13, 14, 15] as well as with our present calculations for $a_{\rm 3b}^{-}$.

However, extending the model of Ref. [16] to the limit $|a| = \infty$, we obtained $\kappa_* \approx 0.037/r_{\rm vdW}$. Our result, by way of contrast, using $v_{\rm vdW}^{\rm hs}$ [Eq. (5.5)] is $\kappa_* = 0.226(2)/r_{\rm vdW}$. We also have tested the effects of finite a corrections on the model of Ref. [16] by replacing Eq. (5.19) with the three-body potential obtained with a zero-range model of the two-body interactions [133]. These corrections are particularly important near $R = |a|$. With this modification, the model of Ref. [16] leads to $a_{\rm 3b}^{-} \approx -39.96 r_{\rm vdW}$. For these reasons, we believe that this model's agreement with our results and experimental data is fortuitous.

While multichannel couplings are needed to quantitatively describe this system, it is possible to construct an effective hyperradial potential curve that correctly describes the behavior of three atoms in the universal regime. Such a potential curve could be useful for simplified future studies. The approximate form obtained from the present study is:

$$\frac{2\mu r_{\rm vdW}^2}{\hbar^2} W_\nu^u(R) \approx -\frac{s_0^2 + 1/4}{(R/r_{\rm vdW})^2} - \frac{2.334}{(R/r_{\rm vdW})^3} - \frac{1.348}{(R/r_{\rm vdW})^4} - \frac{44.52}{(R/r_{\rm vdW})^5} + \frac{4.0 \times 10^4}{(R/r_{\rm vdW})^{16}}. \quad (5.20)$$

Here μ is the three-body reduced mass and r_{vdW} is the two-body van der Waals length. For comparison the speculative potential curve proposed by Chin [16] is shown, which does not resemble the present result even qualitatively at small distances, as it exhibits far too little attraction in the region $R = 2 - 5 r_{\rm vdW}$.

5.5 Summary

In summary, our theoretical examination shows that the three-body parameter controlling much of universal Efimov physics can also be a universal parameter under certain circumstances which should be realized in most ultracold neutral atom experiments. Provided the underlying

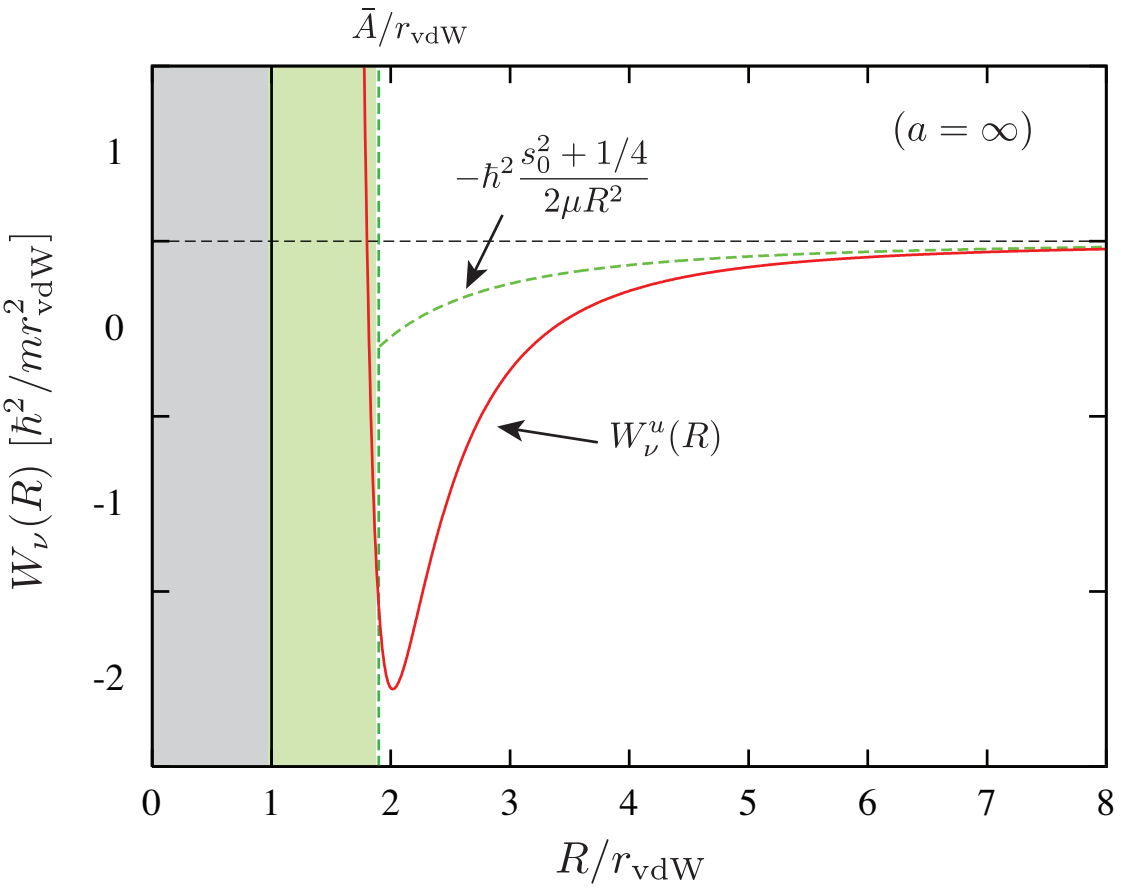

Figure 5.13: Comparison between the effective potential obtained from Ref. [16] and the potential from Eq. (5.20).

two-body short-range interaction supports a large number of bound states, or it has some other property leads to the suppression of the wave function at short distances, three-body properties associated with Efimov physics can be expected to be universal. This surprising new scenario could not have been, and was not, anticipated from the simple model calculations to date. Ironically, increasing the complexity of the model simplified the outcome by effectively eliminating the impact of the deeply bound two- and three-body states on the low-energy bound and scattering three-body observables. That is, the three-body parameter becomes largely universal.

While these arguments suggest universality also for the three-body parameter in heteronuclear systems that exhibit Efimov physics with only resonant interspecies two-body interactions, verifying this prediction is a high priority for future theory and experiment.

Equally important is the exploration of the relationship between $a < 0$ and $a > 0$ Efimov features — currently a subject of a number of controversies [6] — under the new perspective our present work offers.

Chapter 6

Efimov physics on the positive side

In the previous chapter, Efimov resonances of three-body recombination rates K_3 for $a < 0$ have been studied. The universal three-body parameter $a_{3b}^{-} \approx -9.73 r_{\rm vdW}$ is found to be consistent in recent experiments of ultracold atomic gases. Although through a very different mechanism, Efimov physics also affects the three-body recombination rates on the positive side ($a > 0$), which is the focus of this chapter. On the positive side, the three-body recombination rate shows a series of minima on top of an a^4 overall scaling. In principle, there are an infinite number of these minima a_k^+ that obey a universal relation $a_{k+1}^+/a_k^+ \approx 22.7$ for three identical bosons, a clear Efimov feature predicted by [102, 35]. The universality in the three-body parameter that was discussed in the preceding chapter implies that the position of the first minimum a_0^+ (and all other a_k^+) should also be universal, and this is confirmed by the numerical studies reported in the present chapter. The mechanism responsible for these minima is also studied. Reference [35] discovered that the mechanism causing these minima is a quantum interference phenomenon — the so called "Stückelberg minima". This mechanism is examined through an analysis of the partial recombination rates in all the final channels. In addition, two universal enhancements in three-body recombination are found around $a \approx 0.956\ r_{\rm vdW}$. These two enhancements are found to be associated with a universal d-wave dimer, crossing the three-body threshold, for systems with two-body van der Waals potentials .

In this chapter, the Lennard-Jones potential v_λ^a in Eq. (5.3) is adopted to study three-body recombination rates on the positive side. The three-body recombination rates are calculated for

systems having 2 or 3 s-wave bound states for a large range of scattering lengths. Figure 6.1 shows the recombination rates for the two cases (2 or 3 s-wave). The recombination rates for these two cases agree with each other very well. A Stückelberg minimum shows up at about $a \approx 28.09\ r_{\rm vdW}$ for both cases, suggesting that the three-body parameter is universal.

6.1 Stückelberg minima

The Stückelberg minima are the results of a destructive quantum interference phenomenon within the adiabatic hyperspherical picture discussed in Ref. [35]. Since the scattering length a is large and positive, the binding energy of the shallowest s-wave dimer $E_{\rm dimer} \approx -\hbar^2/\left(2\mu_{2b}a^2\right)$ is very small, forming a very shallow atom-dimer threshold in the three-body adiabatic potential curves. An avoided crossing between the three-body entrance channel and this shallow s-wave recombination channel occurs generally near $R \approx 3a$. Such a Landau-Zener-type avoided crossing usually implies a large coupling between the two channels and allows interference between two competing pathway, leading to Stückelberg minima. Since in view of the Hellman-Feynman theorem, the coupling strength is inversely proportional to the difference $U_i(R) - U_f(R)$ (here i and f denote the entrance and exit channels respectively) at some fixed R, the couplings are negligible for deeper channels. Therefore the Stückelberg minima can only be observed in the partial recombination rates into the shallowest s-wave channel. Comparing with the Efimov resonances on the negative side, the resonance behavior should show up in the partial recombination rates of every channel. Figure 6.2 shows the total and partial recombination rates near the Stückelberg minimum. This figure demonstrates that only the shallowest s-wave channel has a Stückelberg minimum.

6.2 Three-body recombination resonances associated with d-wave interactions

This section focuses on two enhancement features of the three-body recombination rates at about $a \approx 0.956\ r_{\rm vdW}$. They are found to be associated with a universal d-wave dimer that crosses the threshold at about the same scattering length. In 2000, Bo Gao predicted that for interactions

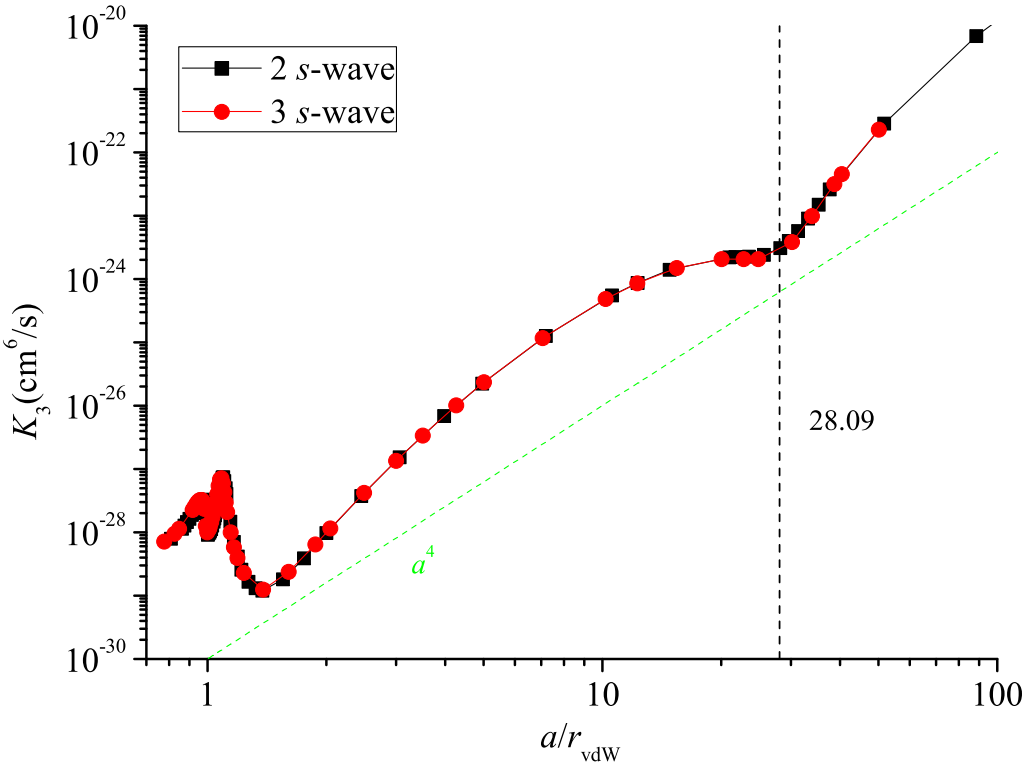

Figure 6.1: The three-body recombination rate K_3 as a function of scattering length a. The black curve with square symbols shows the results from a Lennard-Jones potential with two s-wave bound states; the red curve with circles illustrates the results for three s-wave bound states. A Stückelberg minimum appears at about $a = 28.09 r_{\mathrm{vdW}}$ for both cases; the minimum is indicated by a vertical dashed line. Two enhancement features are also shown for both cases near the small scattering length of $a \approx 0.956\ r_{\mathrm{vdW}}$. The green dashed line is proportional to a^4, the overall scaling of K_3.

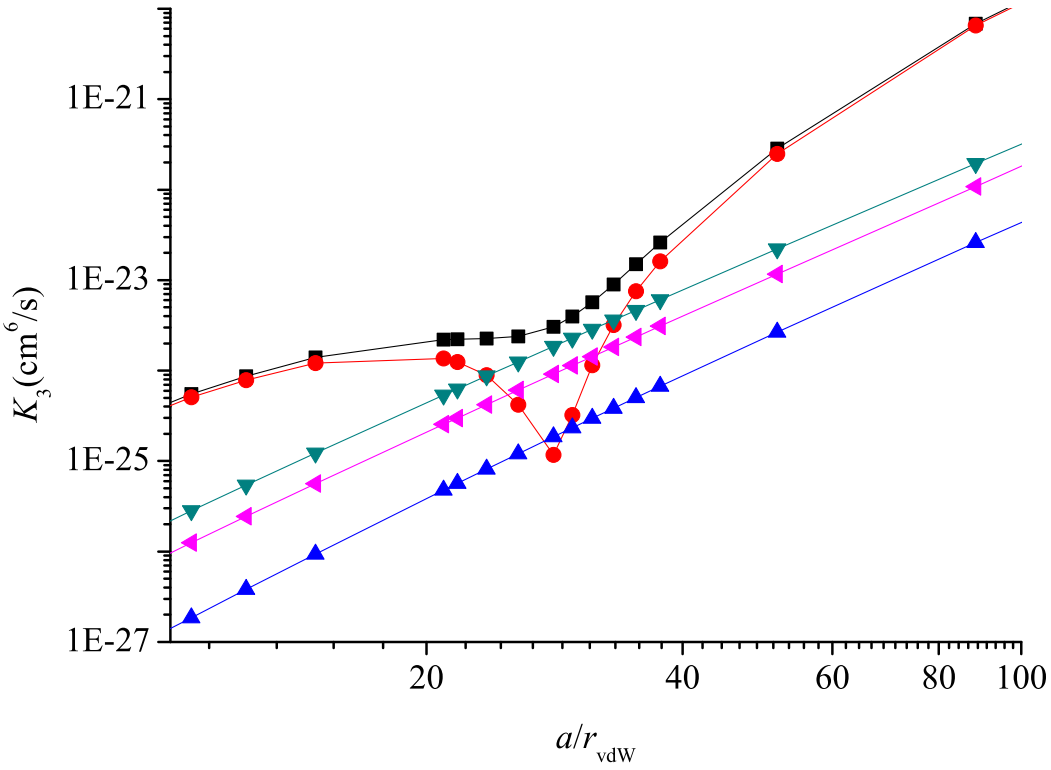

Figure 6.2: The total and partial three-body recombination rate K_3 as a function of scattering length a. The black curve with square symbols shows the total recombination rate, and the red curve with circle symbols shows the partial recombination rate for the shallowest s-wave dimer channel. The other curves shows the partial recombination rate for deeper atom-dimer channels. The Stückelberg minimum only shows up in the shallowest s-wave dimmer channel, but not the deeper atom-dimer channels.

with a van der Waals tail, $-C_6/r^6$, there is always a d-wave dimer (and dimers with higher angular momentum $l = 4j + 2$, where $j = 1, 2, 3...$) that becomes bound at a universal value of the s-wave scattering length $a = a^* = 4\pi/[\Gamma(1/4)]^2 r_{\rm vdW} \approx 0.956 r_{\rm vdW}$ [134]. The single-channel van der Waals interaction is a good model for studying a broad Fano-Feshbach resonance in an ultracold atomic gas that is open channel dominated [119]. We note that when $a = a^*$, the effective range $r_{\rm eff}$ has the value $2\,(3\pi)^{-1}\,[\Gamma\,(1/4)]^2\,r_{\rm vdW} \approx 2.789 r_{\rm vdW}$, which equals the effective range when the s-wave scattering length goes to infinity.

The universal two-body s-wave scattering length a_l^* (when a d-wave or i-wave dimer becomes bound) as a function of number of two-body s-wave bound states is studied numerically, using Lennard-Jones potentials for the two-body interaction. Figure 6.3 shows the scattering length when a d-wave (i-wave) dimer becomes bound. The more s-wave bound states, the deeper is the potential; The change in depth implies different short-range physics. The horizontal dashed line shows the universal prediction from Bo Gao's work [134]. The numerical results obtained for a_l^* ,where l denotes different partial wave, agree well with Bo Gao's prediction of two-body binding energies [within 1% (6%) in the case of 10 s-wave bound states for a d-wave (i-wave)]. The results show better and better agreement for a system with more and more s-wave bound states. In addition, just after the dimer becomes bound ($a \leq a_l^*$), the binding energy can be expressed as a linear function of the scattering length, i.e.,

$$E_l \approx \hbar^2 d_l \left(a_l^* - a\right) / (2\mu_{2b} r_{\rm vdW}^3), \tag{6.1}$$

where $d_2 \approx 5.6$ and $d_4 \approx 42$ are approximately universal for all d-waves and i-waves respectively.

To identify the mechanism of these three-body recombination enhancements, we focus on the example of Lennard-Jones potential with two s-wave bound states. In this numerical example, the d-wave dimers become bound at about $0.995 r_{\rm vdW}$ and the i-wave dimers become bound at about $1.206 r_{\rm vdW}$. Figure 6.4 shows the three-body adiabatic hyperspherical potential curves for the case of $a \approx 0.977 r_{\rm vdW}$ and the final recombination channels. A study of the partial recombination rates helps to discover the enhancement mechanism. Figure 6.5 shows the total recombination

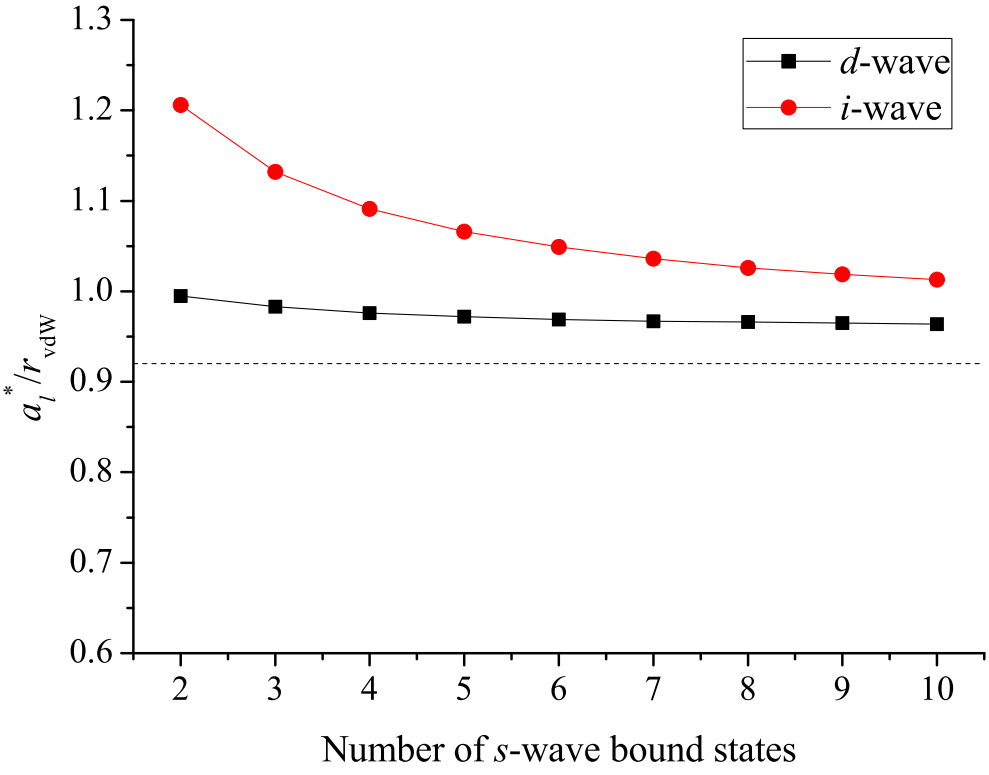

Figure 6.3: The two-body s-wave scattering length a_l^* when a d-wave ($l = 2$) dimer (black curve with square symbols) or an i-wave ($l = 6$) dimer becomes bound (red curve with circle symbols), shown as functions of the number of two-body s-wave bound states.

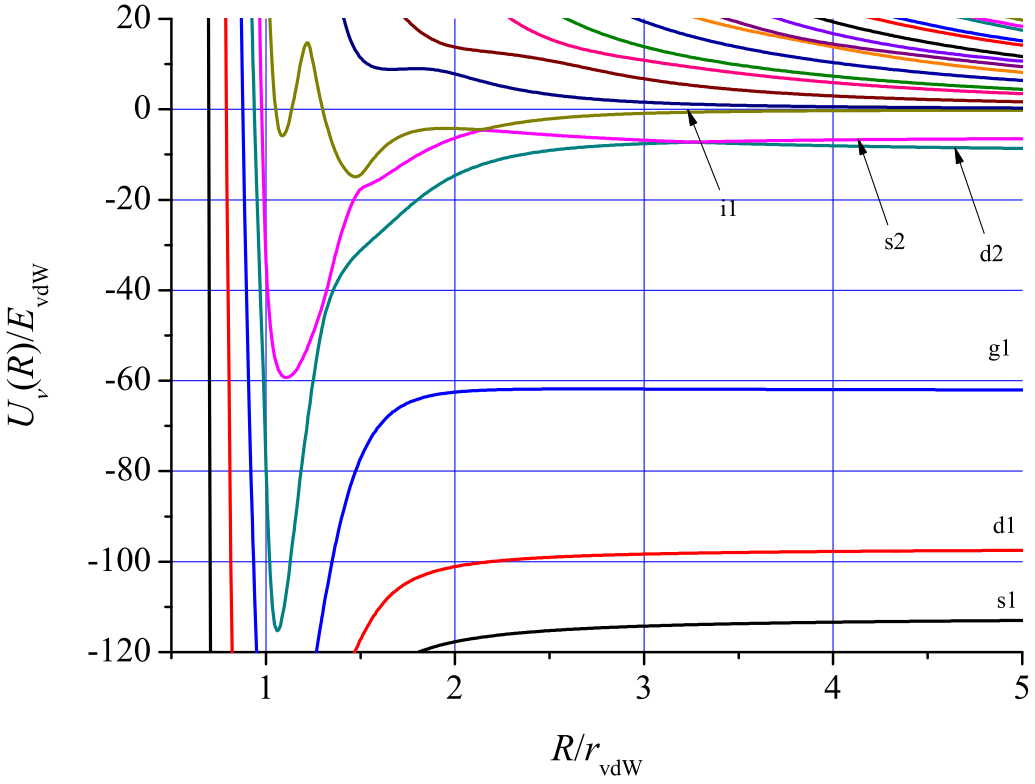

Figure 6.4: Adiabatic potential curves for $a \approx 0.977$. The $2+1$ channels, which corresponding to a dimer plus an atom at very large distance, are labeled by a combination of a letter and a number. The letter denotes the angular momentum quantum number of the dimer, and the number labels the channels for the same dimer angular momentum from low-to-high dimer energies.

rate (K_3) and the partial recombination rates (K_3^f) for every recombination channel f as functions of the scattering length a, near the appearance of a new d-wave dimer threshold. The three-body recombination rates show two enhancements with peaks A ($a_A \approx 1.09 r_{\rm vdW}$) and B ($a_B \approx 0.98 r_{\rm vdW}$). An enhancement around the peak A appears in all the partial three-body recombination rates right before the d-wave dimer becomes bound. After the d-wave becomes bound and forms a new threshold, the K_3 rate enhancement B is dominated by the partial rate in this new threshold, which is indicated in the inset of Fig. 6.5. These features suggest that the peak A might be a resonance due to that a three-body state crosses the three-body threshold, while the peak B seems to relate to some threshold behavior. The behavior of the effective potential curves near these enhancements gives qualitative insight into their origin.

Figure. 6.6 (I) shows the adiabatic hyperspherical potential curves at the resonance peak A. Only the channels relevant to the resonances are shown in this figure. The red dashed-line shows the effective hyperspherical potential. We have manually diabatized the potential near an avoid crossing (see Appendix E) that doesn't play an important role, and show it in the black solid curve. The black solid curve shows an outer barrier, and a three-body state can be supported for this potential. To check whether there is a three-body state near the threshold, a calculation of the WKB phase at zero scattering energy is carried out:

$$\phi_{\rm WKB} = \int_{R_a}^{R_b} \frac{\hbar}{\sqrt{-2\mu_{3b} W_{\nu\nu}(R)}} dR, \tag{6.2}$$

where R_a and R_b are the classical turning points shown in Fig. 6.6 (I). The calculated WKB phase $\phi_{\rm WKB}$ is about 0.51π, which is a strong evidence of the existence of a three-body state. It is this three-body state associated with the d-wave dimer state crossing the three-body break-up threshold that causes the three-body recombination resonances. The physical picture is that the three-body state at threshold can cause the system to be within the short-range potential valley for a long time, hence making it more likely that the system will decay into deeper channels. Figure. 6.6 (II) shows the effective potential $W_{\nu\nu}(R)$ as a function of R around the enhancement peak B. Three points (a), (b), and (c) in the inset of Fig. 6.6 are chosen for the study of the $W_{\nu\nu}$ corresponding to the

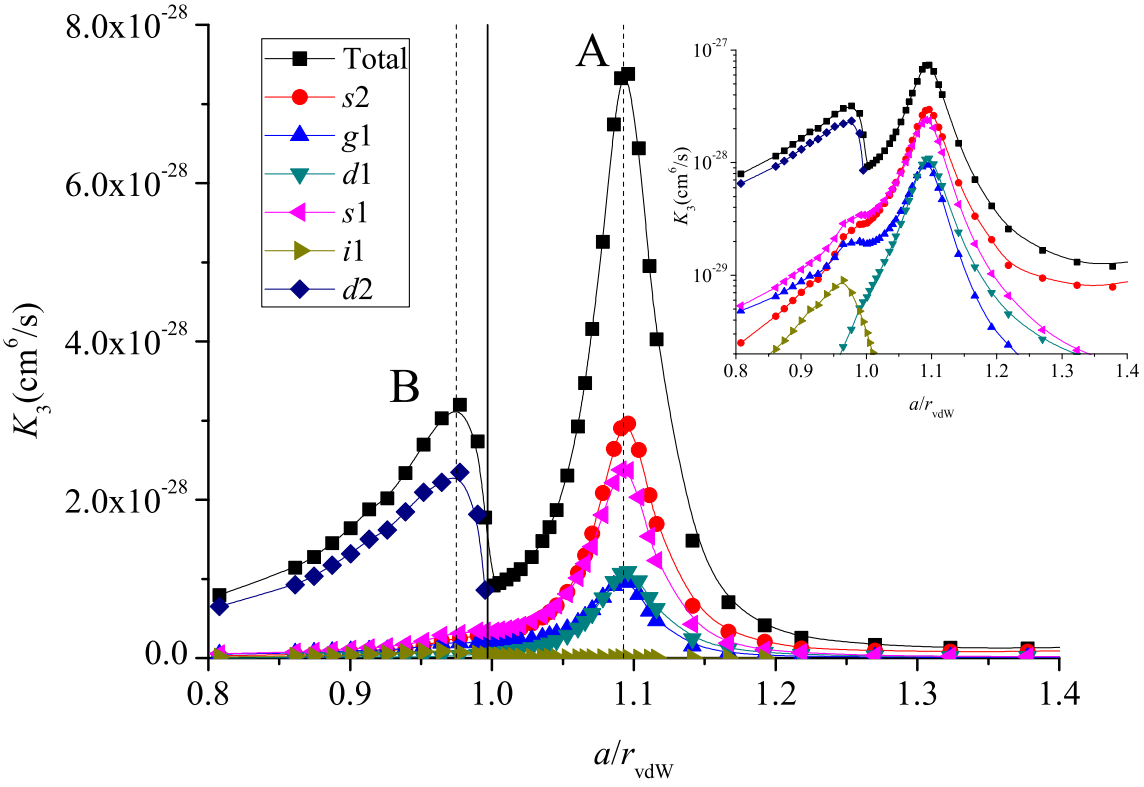

Figure 6.5: Total and partial three-body recombination rate as a function of two-body scattering length a, shown on a linear scale, near a d-wave dimer that is just becoming bound. The inset shows the same graph with a logarithmic scale for the y axis. The solid vertical line shows the s-wave scattering length when the d-wave dimer becomes bound. The two dashed vertical lines show the two peaks of recombination rate enhancement, denoted A and B respectively.

solid curves, dashed curves, and dash-dotted curves. For each point, the thin curve is the entrance channels that do not change much between the three points. The thick curve is the most important recombination channel: the new d-wave channel. It is clear that from point (a) to (c), the barrier and the threshold become lower and lower. When the maximum of the barrier is about to be lower than the three-body threshold, three-body recombination starts decreasing. This decrease may be due to the fact that when the maximum of the barrier is well above the three-body threshold, i.e., at point (a), the wave function of the exit channel has a large amplitude outside the barrier, and has a large overlap with the entrance channel wave function. When the maximum of the barrier becomes lower than the three-body break-up channel, i.e., at point (c), the wave function will have large amplitude inside the three-body potential valley and have much less overlap with the entrance channel wave function. The WKB phase calculated for these three-points is also not close to $\pi/2$ indicating that this enhancement is not due to a three-body state resonance. It is therefore not shown in the partial recombination rate for channels other than the newly formed d-wave.

6.3 Three-body state associated with the d-wave dimmer

While the Efimov states can be viewed as three-body states associated with an s-wave dimer near threshold, the new three-body state discovered in the previous section is a three-body state that can be associated with a d-wave dimer. Because of the existence of deeper atom-dimer thresholds, this three-body state is actually a quasi-bound state. Figure 6.7 shows the three-body quasi-bound state energy as a function of the scattering length a (red dots), with the error bars showing the widths of the quasi-bound states. The red line represents a fitting formula:

$$E_{3b}/\left[\hbar^2/\left(2\mu_{2b}r_{\rm vdW}^2\right)\right] = d_{3b}\left(a_{3b}^* - a\right)/r_{\rm vdW} + e_{3b}\left(a_{3b}^* - a\right)^2/r_{\rm vdW}^2, \tag{6.3}$$

where $a_{3b}^* \approx 1.09 r_{\rm vdW}$, $d_{3b} \approx 8.21$ and $e_{3b} \approx 10.01$. For comparison, the figure also shows the d-wave energy as the black curve with solid square symbols. The three-body energy crosses the threshold at $a \approx 1.09 r_{\rm vdW}$, which corresponds to peak A in K_3. Comparing with the d-wave dimer energy (the black curve with square symbols in Fig. 6.7), the three-body energy is shown to be always

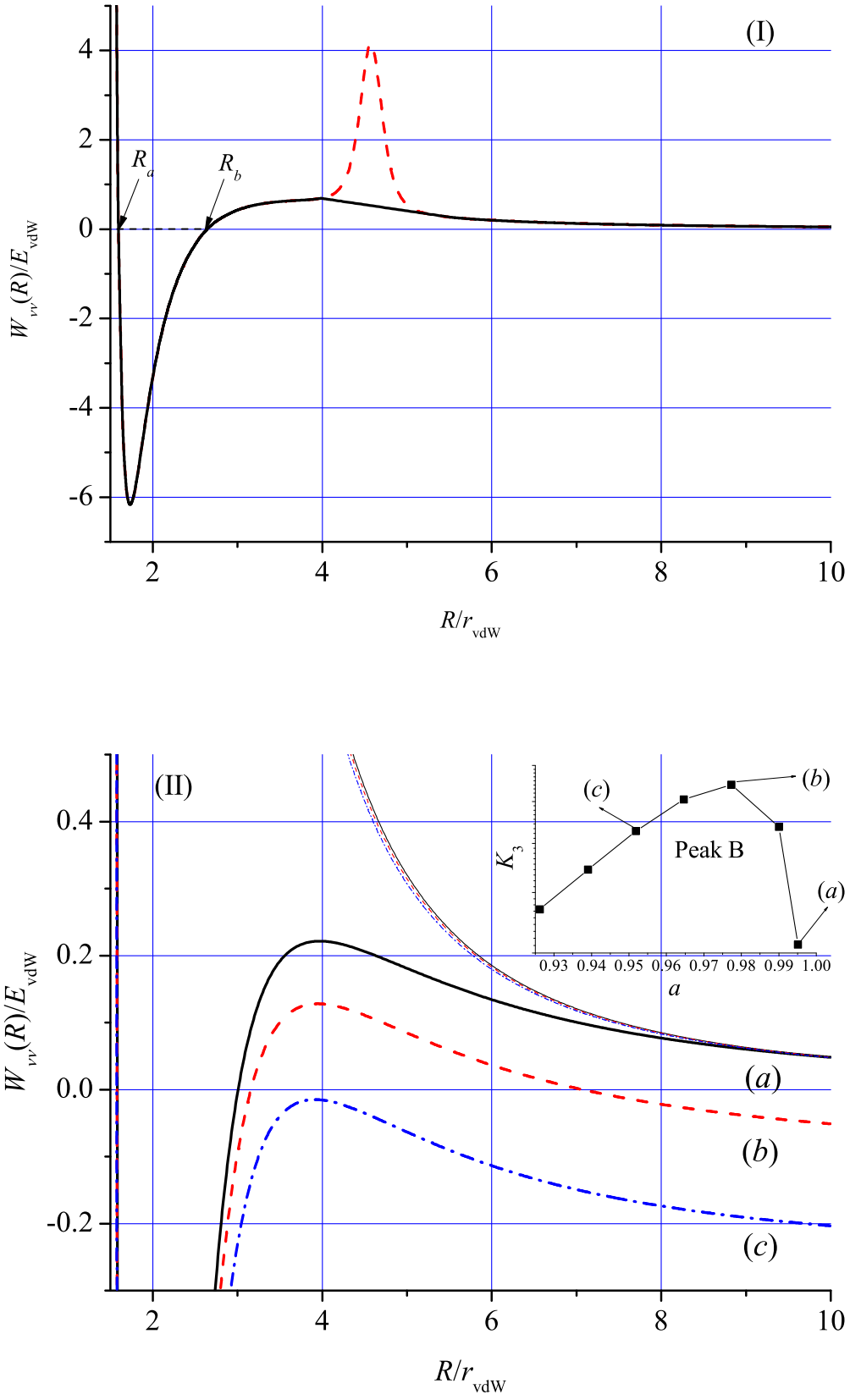

Figure 6.6: (I) $W_{\nu\nu}(R)$ as a function of hyperradius R at the K_3 resonance peak A. (II) $W(R)_{\nu\nu}$ as a function of hyperradius R around the K_3 enhancement peak B. The inset shows the three points where the potential curves correspond to.

deeper than the dimer energy. The difference between the dimer and trimer energy also increases when the scattering length becomes smaller, and the dimer becomes deeper. However, the width of the three-body quasi-bound state does not seem to change appreciably.

From Gao's analysis [134], it is known that there is also an i-wave dimer that becomes bound at a nearby scattering length. However, the i-wave dimer does not affect these two peaks. The i-wave channel has a very sharp avoided crossing with all the other channels. As a consequence, the partial K_3 rate is negligible as compared with the other partial rates. One explanation may be that forming an i-wave ($l = 6$) dimer results in the exchange of a large amount of angular momentum between the dimer and the additional atom. Therefore, although higher partial waves $l = 10, 14, 18...$ might also be formed at nearby scattering lengths, they are not expected to show any strong features in the three-body recombination rate.

Finally, Fig. 6.8 compares the three-body enhancements for the model potential of Lennard-Jones type, having either 2 or 3 s-wave bound states. The enhancement peaks of the two different models differ by only 0.01 $r_{\rm vdW}$. This agrees with a small observed shift of the scattering length where the d-wave dimer crosses the threshold. In this figure, the red (black) solid vertical line shows where the d-wave dimer crosses the threshold for LJ with 2 (3) s-waves. The red (black) dashed vertical line indicates where the three-body state associated with the d-wave cross the threshold for LJ with 2 (3) s-waves. This result suggests that the three-body state associated with the d-wave dimer is also universal.

6.4 Summary

In summary, we have calculated the three-body recombination rates for Lennard-Jones potential with 2 and 3 s-wave bound states at the positive side. A universal Stückelberg minimum for the two cases is found at around $a = 28.09\ r_{\rm vdW}$, and two universal enhancement peaks are found at about $a = 0.995\ r_{\rm vdW}$. In particular, one of the enhancement peaks is related with a universal three-body state that is associated with a d-wave dimer.

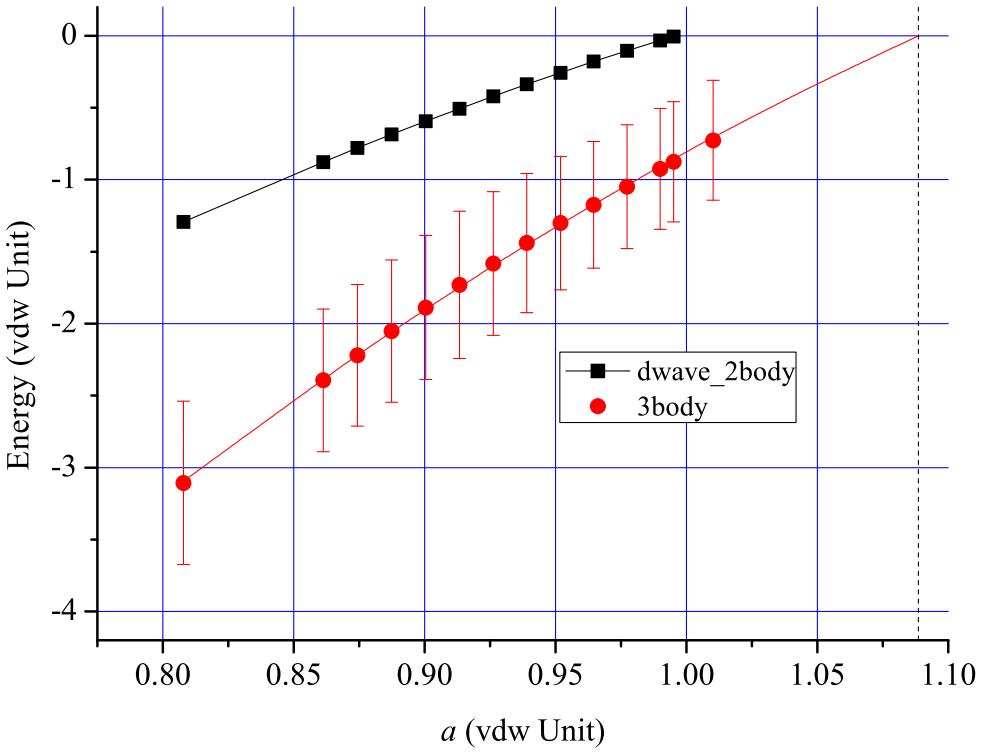

Figure 6.7: Energy of the three-body bound state associated with a d-wave dimer as a function of scattering length a.

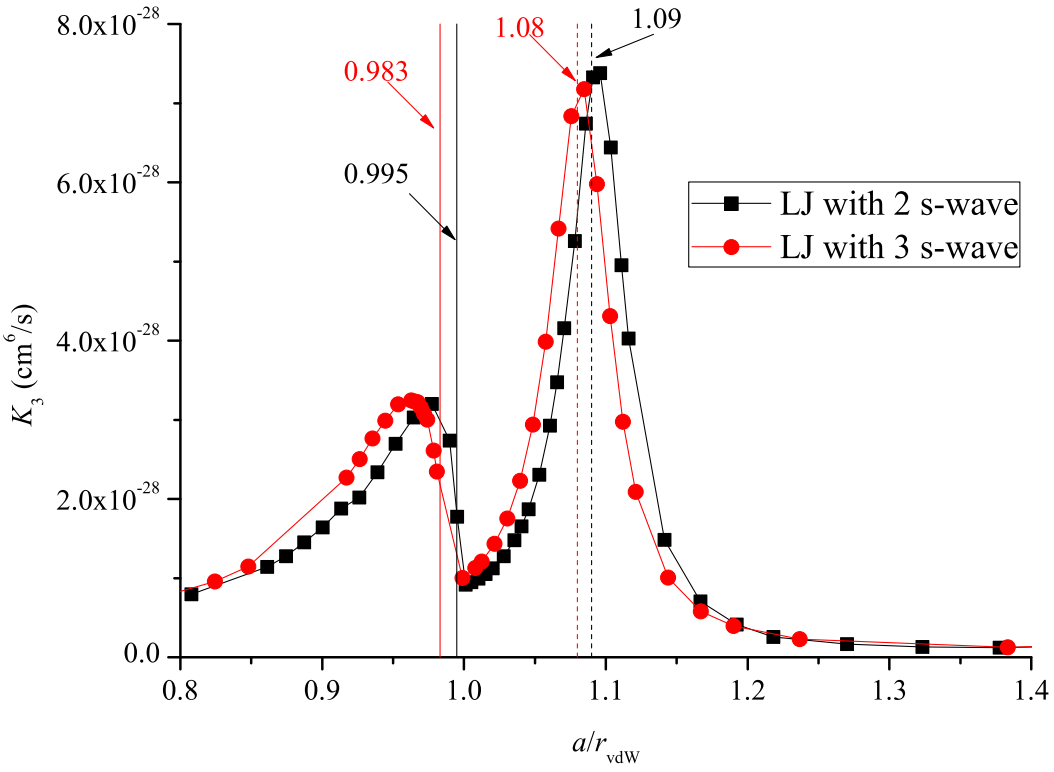

Figure 6.8: The enhancements for the total three-body recombination rate at about $a = 0.995 r_{\mathrm{vdW}}$ for Lennard-Jones potential with 2 and 3 s-wave bound states.

Bibliography

[1] C. M. Lindsay and B. J. McCall, J. Mol. Spectrosc. **210**, 60 (2001).

[2] I. Dabrowski and G. Herzberg, Can. J. Phys. **58**, 1238 (1980).

[3] G. Herzberg and J. K. G. Watson, Can. J. Phys. **58**, 1250 (1980).

[4] G. Herzberg, H. Lew, J. J. Sloan, and J. K. G. Watson, Can. J. Phys. **59**, 428 (1981).

[5] G. Herzberg, J. T. Hougen, and J. K. G. Watson, Can. J. Phys. **60**, 1261 (1982).

[6] C. Chin, R. Grimm, P. S. Julienne, and E. Tiesinga, Rev. Mod. Phys. **82**, 1225 (2010).

[7] M. Zaccanti, B. Deissler, C. D'Errico, M. Fattori, M. Jona-Lasinio, S. Müller, G. Roati, M. Inguscio, and G. Modugno, Phys. Rev. C **66**, 064001 (2002).

[8] S. E. Pollack, D. Dries, and R. G. Hulet, Science **326**, 1683 (2009).

[9] N. Gross, Z. Shotan, S. Kokkelmans, and L. Khaykovich, Phys. Rev. Lett. **103**, 163202 (2009).

[10] N. Gross, Z. Shotan, S. Kokkelmans, and L. Khaykovich, Phys. Rev. Lett. **105**, 103203 (2010).

[11] T. B. Ottenstein, T. Lompe, M. Kohnen, A. N. Wenz, and S. Jochim, Phys. Rev. Lett. **101**, 203202 (2008).

[12] T. Lompe, T. B. Ottenstein, F. Serwane, K. Viering, A. N. Wenz, G. Zürn, and S. Jochim, Phys. Rev. Lett. **105**, 103201 (2010).

[13] J. H. Huckans, J. R. Williams, E. L. Hazlett, R. W. Stites, and K. M. O'Hara, Phys. Rev. Lett. **102**, 165302 (2009).

[14] J. R. Williams, E. L. Hazlett, J. H. Huckans, R. W. Stites, Y. Zhang, and K. M. O'Hara, Phys. Rev. Lett. **103**, 130404 (2009).

[15] J. R. Wild, P. Makotyn, J. M. Pino, E. A. Cornell, and D. S. Jin, Phys. Rev. Lett. **108**, 145305 (2012).

[16] C. Chin, arxiv: , 1111.1484 (2011).

[17] I. Newton, Philosophiæ Naturalis Principia Mathematica, 1687.

[18] E. W. Brown, An Introductory Treatise on the Lunar Theory, Cambridge Universit Press, 1896.

[19] F. Haake, Quantum Signatures of Chaos, Edition: 2, Springer, 2001.

[20] K. Huang, C. N. Yang, and J. M. Luttinger, Phys. Rev. **105**, 776 (1957).

[21] M. H. Anderson, J. R. Ensher, M. R. Matthews, C. E. Wieman, and E. A. Cornell, Science **269**, 198 (1995).

[22] C. C. Bradley, C. A. Sacket, J. J. Tollett, and R. G. Hulet, Phys. Rev. Lett. **75**, 1687 (1995).

[23] K. B. Davis, M. R. Andrews, N. J. van Druten, D. S. Durfee, D. M. Kurn, and W. Ketterle, Phys. Rev. Lett. **75**, 3969 (1995).

[24] L. M. Delves, Nucl. Phys. **9**, 391 (1985).

[25] L. M. Delves, Nucl. Phys. **20**, 275 (1960).

[26] V. Efimov, Sov. J. Nucl. Phys. **12**, 589 (1971).

[27] J. Macek, J. Phys. B **1**, 831 (1968).

[28] U. Fano, Phys. Today **29**, 32 (1976).

[29] U. Fano, Rep. Prog. Phys. **46**, 97 (1983).

[30] C. W. Clark and C. H. Greene, Phys. Rev. A **21**, 1786 (1980).

[31] V. Kokoouline and C. H. Greene, Phys. Rev. A **68**, 012703 (2003).

[32] N. P. Mehta, S. T. Rittenhouse, J. P. D'Incao, J. von Stecher, and C. H. Greene, Phys. Rev. Lett. **103**, 153201 (2009).

[33] L. H. Thomas, Phys. Rev. **47**, 903 (1935).

[34] T. Kraemer, M. Mark, P. Waldburger, J. G. Danzl, C. Chin, B. Engeser, A. D. Lange, K. Pilch, A. Jaakkola, H.-C. Nägerl, and R. Grimm, Nature **440**, 315 (2006).

[35] B. D. Esry, C. H. Greene, and J. P. Burke, Phys. Rev. Lett. **83**, 1751 (1999).

[36] B. D. Esry and C. H. Greene, Nature **440**, 289 (2006).

[37] E. Herbst and W. Klemperer, Astrophys. J. **185**, 505 (1973).

[38] W. D. Watson, Astrophys. J. **183**, L17 (1973).

[39] L. Trafton, D. F. Lester, and K. L. Thompson, Astrophys. J. **343**, L73 (1989).

[40] J. E. P. Connerney, R. Baron, T. Satoh, and T. Owen, Science **262**, 1035 (1993).

[41] J. J. Thomson, Philos. Mag. **21**, 225 (1911).

[42] T. Oka, Phys. Rev. Lett. **45**, 531 (1980).

[43] B. J. McCall, A. J. Huneycutt, R. J. Saykally, T. R. Geballe, N. Djuric, G. H. Dunn, J. Semaniak, O. Novotny, A. Al-Khalili, A. Ehlerding, F. Hellberg, S. Kalhori, A. Neau, R. Thomas, F. Osterdahl, and M. Larsson, Nature **422**, 500 (2003).

[44] A. J. Huneycutt, Studies of Atmospheric and Interstellar Molecules Using Cavity Ringdown Spectroscopy, PhD thesis, University of California, Berkeley, 2003.

[45] R. J. Saykally, E. A. Michael, J. Wang, and C. H. Greene, J. Chem. Phys. **133**, 234302 (2010).

[46] J. G. Frey and B. J. Howard, Chem. Phys. **99**, 415 (1985).

[47] H. Suno, B. D. Esry, C. H. Greene, and J. P. Burke, Phys. Rev. A **65**, 042725 (2002).

[48] R. C. Whitten and F. T. Smith, J. Math. Phys. **9**, 1103 (1968).

[49] B. R. Johnson, J. Chem. Phys. **73**, 5051 (1980).

[50] B. Lepetit, Z. Peng, , and A. Kuppermann, Chem. Phys. Lett. **166**, 572 (1990).

[51] B. K. Kendrick, R. T. Pack, R. B. Walker, and E. F. Hayes, J. Chem. Phys. **110**, 6673 (1999).

[52] B. K. Kendrick, R. T. Pack, R. B. Walker, and E. F. Hayes, J. Chem. Phys. **110**, 6673 (1999).

[53] M. Aymar, C. H. Greene, and E. Luc-Koenig, Rev. Mod. Phys. **68**, 1015 (1996).

[54] J. P. Burke, Theoretical investigation of cold alkali atom collisions, PhD thesis, University of Colorado at Boulder, 1999.

[55] E. Nielsen, D. V. Fedorov, A. S. Jensen, and E. Garrido, Phys. Rep. **347**, 373 (2001).

[56] R. B. Nelson, AIAA Journal **14**, 1201 (1976).

[57] E. Anderson, Z. Bai, C. Bischof, J. Demmel, J. Dongarra, J. D. Cros, A. Greenbaum, S. Hammerling, A. Mckenney, S. Ostouchov, and D. Sorensen, LAPACK Users Guide, SIAM, 1992.

[58] U. Naumanm and O. Schenk, Combniatorial Scientific Computing, Champman and Hall, 2012.

[59] J. V. Lill, G. A. Parker, and J. C. Light, Chem. Phys. Lett. **89**, 483 (1982).

[60] T. N. Rescigno and C. W. McCurdy, Phys. Rev. A **62**, 032706 (2000).

[61] D. E. Manolopoulos and R. E. Wyatt, Chem. Phys. Lett. **152**, 23 (1998).

[62] K. L. Baluja and P. G. Burke, Comp. Phys. Comm. **27**, 299 (1982).

[63] J. Wang and C. H. Greene, Phys. Rev. A **82**, 022506 (2010).

[64] H. Helm, Phys. Rev. Lett. **56**, 42 (1986).

[65] H. Helm, Phys. Rev. A **38**, 3425 (1988).

[66] A. E. Orel, I. F. Schneider, and A. Suzor-Weiner, Philos. Trans. R. Soc. London, Ser. A **385**, 2445 (2000).

[67] V. Kokoouline, C. Greene, and B. Esry, Nature (London) **412**, 891 (2001).

[68] C. Jungen and S. T. Pratt, Phys. Rev. Lett. **102**, 023201 (2009).

[69] M. Vervloet and J. K. G. Watson, J. Mol. Spectrosc. **217**, 255 (2003).

[70] M. J. Seaton, Rep. Prog. Phys. **46**, 167 (1983).

[71] C. H. Greene and C. Jungen, Adv. At. Mol. Phys. **21**, 51 (1985).

[72] H. Takagi, J. Phys. B **26**, 4815 (1993).

[73] O. Motapon, F. O. W. Tamo, X. Urbain, and I. F. Schneider, Phys. Rev. A **77**, 052711 (2008).

[74] A. Giusti, J. Phys. B **13**, 386 (1980).

[75] O. I. Tolstikhin, S. Watanabe, and M. Matsuzawa, J. Phys. B: At. Mol. Opt. Phys. **29**, L389 (1996).

[76] S. F. Santos, V. Kokoouline, and C. H. Greene, J. Chem. Phys. **127**, 124309 (2007).

[77] W. Cencek, J. Rychlewski, R. Jaquet, and W. Kutzelnigg, J. Chem. Phys. **108**, 2831 (1998).

[78] R. Jaquet, W. Cencek, W. Kutzelnigg, and J. Rychlewski, J. Chem. Phys. **108**, 2837 (1998).

[79] M. Pavanello, L. Adamowicz, A. Alijah, N. F. Zobov, I. I. Mizus, O. L. Polyansky, J. Tennyson, T. Szidarovszky, A. G. Császár, M. Berg, A. Petrignani, and A. Wolf, Phys. Rev. Lett. **108**, 023002 (2012).

[80] I. Mistrík, R. Reichle, U. Müller, H. Helm, M. Jungen, and J. A. Stephens, Phys. Rev. A **61**, 033410 (2000).

[81] A. Staib and W. Domcke, Z. Phys. D: At., Mol. Clusters **16**, 275 (1990).

[82] E. E. Eyler and F. M. Pipkin, Phys. Rev. A **27**, 2462 (1983).

[83] G. Herzberg and C. Jungen, J. Chem. Phys. **77**, 5876 (1982).

[84] C. Jungen, I. Dabrowski, G. Herzberg, and D. J. W. Kendall, J. Chem. Phys. **91**, 3926 (1989).

[85] N. R. Badnell and M. J. Seaton, J. Phys. B. **32**, 3955 (1999).

[86] J. D. Augspurger and C. E. Dykstra, J. Chem. Phys. **88**, 3817 (1988).

[87] J. D. Augspurger and C. E. Dykstra, J. Chem. Phys. **91**, 1384 (1989).

[88] A. Fridman, Plasma Chemistry, Cambridge University Press, Cambridge, 2008.

[89] J. Glosík, O. Novotný, A. Pysanenko, P. Zakouril, R. Plašil, P. Kudrna, and V. Poterya, Plasma Sources Sci. Technol. **12**, S117 (2003).

[90] V. Kokoouline and C. H. Greene, Phys. Rev. A **69**, 032711 (2004).

[91] J. A. Stephens and C. H. Greene, J. Chem. Phys. **102**, 1579 (1995).

[92] G. Herzberg, Annu. Rev. Phys. Chem. **38**, 27 (1987).

[93] J. Glosík, I. Korolov, R. Plasil, O. Novotny, T. Kotrik, P. Hlavenka, J. Varju, I. A. Mikhailov, V. Kokoouline, and C. H. Greene, J. Phys. B – At. Mol. Opt. **41**, 191001 (2008).

[94] D. R. Bates and S. P. Khare, Proc. Phys. Soc. , 231 (1965).

[95] J. Wang, J. P. D'Incao, and C. H. Greene, Phys. Rev. A **84**, 052721 (2011).

[96] J. Cubizolles, S. J. J. M. F. K. T. Bourdel, G. V. Shlyapnikov, and C. Salomon, Phys. Rev. Lett. **91**, 240401 (2003).

[97] S. Jochim, M. Bartenstein, A. Altmeyer, G. Hendl, C. Chin, J. H. Denschlag, and R. Grimm, Phys. Rev. Lett. **91**, 240402 (2003).

[98] M. W. Zwierlein, C. A. Stan, C. H. Schunck, S. M. F. Raupach, Z. H. S. Gupta, and W. Ketterle, Phys. Rev. Lett. **91**, 250401 (2003).

[99] J. P. D'Incao and B. D. Esry, Phys. Rev. Lett. **100**, 163201 (2008).

[100] B. Borca, J. W. Dunn, V. Kokoouline, and C. H. Greene, Phys. Rev. Lett. **91**, 070404 (2003).

[101] T. Weber, J. Herbig, and H.-C. N. M. Mark, Phys. Rev. Lett. **91**, 123201 (2003).

[102] E. Nielsen and J. H. Macek, Phys. Rev. Lett. **83**, 1566 (1999).

[103] J. P. D'Incao and B. D. Esry, Phys. Rev. Lett. **94**, 213201 (2005).

[104] E. Braaten and H.-W. Hammer, Phys. Rep. **428**, 259 (2006).

[105] J. P. D'Incao and B. D. Esry, Phys. Rev. Lett. **103**, 083202 (2009).

[106] F. Ferlaino and R. Grimm, Physics **3**, 9 (2010).

[107] H. Suno and B. D. Esry, Phys. Rev. A **78**, 062701 (2008).

[108] H. Suno and B. D. Esry, Phys. Rev. A **80**, 062702 (2009).

[109] Y. Wang, J. P. D'Incao, and B. D. Esry, Phys. Rev. A **83**, 032703 (2011).

[110] H. Suno, J. Chem. Phys. **134**, 064318 (2011).

[111] G. A. Parker, R. B. Walker, B. K. Kendrick, and R. T. Pack, J. Chem. Phys. **117**, 6083 (2002).

[112] F. D. Colavecchia, F. Mrugala, G. A. Parker, and R. T. Pack, J. Chem. Phys. **118**, 10387 (2003).

[113] B. D. Esry, C. H. Greene, and H. Suno, Phys. Rev. A **65**, 010705 (2001).

[114] E. B. S. G. C. Maitland, M. Rigby and W. A. Wakeham, Intermolecular Forces, Clarendon Press, Oxford, 1981.

[115] J. Wang, J. P. D'Incao, B. D. Esry, and C. H. Greene, Phys. Rev. Lett. **108**, 263001 (2012).

[116] P. Soldán, M. T. Cvitas, and J. M. Hutson, Phys. Rev. A **67**, 054702 (2003).

[117] E. Epelbaum, A. Nogga, W. Glöckle, H. Kamada, U.-G. Meißner, and H. Witała, Phys. Rev. C **66**, 064001 (2002).

[118] J. P. D'Incao, C. H. Greene, , and B. D. Esry, J. Phys. B **42**, 044016 (2009).

[119] C. Chin, R. Grimm, P. S. Julienne, and E. Tiesinga, Rev. Mod. Phys. **82**, 1225 (2010).

[120] V. V. Flambaum, G. F. Gribakin, and C. Harabati, Phys. Rev. A **59**, 1998 (1993).

[121] G. F. Gribakin and V. V. Flambaum, Phys. Rev. A **48**, 546 (1993).

[122] R. Côté, H. Friedrich, and J. Trost, Phys. Rev. A **56**, 1781 (1997).

[123] Y. Wang, J. P. D'Incao, , and C. H. Greene, Phys. Rev. Lett. **106**, 233201 (2011).

[124] D. S. Petrov, Phys. Rev. Lett. **93**, 143201 (2004).

[125] P. Massignan and H. T. C. Stoof, Phys. Rev. Lett. **93**, 143201 (2004).

[126] Y. Wang, J. P. D'Incao, , and B. D. Esry, Phys. Rev. A **83**, 042710 (2011).

[127] P. Naidon and M. Ueda, Comptes Rendus Physique **12**, 13 (2011).

[128] P. Naidon, E. Hiyama, and M. Ueda, arxiv , 1109.5807.

[129] S. Nakajima, M. Horikoshi, T. Mukaiyama, P. Naidon, and M. Ueda, Phys. Rev. Lett. **106**, 143201 (2011).

[130] M. D. Lee, T. Köhler, and P. S. Julienne, Phys. Rev. A **76**, 012720 (2007).

[131] M. Jona-Lasinio and L. Pricoupenko, Phys. Rev. Lett. **104**, 023201 (2010).

[132] D. Blume, C. H. Greene, and B. D. Esry, J. Chem. Phys. **113**, 2145 (2000).

[133] S. T. Rittenhouse, N. P. Mehta, and C. H. Greene, Phys. Rev. A **82**, 022706 (2010).

[134] B. Gao, Phys. Rev. A **62**, 050702(R) (2000).

[135] D. A. Varshalovich, A. N. Moskalev, and V. K. Khersonskii, Quantum Theory of Angular Momentum, World Scientific, singapore, 1988.

[136] H. C. Longuet-Higgins, Advances in Spectroscopy, Interscience, New York, 1961.

[137] N. Gemelke, C.-L. Hung, X. Zhang, and C. Chin, arxiv: , 0812.1317 (2008).

Appendix A

Symmetry of R-matrix

The R-matrix $\underline{\mathcal{R}}$ is a real and symmetric matrix. This symmetry is determined by the properties of the radial Schrödinger equation [Eq. (2.17)], which can be rewritten as

$$\frac{d^2}{dR^2}\underline{F} = \left[\frac{2\mu_{3b}}{\hbar^2}\left(\underline{U} - E\underline{1}\right) - \underline{Q}\right]\underline{F} - 2\underline{P}\frac{d}{dR}\underline{F}, \tag{A.1}$$

where $\underline{1}$ denotes an identity matrix. Inserting the expansion of the wave function [Eq. (2.16)] into Eq. (2.20) gives

$$\underline{\widetilde{F}} = \frac{d}{dR}\underline{F} + \underline{P} \times \underline{F}. \tag{A.2}$$

The definition of the R-matrix can then expressed as,

$$\underline{\mathcal{R}}\left(\frac{d}{dR}\underline{F} + \underline{P} \times \underline{F}\right) = \underline{F}. \tag{A.3}$$

Taking derivatives of both sides of this equation leads to

$$\left(\frac{d}{dR}\underline{\mathcal{R}}\right)\left(\frac{d}{dR}\underline{F} + \underline{P} \times \underline{F}\right) + \underline{\mathcal{R}}\left[\frac{d^2}{dR^2}\underline{F} + \left(\frac{d}{dR}\underline{P}\right)\underline{F} + \underline{P}\left(\frac{d}{dR}\underline{F}\right)\right] = \frac{d}{dR}\underline{F}. \tag{A.4}$$

Replacing the second derivative of $\underline{F}$ by Eq. (A.1) gives us

$$\left(\frac{d}{dR}\underline{\mathcal{R}}\right)\left(\frac{d}{dR}\underline{F} + \underline{P} \times \underline{F}\right) + \underline{\mathcal{R}}\left[\frac{2\mu_{3b}}{\hbar^2}\left(\underline{U} - E\underline{1}\right) - \underline{P^2}\right]\underline{F} = \left(\underline{\mathcal{R}} \times \underline{P} + \underline{1}\right)\frac{d}{dR}\underline{F}, \tag{A.5}$$

with the help of the relation $\frac{d}{dR}\underline{P} = -\underline{P^2} + \underline{Q}$. Finally, after multiplying both sides of Eq. (A.5) with $\left[\left(\frac{d}{dR}\underline{F} + \underline{P} \times \underline{F}\right)\right]^{-1}$ and using the definition of the R-matrix Eq. (A.3), we arrive at

$$\begin{aligned}
\frac{d}{dR}\underline{\mathcal{R}} &= -\underline{\mathcal{R}}\left[\frac{2\mu_{3b}}{\hbar^2}\left(\underline{U} - E\underline{1}\right) - \underline{P^2}\right]\underline{\mathcal{R}} + \left(\underline{\mathcal{R}} \times \underline{P} + \underline{1}\right)\left(\frac{d}{dR}\underline{F}\right)\left(\frac{d}{dR}\underline{F} + \underline{P} \times \underline{F}\right)^{-1} \\
&= -\underline{\mathcal{R}}\left[\frac{2\mu_{3b}}{\hbar^2}\left(\underline{U} - E\underline{1}\right) - \underline{P^2}\right]\underline{\mathcal{R}} + \left(\underline{\mathcal{R}} \times \underline{P} + \underline{1}\right)\left(\underline{1} - \underline{P} \times \underline{\mathcal{R}}\right).
\end{aligned} \tag{A.6}$$

Since $\underline{P}$ is antisymmetric and $\underline{P^2}$ is symmetric, this equation implies that the symmetry of the matrix $\underline{\mathcal{R}}$ at one value of R immediately guarantees symmetry at all R values. In most problems, the matrix $\underline{\mathcal{R}}$ is diagonal in some region of space, often at small distances ($R \to 0$), which is enough to prove that it will remain real and symmetric at all hyperradii.

The symmetry of $\underline{\mathcal{R}}$ guarantees the symmetry of the reaction matrix $\underline{\mathcal{K}}$ and the unity of scattering matrix $\underline{\mathcal{S}}$. In the asymptomatic region at large hyperradii, the $\underline{P}$ matrix vanishes. The relation between $\underline{\mathcal{R}}$ and $\underline{\mathcal{K}}$ is given by,

$$\underline{\mathcal{R}}\left[\underline{f}' - \underline{g}'\underline{\mathcal{K}}\right] = \left[\underline{f} - \underline{g}\underline{\mathcal{K}}\right] \tag{A.7}$$

or equivalently by

$$\left[\underline{f}' - \underline{g}'\underline{\mathcal{K}}\right] = \underline{\mathcal{R}}^{-1}\left[\underline{f} - \underline{g}\underline{\mathcal{K}}\right]. \tag{A.8}$$

Transposing on both sides of Eq.(A.7) gives

$$\left[\underline{f} - \underline{\mathcal{K}}^T\underline{g}\right] = \left[\underline{f}' - \underline{\mathcal{K}}^T\underline{g}'\right]\underline{\mathcal{R}}. \tag{A.9}$$

Together, Eqs. (A.8) and Eq. (A.9) give the followings

$$\left[\underline{f} - \underline{\mathcal{K}}^T\underline{g}\right]\left[\underline{f}' - \underline{g}'\underline{\mathcal{K}}\right] = \left[\underline{f}' - \underline{\mathcal{K}}^T\underline{g}'\right]\left[\underline{f} - \underline{g}\underline{\mathcal{K}}\right], \tag{A.10}$$

which can be transformed into

$$\underline{\mathcal{K}}^T\left(\frac{d\underline{g}}{dR}\underline{f} - \underline{g}\frac{d\underline{f}}{dR}\right) = \left(\underline{g}\frac{d\underline{f}}{dR} - \frac{d\underline{g}}{dR}\underline{f}\right)\underline{\mathcal{K}}. \tag{A.11}$$

Since $\underline{f}$ and $\underline{g}$ are linearly independent solutions of the Schrödinger equation, their Wronskian has the good property of

$$\frac{d\underline{g}}{dR}\underline{f} - \underline{g}\frac{d\underline{f}}{dR} = \underline{f}\frac{d\underline{g}}{dR} - \frac{d\underline{f}}{dR}\underline{g} = \frac{2\mu_{3b}}{\hbar\pi}\underline{1}, \tag{A.12}$$

whoich guarantees that $\underline{\mathcal{K}}^T = \underline{\mathcal{K}}$. Therefore, we prove that $\underline{\mathcal{K}}$ is real and symmetric, and consequently, $\underline{\mathcal{S}} = \left(\underline{1} + i\underline{\mathcal{K}}\right)\left(\underline{1} - i\underline{\mathcal{K}}\right)^{-1}$ is unitary.

Appendix B

R-matrix propagation method with the traditional adiabatic method.

The model described in the main text uses the traditional adiabatic approach combined with an R-matrix propagation method for large values of R, where the $\underline{P}$ and $\underline{Q}$ matrices are smooth functions of R. One advantage of using this representation is that instead of calculating the values of the $\underline{P}$ and $\underline{Q}$ matrices at every mesh point in R, we can solve the hyperangular part of the Hamiltonian at relatively fewer grid points. (The number of grid points is generally set by the characteristic wavelength associated with the collision energy.) This strategy, therefore, allows the use of interpolation and/or extrapolation methods to generate the required much denser grid without memory storage problems. Appendix B describes the approach in more detail.

In the traditional method, $\psi_{\nu'}$ is expanded as

$$\psi_{\nu'}(R) = \sum_{j\nu} c_{j\nu,\nu'} \pi_j(R) \Phi_\nu(R;\Omega). \tag{B.1}$$

A comparison of Eq. (B.1) with Eq. (2.52) shows that the main differences between the traditional adiabatic method and the SVD method derive from using different three-body numerical basis sets. (Notice that in Eq. (B.1), the $\Phi_\nu(R;\Omega)$ are channel functions evaluated at R, while in Eq. (2.52), the $\Phi_\nu(R_j;\Omega)$ are channel functions evaluated at R_j.) However, one can show that the expansion coefficients $c_{j\nu,\nu'}$ are the same for the two expansions if $\Phi_\nu(R;\Omega)$ is smooth so that the DVR approximation can be applied,

$$\int dR \pi_i(R) \Phi_\nu(R;\Omega) \pi_j(R) \approx \Phi_\nu(R_i;\Omega) \delta_{ij}. \tag{B.2}$$

Equation (B.2) implies that the traditional adiabatic method and the SVD method are equivalent within the DVR approximation. Therefore, when the $\underline{P}$ and $\underline{Q}$ matrices change rapidly and are hard to evaluate numerically, it is highly advantageous to choose the SVD method; when the $\underline{P}$ and $\underline{Q}$ matrices are smooth, however, the traditional method is simpler and benefits from lower memory storage requirements.

Next, the details of the traditional approach are elaborated and the R-matrix propagation from a point b_1 to another point b_2 is explained. Insertion of Eq. (B.1) into Eq. (2.19) yields

$$\begin{aligned} F_{\nu\nu'}(b_1) &= \sum_j c_{j\nu,\nu'}\pi_j(b_1), \qquad \text{(B.3)} \\ F_{\nu\nu'}(b_2) &= \sum_j c_{j\nu,\nu'}\pi_j(b_2), \\ \widetilde{F}_{\nu\nu'}(b_1) &= \sum_\mu \left[\delta_{\nu\mu}F'_{\mu\nu'}(b_1) + P_{\nu\mu}(b_1)F_{\mu\nu'}(b_1)\right], \\ \widetilde{F}_{\nu\nu'}(b_2) &= \sum_\mu \left[\delta_{\nu\mu}F'_{\mu\nu'}(b_2) + P_{\nu\mu}(b_2)F_{\mu\nu'}(b_2)\right]. \end{aligned}$$

As the next step, rewrite Eq. (2.11) in the basis of Eq. (B.1) in the matrix form of Eq. (2.59), with the matrix elements

$$\begin{aligned} H_{i\mu,j\nu} &= \frac{1}{2\mu_{3b}}\int_{b_1}^{b_2}\pi_i'(R)\,\pi_j'(R)\,dR\delta_{\mu\nu} + \left[U_\nu(R_j)\,\delta_{\mu\nu} - \frac{P_{\mu\nu}^2(R_j)}{2\mu_{3b}}\right]\delta_{ij} \\ &\quad -\frac{1}{2\mu_{3b}}\int_{b_1}^{b_2}\pi_i(R)\,P_{\mu\nu}(R)\,\pi_j'(R) - \pi_i'(R)\,P_{\nu\mu}(R)\,\pi_j(R)\,dR, \qquad \text{(B.4)} \\ L_{i\mu,j\nu} &= \frac{1}{2\mu_{3b}}\left[\pi_i(R)\,\delta_{\mu\nu}\pi_j'(R) + \pi_i(R)\,P_{\mu\nu}(R)\,\pi_j(R)\right]\Big|_{b_1}^{b_2}. \qquad \text{(B.5)} \end{aligned}$$

Use of these matrix elements and replacing $a1(a2)$ with $b1(b2)$, the same procedure as Eqs. (2.63-2.73) accomplishes the matrix propagation.

Appendix C

Permutation symmetry of the basis functions

For convenience, we first consider trial basis functions as

$$\Phi_{\rm try} = e^{im_2\varphi}\mathcal{R}^{N^+}_{K^+m^+}(\alpha,\beta,\gamma)\,\Phi^I_{g_I}u_j(\theta)\,, \tag{C.1}$$

and use them to construct basis functions with proper permutation symmetry Eqs.(3.5–3.6). The continuity condition for Smith-Whitten hyperspherical coordinates [52, 47] requires that,

$$\Phi_{\rm try}(\theta,\varphi,\alpha,\beta,\gamma) = \Phi_{\rm try}(\theta,\varphi+2\pi,\alpha,\beta,\gamma+\pi)\,. \tag{C.2}$$

This boundary condition leads to the condition that $K^+/2+m_2$ must be integral. Hence, if K^+ is even, m_2 must be integral; if K^+ is odd, m_2 must be half integral. We remark here that the parity Π^+ is determined by K^+ only; $\Pi^+=+1$, if K^+ is even, and $\Pi^+=-1$, if K^+ is odd [52, 47].

The permutation symmetries for the basis functions chosen for each degree of freedom are shown in Table 4. Here, $\Phi^I_{g_I}$ is the nuclear-spin basis function defined as in Ref. [31]. g_I equals zero for the ortho state, and ±1 for the para state. The rotational part $\mathcal{R}^{N^+}_{K^+m^+}(\alpha,\beta,\gamma)$ is given by,

$$\mathcal{R}^{N^+}_{K^+m^+}(\alpha,\beta,\gamma) = \sqrt{\frac{2N^++1}{8\pi^2}}\left[D^{N^+}_{m^+K^+}(\alpha,\beta,\gamma)\right]^* \tag{C.3}$$

where $D^{N^+}_{m^+K^+}$ are the Wigner D functions of the Euler angles. The phase of the Wigner function is chosen as in Varshalovich **et al**. [135]. N^+ is the total angular momentum of the ion, K^+ is the projection of N^+ onto the body frame z-axis, and m^+ is the projection onto the laboratory frame Z-axis. We also use a set of fifth-order basis splines $u_j(\theta)$ to expand the wave function in θ. Since $u_j(\theta)$ is unaffected by permutations, it is not shown in Table 4.

Table C.1: Permutation symmetry for basis functions in the different degrees of freedom.

Permutation Operation	$e^{im_2\varphi}$	$\mathcal{R}^{N^+}_{K^+m^+}$	$\Phi^I_{g_I}$
P_{12}	$e^{i4\pi/3}e^{-im_2\varphi}$	$(-)^{N^++K^+}\,\mathcal{R}^{N^+}_{-K^+m^+}$	$e^{i4\pi g_I/3}\Phi^I_{-g_I}$
P_{23}	$e^{i2\pi/3}e^{-im_2\varphi}$	$(-)^{N^+}\,\mathcal{R}^{N^+}_{-K^+m^+}$	$e^{i2\pi g_I/3}\Phi^I_{-g_I}$
P_{31}	$e^{i2\pi}e^{-im_2\varphi}$	$(-)^{N^++K^+}\,\mathcal{R}^{N^+}_{-K^+m^+}$	$e^{i2\pi g_I}\Phi^I_{-g_I}$
$P_{12}P_{31}$	$e^{i2\pi/3}e^{im_2\varphi}$	$(-)^{K^+}\,\mathcal{R}^{N^+}_{K^+m^+}$	$e^{i2\pi g_I/3}\Phi^I_{g_I}$
$P_{12}P_{23}$	$e^{i4\pi/3}e^{im_2\varphi}$	$\mathcal{R}^{N^+}_{K^+m^+}$	$e^{i4\pi g_I/3}\Phi^I_{-g_I}$

Application of the antisymmetrization operator $\mathcal{A}$ in Eq.(3.7) to Eq.(C.1) leads to:

$$\begin{aligned}\mathcal{A}\Phi_{\rm try} = \quad & u_j(\theta)\left[1+(-)^{K^+}e^{i\frac{2\pi}{3}(m_2+g_I)}+e^{i\frac{4\pi}{3}(m_2+g_I)}\right]\\ & \times\left[e^{im\varphi}\mathcal{R}^{N^+}_{K^+m^+}\Phi^I_{g_I}-e^{i\frac{2\pi}{3}(m_2+g_I)}(-)^{N^+}\,e^{-im\varphi}\mathcal{R}^{N^+}_{-K^+m^+}\Phi^I_{-g_I}\right]\end{aligned} \tag{C.4}$$

Following the fact that m_2 is integral (half integral) if K^+ is even (odd), and that g_I equals 0 or ±1, we see that the factors in the second line of the right hand side of Eq.(C.4) vanish unless,

$$m_2+g_I=3n \text{ if } \mathrm{K}^+ \text{ iseven}, \tag{C.5}$$

$$m_2+g_I=3n+3/2 \text{ if } \mathrm{K}^+ \text{ isodd}, \tag{C.6}$$

where n is any integer. Under the conditions Eqs.(C.5–C.6), the factors in the first line of the right hand side of Eq.(C.4) vanish if $m_2=0$, $g_I=0$, $K^+=0$ when N^+ is even. Therefore, the basis functions that obey the permutation symmetry are:

$$\Phi^{N^+m^+g_I}_{jm_2K^+}=u_j(\theta)\,e^{im_2\varphi}\mathcal{R}^{N^+}_{K^+m^+}\Phi^I_{g_I}, \tag{C.7}$$

if $m_2=0$, $K^+=0$, $g_I=0$, and N^+ is odd, otherwise,

$$\Phi^{N^+m^+g_I}_{jm_2K^+}=\frac{1}{\sqrt{2}}u_j(\theta)\left[e^{im_2\varphi}\mathcal{R}^{N^+}_{K^+m^+}\Phi^I_{g_I}-(-)^{N^++K^+}\,e^{-im_2\varphi}\mathcal{R}^{N^+}_{-K^+m^+}\Phi^I_{-g_I}\right], \tag{C.8}$$

where m_2, g_I and K^+ obey the relations Eqs. (C.5–C.6).

The explicit form of $\tilde{\Phi}^{Nmg_I}_{jm_2N^+K^+\Lambda}$ in Eq. (3.15) is closely related to $\Phi^{N^+m^+g_I}_{jm_2K^+}$. Insertion of Eq.(3.13) into Eq.(3.10) yields

$$\tilde{\Phi}^{Nmg_I}_{jm_2N^+K^+\Lambda}=u_j(\theta)\,(-)^{l-\Lambda}\,e^{im_2\varphi}\Phi^I_{g_I}C^{N^+K^+}_{l,-\Lambda;N,K}\mathcal{R}^N_{Km}, \tag{C.9}$$

with $K = K^+ + \Lambda$, if $m_2 = 0$, $g_I = 0$, $K^+ = 0$ and N^+ is odd. Otherwise,

$$\tilde{\Phi}^{Nmg_I}_{jm_2N^+K^+\Lambda} = \frac{u_j(\theta)}{\sqrt{2}}(-)^{l-\Lambda}\left[e^{im_2\varphi}\Phi^I_{g_I}C^{N^+K^+}_{l,-\Lambda;N,K}\mathcal{R}^N_{Km} - (-)^{N^++K^+}\ e^{-im_2\varphi}\Phi^I_{-g_I}C^{N^+-K^+}_{l,-\Lambda;N,\tilde{K}}\mathcal{R}^N_{\tilde{K}m}\right], \tag{C.10}$$

where $\tilde{K} = -K^+ + \Lambda$.

Appendix D

Body-frame quantum defect matrix elements

The form of reaction matrix K describing the Jahn-Teller coupling of the p-wave electron can be written as

$$K_{\Lambda\Lambda'} = \begin{pmatrix} K_{00} & K_{01} & K_{0-1} \\ K_{10} & K_{11} & K_{1-1} \\ K_{-10} & K_{-11} & K_{-1-1} \end{pmatrix}. \tag{D.1}$$

In perturbation theory, the matrix elements of the reaction matrix near the equilibrium position obey,

$$\begin{aligned} K_{\Lambda\Lambda'} \approx \quad & -\pi \int dr' \bar{f}_{\varepsilon l\Lambda}\left(r'\right) \bar{f}_{\varepsilon l\Lambda'}\left(r'\right) \\ & \times \int d\omega_e' Y_{l\Lambda}^{*}\left(\theta_e', \varphi_e'\right) \Delta V_e\left(\mathcal{Q}; \mathbf{r_e}'\right) Y_{l\Lambda'}\left(\theta_e', \varphi_e'\right), \end{aligned} \tag{D.2}$$

where $\Delta V_e = V_e\left(\mathcal{Q}; \mathbf{r_e}'\right) - V_e\left(\mathcal{Q}=0; \mathbf{r_e}'\right)$, and $V_e\left(Q, r_e'\right)$ is the interaction between the ion and the Rydberg electron excluding the Coulomb potential, $\mathcal{Q}$ are the vibrational symmetry coordinates, and $\mathbf{r_e}' = \{r', \theta_e', \varphi_e'\}$ are the spherical coordinates of the electron in the body-frame. $\bar{f}_{\varepsilon l\Lambda}\left(r'\right)$ is the regular phase-renormalized Coulomb wave function defined by, $\bar{f}_{\varepsilon l\Lambda} = f_{\varepsilon l}\cos\left(\pi\mu_{\Lambda\Lambda}\left(\mathcal{Q}=0\right)\right) - g_{\varepsilon l}\sin\left(\pi\mu_{\Lambda\Lambda}\left(\mathcal{Q}=0\right)\right)$, where $\{f_{\varepsilon l}, g_{\varepsilon l}\}$ are the usual Coulomb wave functions with energy ε and angular momentum l. $\mu_{\Lambda\Lambda}\left(\mathcal{Q}=0\right)$ are the constant zero-order term of the diagonal quantum defect matrix elements.

To explore the symmetry properties of $K_{\Lambda\Lambda'}$, we write the Taylor expansion in terms of

$\mathcal{Q} = \{Q_1, Q_+, Q_-\}$, where $Q_+ = \rho e^{+i\phi}$ and $Q_- = \rho e^{-i\phi}$,

$$K_{\Lambda\Lambda'} = \sum_{\nu} K^{\nu}_{\Lambda\Lambda'} Q_\nu + \frac{1}{2} \sum_{\nu\mu} K^{\nu\mu}_{\Lambda\Lambda'} Q_\nu Q_\mu + \ldots \tag{D.3}$$

where each summation is over the subscripts 1, + and −. However, the expansion Eq. (D.3) is not valid in our body frame coordinates because $\Delta V_e\left(\mathcal{Q}; \mathbf{r_e}'\right)$ is not single-valued at $Q_+ = Q_- = 0$. This fact is demonstrated in the following discussion of our body frame coordinates.

The body frame coordinates used here are the same as the coordinates defined in Eq. (7) of Ref. [47], but we denote them as $x'y'z'$ instead of xyz to make our notations consistent. The z'-axis is perpendicular to the plane defined by the three nuclei and the x'-axis is associated with the smallest moment of inertia. After manipulating Eqs.(2), (3), and Eq.(7) of Ref. [47] with some algebra, we can write down the cartesian coordinates of the positions of the ith nuclei (x'_i, y'_i, z'_i) as

$$x'_i = \frac{2}{3d} R \cos\left(\frac{\theta}{2} - \frac{\pi}{4}\right) \cos\left(\frac{\varphi}{2} + \vartheta_i\right), \tag{D.4}$$

$$y'_i = -\frac{2}{3d} R \sin\left(\frac{\theta}{2} - \frac{\pi}{4}\right) \sin\left(\frac{\varphi}{2} + \vartheta_i\right), \tag{D.5}$$

$$z'_i = 0. \tag{D.6}$$

where $\vartheta_1 = 5\pi/6$, $\vartheta_2 = -\pi/2$ and $\vartheta_3 = \pi/6$. When θ is very small, following Eqs. (2.5) and Eqs. (3.19) the two sets of coordinates $\{Q_1, \rho, \phi\}$ and $\{R, \theta, \varphi\}$ have the following relationship,

$$Q_1 = 3^{1/4} f \left(R - R_0\right), \tag{D.7}$$

$$\rho = 3^{1/4} f R\theta/2, \tag{D.8}$$

$$\phi = \varphi - 2\pi/3. \tag{D.9}$$

where $R_0 = 3^{1/4} r_{\text{equi}}$. Therefore, when $Q_+ = Q_- = 0$, and hence $\rho = 0$, the positions of the ith nuclei (x'_i, y'_i, z'_i) can be written as,

$$x'_i\left(Q_1, Q_+ = 0, Q_- = 0\right) = \frac{\sqrt{2}}{3d} \left(R_0 + \frac{Q_1}{3^{1/4} f}\right) \cos\left(\frac{\phi}{2} + \vartheta_i + \frac{\pi}{3}\right), \tag{D.10}$$

$$y_i'\left(Q_1, Q_+ = 0, Q_- = 0\right) = \frac{\sqrt{2}}{3d}\left(R_0 + \frac{Q_1}{3^{1/4}f}\right)\sin\left(\frac{\phi}{2} + \vartheta_i + \frac{\pi}{3}\right), \tag{D.11}$$

$$z_i\left(Q_1, Q_+ = 0, Q_- = 0\right) = 0. \tag{D.12}$$

These equations show that the positions of the three nuclei can not be expressed by Q_1, Q_+ and Q_- when $\rho = 0$, and hence the expansion Eq. (D.3) is not valid as $\Delta V_e\left(\mathcal{Q}; \mathbf{r_e}'\right)$ is not single-valued at $Q_+ = Q_- = 0$ and therefore is not infinitely differentiable. However, if we define another set of $\widetilde{x}', \widetilde{y}', \widetilde{z}'$ axis by a passive rotation through $\phi/2$ about z'-axes, the positions of nuclei have defined values when $Q_+ = Q_- = 0$ in this new frame:

$$\widetilde{x}_i'\left(Q_1, Q_+ = 0, Q_- = 0\right) = \frac{\sqrt{2}}{3d}\left(R_0 + \frac{Q_1}{3^{1/4}f}\right)\cos\left(\vartheta_i + \frac{2\pi}{3}\right), \tag{D.13}$$

$$\widetilde{y}_i'\left(Q_1, Q_+ = 0, Q_- = 0\right) = \frac{\sqrt{2}}{3d}\left(R_0 + \frac{Q_1}{3^{1/4}f}\right)\sin\left(\vartheta_i + \frac{2\pi}{3}\right), \tag{D.14}$$

$$\widetilde{z}_i'\left(Q_1, Q_+ = 0, Q_- = 0\right) = 0. \tag{D.15}$$

Hence, the following expansion is valid,

$$\widetilde{K}_{\Lambda\Lambda'} = \sum_{\nu} \widetilde{K}^{\nu}_{\Lambda\Lambda'} Q_\nu + \frac{1}{2}\sum_{\nu\mu} \widetilde{K}^{\nu\mu}_{\Lambda\Lambda'} Q_\nu Q_\mu + \ldots, \tag{D.16}$$

and therefore using the analysis of Longuet-Higgins [136] in which $K_{\Lambda\Lambda}$ is expanded to third order in Q_1 and second order in ρ, gives:

$$\widetilde{K}_{\Lambda\Lambda} = \widetilde{K}^{1}_{\Lambda\Lambda} Q_1 + \widetilde{K}^{11}_{\Lambda\Lambda} Q_1^2 + \widetilde{K}^{111}_{\Lambda\Lambda} Q_1^3 + \widetilde{K}^{+-}_{\Lambda\Lambda}\rho^2. \tag{D.17}$$

We also have

$$\widetilde{K}_{\Lambda\Lambda\pm1} = \widetilde{K}_{\Lambda\pm1\Lambda} = 0, \tag{D.18}$$

and

$$\widetilde{K}_{\Lambda\Lambda\pm2} = \widetilde{K}_{\Lambda\pm2\Lambda} = \widetilde{K}^{1}_{\Lambda\Lambda\pm2}\rho e^{\mp i\phi}, \tag{D.19}$$

to first order in ρ. The matrix elements of $\widetilde{K}_{\Lambda\Lambda'}$ also obey

$$\begin{aligned}\widetilde{K}_{\Lambda\Lambda'} \approx \quad & -\pi \int dr' \bar{f}_{\varepsilon l\Lambda}\left(r'\right) \bar{f}_{\varepsilon l\Lambda'}\left(r'\right) \\ & \times \int d\widetilde{\omega}_e' Y^*_{l\Lambda}\left(\widetilde{\theta}_e', \widetilde{\varphi}_e'\right) V_e\left(\mathcal{Q}, \mathbf{r_e}'\right) Y_{l\Lambda'}\left(\widetilde{\theta}_e', \widetilde{\varphi}_e'\right),\end{aligned} \tag{D.20}$$

where we use the tilde notation to stress that these are expressed in terms of coordinates in the new frame. The rotation to the new frame from our original one has the following effects: $\widetilde{\theta}_e = \theta_e$ and $\widetilde{\varphi}_e = \varphi_e - \phi/2$. Hence a comparison with Eq. (D.2) gives

$$\widetilde{K}_{\Lambda\Lambda'} = K_{\Lambda\Lambda'} e^{i(\Lambda-\Lambda')\phi/2}. \tag{D.21}$$

Because the reaction matrix K and quantum defect matrix μ are related by $\mu = \mu(\mathcal{Q}=0) + \arctan(K)/\pi \approx \mu(\mathcal{Q}=0) + K/\pi + O\left(K^3\right)/\pi + \ldots$, at least to first order, the K matrix and μ matrix have the same symmetry properties, and hence we write the form of μ matrix as Eq.(3.18) and Eqs.(3.23-3.25).

Appendix E

Effective adiabatic potentials

The effective potentials shown in Fig. 1 (a) of the main text are very complicated, making identification of the important physics challenging. For that reason, this section presents some details of our work that not only give support to our physical interpretation of the nature of the three-body parameter but also show how some important nonuniversal aspects appear in the hyperspherical adiabatic representation. In fact, Fig. E.1 shows some of the most drastic nonadiabatic effects found in our calculations. The model proposed in Ref. [16] is also considered, and we show that this model offers an interesting qualitative picture; but since incorporation of corrections to that model diminishes its accuracy in the three-body parameter universality, its agreement with experiment might be fortuitous.

We first consider the validity of the single-channel adiabatic hyperspherical approximation and point out the manner in which some important nonuniversal features manifest themselves. Figure E.1 shows the results for $U_\nu(R)$ and $W_\nu(R)$ obtained from three different two-body potential models. Figures E.1 (a) and (b) show the results for the potential models $v^a_\lambda(\lambda = \lambda^*_2)$ and $v^a_\lambda(\lambda = \lambda^*_{10})$ [Eq. (5.3)], respectively, while Fig. E.1 (c) shows the results obtained for $v_{\rm sch}(D = D^*_6)$ [Eq. (5.2)]. The most striking aspect of these figures is that $U_\nu(R)$ and $W_\nu(R)$ are substantially different, meaning that the nonadiabatic couplings $P_{\nu\nu'}(R)$ and $Q_{\nu\nu'}(R)$ are important near $R = r_{\rm vdW}$. Therefore, it is clear that one needs to go beyond a single channel approximation in order to describe the three-body observables. It is worth noting that the nonadiabatic couplings originate from the hyperradial kinetic energy. Their large values are thus consistent with our physical picture in

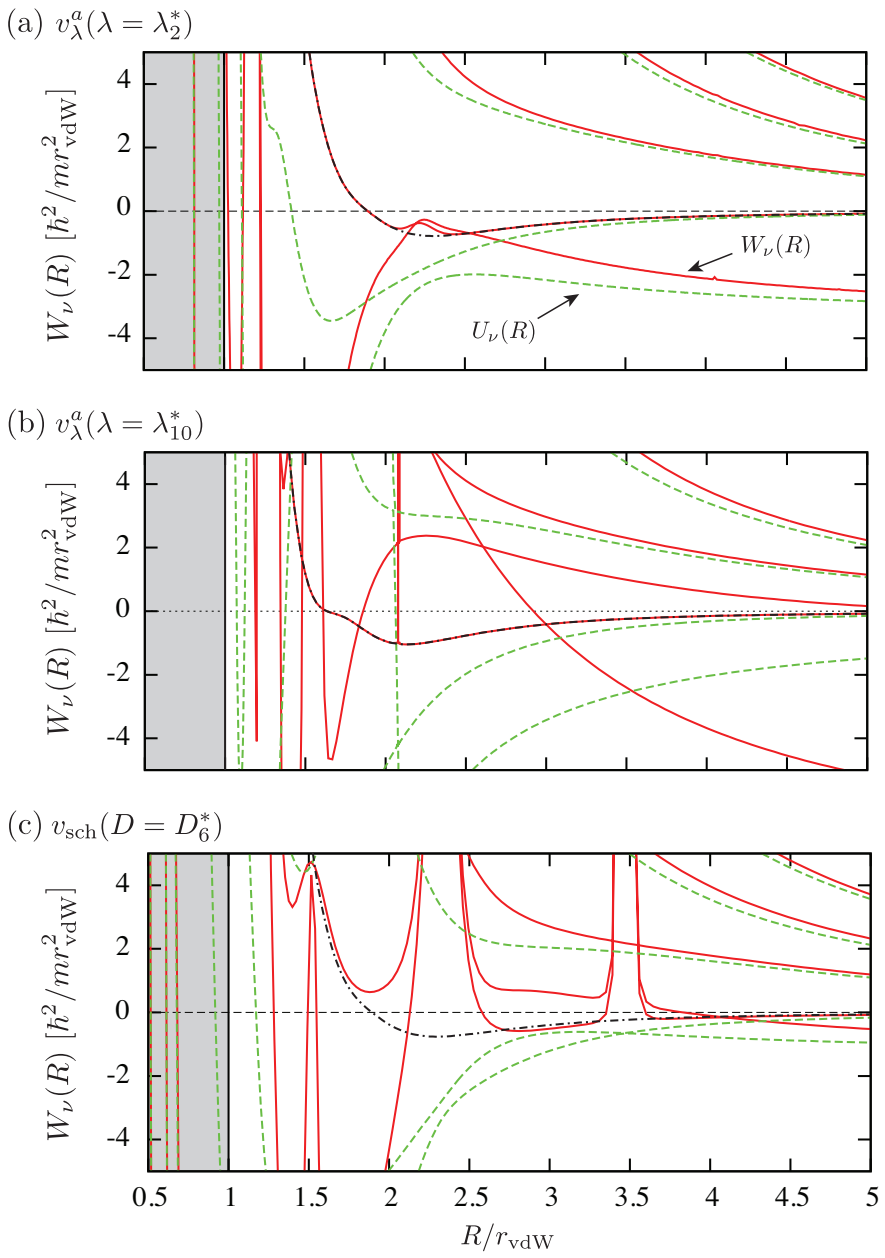

Figure E.1: Comparison of $U_\nu(R)$ (green dashed curves) and $W_\nu(R)$ (red solid curves) demonstrating the importance of nonadiabatic effects introduced by $Q_{\nu\nu}(R)$. (a) and (b) show the results for the potential models $v_\lambda^a(\lambda = \lambda_2^*)$ and $v_\lambda^a(\lambda = \lambda_{10}^*)$ [Eq. (5.3)], respectively, and in (c) we show the results obtained for $v_{\rm sch}(D = D_6^*)$ [Eq. (5.2)]. (a) and (b) also show the effect of the diabatization scheme used in order to prepare some of our figures in the main text (dash-dotted curves). The goal of the diabatization is to eliminate the sharp features resulting from $Q_{\nu\nu}(R)$ which should not contribute substantially to the three-body observables. The case shown in (c), however, does not allow us to easily trace the diabatic version of the potentials W_ν. In this case, however, the "less" sharp features have a larger contribution due to the crossing with a three-body channel describing a collision between a g-wave molecular state and a free atom, giving rise to the anomalous $n = 6$ point for the $v_{\rm sch}$ model in Fig. 4 of the main text. Although such cases are relatively infrequent in our calculations (and occur mostly for the $v_{\rm sch}$ model), they do illustrate nonuniversal effects that can affect the three-body parameter. Nevertheless, the three-body observables obtained for cases like the one shown in (c) are still within the 15% range we claimed for the universality of the three-body parameter.

which the **local** kinetic energy increases and generates the repulsive barrier in our effective potentials. It is also worth mentioning that since the three-body repulsive barrier prevents particles from approaching to small distances, the question of whether or not the short range physics actually changes as a function of the external magnetic field (as in experiments in ultracold quantum gases) [137] can not be directly answered by observing features related to Efimov physics.